Understanding X-ray Pulsars: from Blind Source Separation to Pulse Profile Decompositions

Dissertation

der Mathematisch-Naturwissenschaftlichen Fakultät

der Eberhard Karls Universität Tübingen

zur Erlangung des Grades eines

Doktors der Naturwissenschaften

(Dr. rer. nat.)

vorgelegt von

Inga Saathoff

aus Norden

Tübingen

2023

Abstract

In neutron star X-ray binaries, matter is transferred from the companion to the compact object where it encounters the strong magnetic field at the magnetosphere. The magnetic field redirects the material toward the magnetic poles, where it releases its gravitational potential energy mainly as X-rays. If the spin and magnetic axes are misaligned, this emission can be observed as pulsations, and the object is called an accreting X-ray pulsar. Folding the light curve, i.e. the intensity variation of the emission over time, with the spin period of the pulsar gives a pulse profile, which can have complex shapes due to the interplay of several factors such as geometry, magnetic field configuration, intrinsic beam patterns, and gravitational light bending.

Understanding the physics of X-ray pulsars, and the extreme conditions that are associated with them, presents a number of challenges. Radiative transfer and the dynamical structure of the accretion flow must be modeled to gain insight into their complex nature. These problems are interrelated, since the properties and dynamics of the accreting matter directly affect the X-ray emission, and the resulting radiation pressure in turn changes the accretion flow. Such interactions play an important role in shaping the observed X-ray spectra and they are difficult to understand from both a theoretical and observational point of view. In addition, the emission that escapes from the immediate vicinity of the surface of the neutron star is not necessarily what is observed: during different phases of the star's rotation, emission from both poles may be observed simultaneously due to phenomena such as gravitational light bending. To test and refine models describing the formation of spectra and pulse profiles in X-ray pulsars, it is necessary to determine the contributions of each pole to the observed flux as a function of phase, which helps to study the physical processes involved in radiative transfer. The rotation of the pulsar makes it possible to study the angular dependence of the emission, which in turn contributes to a better understanding of the physics of X-ray pulsars.

To accomplish this, a new data-driven approach is used in this thesis that takes advantage of the pulse-to-pulse variability in the observed flux. The method is based on treating the task as a blind source separation problem, where the goal is to estimate unknown signals mixed with unknown mixing coefficients. In this context, blind source separation techniques can be used by exploiting the inherent flux variability that is partially independent for the two poles. The result of this decomposition are the two signals representing the time variability of the accretion rate at each pole and the weights associated with each pole. These weights are the single-pole pulse profiles of interest.

To establish the method, in this thesis I develop the phase correlated variability analysis (PCVA) through a series of simulations. This includes determining the requirements and limitations of the PCVA to ensure its effectiveness in disentangling the contributions of the two poles in X-ray pulsars. I then demonstrate the application of the PCVA to observational data of the bright persistent X-ray pulsar Cen X−3 obtained from RXTE (Rossi X-ray Timing Explorer) observations. I compare the results obtained with the PCVA to those of previous studies that have addressed the same problem. Based on my results, I find that the symmetry assumption made in the past is incompatible with the PCVA results and thus may not be justified.

In order to interpret the results of the PCVA, I create a toy model to describe the obtained pulse profiles. This model is based on a number of assumptions. First, the geometry of the system is defined by considering the inclination and position angle of the pulsar spin. The emission region is assumed to be generated by a single source at each pole. To introduce asymmetry, a phenomenological beam pattern is defined that is symmetric about a certain direction but asymmetric with respect to the normal of the surface. This results in asymmetric beam patterns due to the rotation of the neutron star. The toy model also allows for an offset of the dipole as an additional parameter and incorporates the effects of gravitational light bending. In this way, the model provides a means to study the effect of different parameters, most importantly the intrinsic beam pattern, on the observed pulse profiles from each pole.

I then address the Cen X−3 PCVA result in the context of the toy model. Despite accounting for gravitational light bending, the presence of mostly non-zero contributions throughout the rotation makes it difficult to find a solution using literature geometry. I find a slight improvement by allowing for an offset of the dipole, but the visibility problem still remains and I discuss possible solutions to this problem. One possibility is to relax the basic pulsar geometry, since all methods for determining the geometry are based on models or assumptions that are not absolute. Alternatively, the use of a more complex beam pattern model or the consideration of extended emission regions could potentially resolve the lack of visibility gaps in the results.

The PCVA developed in this thesis allows the separation of the emission contributions from the two poles of X-ray pulsars. In principle, this method can be applied to any luminous X-ray pulsar, provided that the specified source and observational requirements are met. Thus, by studying the individual contributions from each pole, the PCVA allows the study of changes in the accretion process and structures. In addition, the toy model provides a tool for exploring various parameters that shape the pulse profile, in particular the effects of a slightly asymmetric beam pattern.

Zusammenfassung

In Röntgendoppelsternen mit einem Neutronenstern wird Materie vom Begleiter auf das kompakte Objekt übertragen, wo sie auf das starke Magnetfeld der Magnetosphäre trifft. Das Magnetfeld lenkt die Materie zu den magnetischen Polen, wo sie ihre Gravitationsenergie abgibt, hauptsächlich in Form von Röntgenstrahlung. Wenn die Spin- und Magnetachse versetzt sind, kann diese Emission als Pulsation beobachtet werden, und das Objekt wird dann als akkretierender Röntgenpulsar bezeichnet. Faltet man die Lichtkurve, d. h. die Intensitätsvariation der Emission über die Zeit, mit der Spinperiode des Pulsars, erhält man ein Pulsprofil, das aufgrund des Zusammenspiels verschiedener Faktoren wie Geometrie, Magnetfeldkonfiguration, intrinsische Strahlenmuster und gravitationsbedingte Lichtablenkung komplexe Formen aufweisen kann.

Die Physik von Röntgenpulsaren unter ihren extremen Bedingungen zu verstehen, stellt eine Reihe von Herausforderungen dar. Der Strahlungstransport und die dynamische Struktur des Akkretionsflusses müssen modelliert werden, um ihre komplexe Natur zu verstehen. Diese Probleme sind miteinander verknüpft, da die Eigenschaften und die Dynamik der akkretierenden Materie die Röntgenemission direkt beeinflussen. Diese Wechselwirkungen spielen eine wichtige Rolle bei der Entstehung der beobachteten Röntgenspektren. Sie zu verstehen ist sowohl aus theoretischer als auch aus beobachtungstechnischer Sicht keine triviale Aufgabe. Hinzu kommt, dass die Emission aus der unmittelbaren Umgebung der Neutronensternoberfläche aufgrund von Phänomenen wie der gravitationsbedingten Lichtablenkung nicht unbedingt mit der beobachteten Strahlung übereinstimmt. Außerdem kann während verschiedener Phasen der Sternrotation die Emission von beiden Polen gleichzeitig beobachtet werden. Um Modelle zu testen und zu verfeinern, die die Entstehung von Spektren und Pulsprofilen in Röntgenpulsaren beschreiben, müssen die Beiträge beider Pole zum beobachteten Fluss als Funktion der Phase bestimmt werden. Dies ermöglicht die Untersuchung der physikalischen Prozesse, die am Strahlungstransport beteiligt sind. Die Rotation des Pulsars erlaubt es, die Winkelabhängigkeit der Emission zu untersuchen, was wiederum zu einem besseren Verständnis der Physik von Röntgenpulsaren beiträgt.

In dieser Arbeit wird ein neuer datenbasierter Ansatz verwendet, der die Puls-zu-Puls-Variabilität des beobachteten Flusses ausnutzt. Die Methode basiert auf der Behandlung der Aufgabe als ein Problem der blinden Quellentrennung. Das Ziel ist die Schätzung unbekannter Signale, die mit unbekannten Mischkoeffizienten gemischt sind. Dabei kann die inhärente Variabilität des Flusses genutzt werden, die teilweise unabhängig von den beiden Polen ist. Das Ergebnis sind zwei Signale, die die Flussvariabilität jedes Pols

darstellen, skaliert durch die beiden Gewichtungen, die jedem Pol zugeordnet sind. Diese Gewichtungen sind die einpoligen Pulsprofile, die von Interesse sind.

Um die Methode zu etablieren, entwickle ich in dieser Arbeit die phasenkorrelierte Variabilitätsanalyse (PCVA) durch eine Reihe von Simulationen. Dies beinhaltet die Bestimmung der Anforderungen und Grenzen der PCVA, um ihre Effektivität bei der Trennung der Beiträge beider Pole in Röntgenpulsaren zu bestimmen. Anschließend demonstriere ich die Anwendung der PCVA auf Beobachtungsdaten des hellen Röntgenpulsars Cen X−3, die aus RXTE (Rossi X-ray Timing Explorer) Beobachtungen stammen. Ich vergleiche die Ergebnisse der PCVA mit früheren Arbeiten, die sich mit dem gleichen Problem beschäftigten. Auf der Grundlage meiner Ergebnisse stelle ich fest, dass die in der Vergangenheit getroffene Annahme der Symmetrie der intrinsischen Strahlungsmuster mit den Ergebnissen der PCVA unvereinbar und daher möglicherweise nicht gerechtfertigt ist.

Um die Ergebnisse der PCVA interpretieren zu können, habe ich ein einfaches Modell zur Beschreibung der erhaltenen Pulsprofile erstellt. Dieses Modell basiert auf einer Reihe von Annahmen. Zunächst wird die Geometrie des Systems unter Berücksichtigung der Inklination und des Positionswinkels des Pulsarspins definiert. Es wird angenommen, dass die Emissionsregion von einer einzelnen Quelle an jedem Pol erzeugt wird. Um eine Asymmetrie einzuführen, wird ein phänomenologisches Strahlungsmuster definiert, das symmetrisch zu einer bestimmten Richtung, aber asymmetrisch zur Oberflächennormalen ist. Dies führt zu asymmetrischen Strahlenmustern aufgrund der Rotation des Neutronensterns. Das Modell ermöglicht es auch eine Dipolverschiebung als zusätzlichen Parameter zu berücksichtigen und die Effekte der gravitationsbedingten Lichtablenkung miteinzubeziehen. Auf diese Weise bietet das Modell die Möglichkeit den Einfluss verschiedener Parameter, insbesondere des intrinsischen Strahlungsmusters, auf die beobachteten Pulsprofile zu untersuchen.

Ich verwende das Modell, um das Cen X−3 PCVA-Ergebnis zu untersuchen. Da die meisten Beiträge während der Rotation nicht Null sind, ist es naheliegend, dass die Emissionsregionen fast immer sichtbar sind. Trotz der Berücksichtigung der gravitationsbedingten Lichtablenkung ist eine Lösung, die dies widerspiegelt, auf der Basis der Literaturgeometrie schwierig. Eine leichte Verbesserung wird durch die Einbeziehung einer Dipolverschiebung erreicht, aber das Problem der fehlenden Sichtbarkeit der Emissionsregion bleibt bestehen. Ich diskutiere mögliche Lösungen für dieses Problem. Eine Möglichkeit besteht darin, die Beschränkung der Pulsargeometrie zu lockern, da alle Methoden zur Bestimmung der Geometrie auf Modellen oder Annahmen beruhen, die nicht absolut sind. Eine andere Möglichkeit wäre, ein komplexeres Strahlungsmodell zu verwenden oder ausgedehntere Emissionsregionen zu berücksichtigen.

Die in dieser Arbeit entwickelte PCVA erlaubt die Trennung der Emissionsbeiträge der beiden Pole von Röntgenpulsaren. Diese Methode kann prinzipiell auf jeden leuchtkräfti-

gen Röntgenpulsar angewendet werden, sofern die spezifizierten Quellen- und Beobach-
tungsbedingungen erfüllt sind. Durch die Untersuchung der individuellen Beiträge der
beiden Pole ermöglicht die PCVA die Untersuchung von Veränderungen im Akkretions-
prozess und in den Akkretionsstrukturen. Darüber hinaus bietet das von mir entwickelte
Modell ein Werkzeug zur Untersuchung verschiedener Parameter die das Pulsprofil formen,
insbesondere die Auswirkungen eines leicht asymmetrischen Strahlungsmusters.

Contents

I   Astrophysical Context

II   Method Development

III	**Application to Cen X−3**	

List of Figures

List of Tables

List of Abbreviations

AMP   Accreting Millisecond Pulsar
APP   Accretion Powered Pulsar
AXP   Anomalous X-ray Pulsar

BeXRB   Be X-ray Binary
BW   Black Widow Pulsar

CCO   Central Compact Object
CMB   Cosmic Microwave Background
CRSF   Cyclotron Resonance Scattering Feature
CT   Computed Tomography

ECG   Electrocardiogram
EEG   Electroencephalogram
EoS   Equation of State
eXTP   Enhanced X-ray Timing and Polarimetry

fMRI   Functional Magnetic Resonance Imaging

HMXB   High Mass X-ray Binary
HXMT   Hard X-ray Modulation Telescope

ICA   Independent Component Analysis
IENS   Internal Energy Powered Neutron Star
IMXB   Intermediate Mass X-ray Binary
INS   Isolated Neutron Star
ISS   International Space Station
IXPE   Imaging X-ray Polarimetry Explorer

LMXB   Low Mass X-ray Binary

MAXI   Monitor of All-sky X-ray Image
MSRP   Millisecond Radio Pulsar

NASA   National Aeronautics and Space Administration

NICER	Neutron Star Interior Composition Explorer
NMF	Non-Negative Matrix Factorization
PCA	Principal Component Analysis
PCA	Proportional Counter Array
PCVA	Phase Correlated Variability Analysis
PET	Positron Emission Tomography
PHA	Pulse Height Amplitude
PI	PHA Invariant
PSR	Radio Pulsar
QED	Quantum Electrodynamics
RB	Redback Pulsar
RFID	Radio Frequency Identification
RMF	Response Matrix File
RPP	Rotation Powered Pulsar
RRAT	Rotating Radio Transient
RXTE	Rossi X-ray Timing Explorer
SFXT	Supergiant Fast X-ray Transient
SGR	Soft Gamma-ray Repeater
SgXRB	Supergiant X-ray Binary
Swift	Neil Gehrels Swift Observatory
TOV	Tolman-Oppenheimer-Volkoff
WMAP	Wilkinson Microwave Anisotropy Probe
XRB	X-ray Binary
XRP	X-ray Pulsar

1. Introduction

Accreting X-ray pulsars are a unique class of binary stars. They consist of a neutron star, which is the smaller and more compact of the two stars, and a companion or "donor" star. In this binary system, the neutron star accretes matter from its companion. However, before the material can reach the surface, it is stopped by the neutron star's magnetosphere, which is a region of space surrounding the star that is defined by the strength of its magnetic field. In the presence of a sufficiently strong magnetic field, matter is deflected and guided along the field lines to the surface of the neutron star near the magnetic poles. When it reaches the surface, a significant amount of energy is released in the form of photons with energies between about 100 electron volts and 100 kilo-electron volts, the energy range of X-rays. This makes accreting X-ray pulsars some of the brightest X-ray sources in the sky (Caballero & Wilms 2012; Fürst et al. 2019; Mushtukov & Tsygankov 2022).

The intense X-ray emission from accreting X-ray pulsars is observed as pulsations, giving them their name. These pulsations are caused by the rotation of the neutron star and the misalignment between the spin axis and the magnetic axis of the neutron star. The pulsations are remarkably distinctive, and their shapes can take on different forms. The average shape of the pulsations is known as the pulse profile, which can vary with energy, luminosity, orbital phase, and other parameters (Basko & Sunyaev 1976; Karino 2007; Doroshenko et al. 2020; Tuo et al. 2020; Alonso-Hernández et al. 2022; Wang et al. 2022; Kong et al. 2022; Mushtukov & Tsygankov 2022).

The analysis of pulse profiles in X-ray pulsars can help to understand the physics of neutron stars (Bachetti et al. 2014; Doroshenko et al. 2022a). By accurately measuring the period, models describing the structure and formation of neutron stars can be refined (Kutschera 1998; Cerda-Duran & Elias-Rosa 2018). The shape of the pulse profile is affected by the interaction between the accretion disk and the magnetic field of the neutron star, so studying the pulse profile can help us understand the dynamics of matter accretion, the transfer of angular momentum, and the structure of the accretion disk (Naso et al.

2013; Brumback et al. 2021). In addition, pulse profiles are a tool for studying the internal properties of neutron stars (Mushtukov et al. 2015a). By studying the characteristics of the pulse profiles, such as their shape and intensity, we can gain insight into the equation of state of the neutron star, its composition, and the possible presence of exotic matter in its core (Watts et al. 2016; Watts 2019; Watts et al. 2019). The study of pulse profiles also provides valuable information about binary evolution, shedding light on processes such as mass transfer and orbital dynamics (Serylak et al. 2022). X-ray pulsars, with their high gravitational fields, also offer opportunities beyond neutron star physics, allowing us to test theories such as general relativity (Kim & Trippe 2021). In addition, the study of accretion flows provides insights into plasma physics, instabilities within the accretion process, the production of X-ray emissions, and radiative transfer (Bulik et al. 2003; Becker & Wolff 2007; Annala & Poutanen 2010; Mushtukov & Tsygankov 2022).

In summary, understanding the pulse profiles of X-ray pulsars contributes to advancing our knowledge in a wide range of fields, such as fundamental properties of neutron stars, accretion processes, and plasma physics. The importance of studying and understanding these pulse profiles is therefore clear. However, despite decades of dedicated research since the discovery of X-ray pulsars in 1971 (Giacconi et al. 1971a), the formation of their pulse profiles remains poorly understood. One of the main problems is that all the observed properties of these sources depend on the geometrical configuration of the emission regions, so that the intrinsic beam patterns of the radiation are highly uncertain (Basko & Sunyaev 1976; Wang & Welter 1981; Riffert & Meszaros 1988; Leahy 1991; Riffert et al. 1993; Kraus et al. 1995; Bulik et al. 1995; Leahy 2004; Caballero et al. 2011; Sasaki et al. 2012; Iwakiri et al. 2019). This in turn makes the verification of theoretical calculations very challenging. The main goal of this thesis is to fill this gap in our knowledge by approaching the study of pulse profiles from a fresh perspective.

I divide this thesis into three parts. In the first part I provide the context for this thesis. I begin with an introduction to neutron stars in Chapter 2. This chapter reviews the basic properties of neutron stars, such as their size and mass, which are not well constrained, as well as the formation and classification of neutron stars. Many neutron stars are observed in binary systems where they interact with companion stars, and studying these systems can provide a broader understanding of neutron stars in general, which is also discussed in this chapter.

In the past, astronomy relied primarily on naked-eye observations, which included observing the positions of objects in the night sky, their brightness, their apparent motion, and variations in their properties over time. These basic observables continue to be studied, such as object position, time, intensity, and now additional properties such as energy and polarization have been added. In Chapter 3 I will review these observables, with a particular focus on the insights they can provide for accreting X-ray pulsars. In time series analysis, the pulse profiles of these pulsars show up as distinct patterns in the light curve

data, and since these are the focus of this thesis, they will be discussed in detail.

The X-ray energy range in which X-ray pulsars emit radiation is beyond the range of the human eye and requires specialized tools to observe. Observations in the X-ray range can only be made with space-based telescopes. I discuss some of the instrument details in Chapter 4 of this thesis, with a focus on the RXTE (Rossi X-ray Timing Explorer) satellite as I use its data in this thesis.

The second part of this thesis is dedicated to the development of a new method based on blind source separation. In Chapter 5 I introduce the concept of blind source separation and give examples of its application in various fields. I also examine well-established algorithms for solving this problem, which form the basis of this method.

In Chapter 6 I investigate the application of blind source separation to X-ray pulsars. The methodology developed and tested for this purpose is called "phase correlated variability analysis" (PCVA). In order to establish the efficacy of PCVA, I perform a series of simulation and verification studies.

In the third part of the thesis, Chapter 7, I focus on the application of the newly developed PCVA method to a specific X-ray pulsar, namely Cen X$-$3. The results obtained by PCVA are presented and show discrepancies with the existing literature. To gain a better understanding of these results, I create a toy model of a pulsar. This model produces pulse profiles based on given geometries and phenomenological beam patterns, thereby helping to physically understand the PCVA results.

I conclude the thesis with a summary and brief outlook on the future prospects of PCVA and blind source separation in X-ray astrophysics in Chapter 8.

Astrophysical Context

2. Neutron Stars: Endpoints of Stellar Evolution

Neutron stars are among the most extreme objects in the universe. They are the remnants of massive stars and form through the process of supernova explosions - the end of a massive star's life. The core of the progenitor star collapses under its own gravity, creating an object with a density equal to or greater than that of atomic nuclei. As a result, neutron stars have extreme physical properties, unlike anything we observe on Earth.

In this chapter, I review some basic properties of neutron stars and their formation, starting with an overview of the life cycles of high-mass stars and the formation of neutron stars in Section 2.1. In Section 2.2, I discuss some of the properties of neutron stars, such as structure and composition, which are closely related to the mass and radius described in the equation of state (EoS). Finally, I discuss the role of binary evolution with an overview of X-ray binaries (XRB) in Section 2.3.

2.1 Evolution of High-Mass Stars

The interstellar medium can be considered homogeneous on large scales (Schneider 2015). On smaller scales, however, both densities and temperatures vary significantly, and clouds of gas can collapse under their own gravity to form stars under the following condition:

$$M > \frac{3kT}{2G\bar{m}} R \equiv M_{\mathrm{J}} \, , \tag{2.1}$$

where

k ...... Boltzmann constant,
G ...... gravitational constant,
M ...... mass of the cloud,
T ...... temperature of the cloud,

> R ...... radius of the cloud,
> $\bar{m}$ ...... average mass per particle $\hat{\approx}$ chemical composition, and
> M_{J} ...... Jeans mass.

The Jeans mass therefore describes the critical conditions under which a cloud of gas will collapse under its own gravity, and forms new stars. It depends on the temperature, size, and composition of the gas. When the mass of a gas cloud exceeds the Jeans mass, it becomes unstable and begins to fragment into smaller clumps, eventually forming protostars that ignite and become stars (Ryan & Norton 2010, p. 178). Once a protostar has formed, its only source of energy is the release of gravitational potential energy. This energy can be dissipated by an accretion disk surrounding the young star, or it can be released as heat from the contraction of the gas (Weigert & Wendker 2010). The timescale that dominates this process is known as the Kelvin-Helmholtz timescale, which determines how long the protostar will continue to contract and heat up before reaching hydrostatic equilibrium:

$$t_{\mathrm{KH}} \approx \frac{GM^2}{3RL} \, , \tag{2.2}$$

where

> M ...... mass of the star,
> R ...... radius of the star, and
> L ...... luminosity produced.

For the sun, t_{KH} is about 10^7 years, but since t_{KH} is proportional to M^2, this time can be much shorter for higher-mass stars (Weigert & Wendker 2010; Silva Aguirre 2018). With the ignition of hydrogen fusion, the star enters the main sequence, which is the longest phase in a star's life and can be seen in the Hertzsprung-Russell diagram in the left panel of Figure 2.1. The star is supported by the thermal pressure from the hydrogen fusion at this stage. The time it takes for a star to exhaust its nuclear fuel is called the nuclear timescale, given by

$$t_{\mathrm{nuc}} = \frac{E_{\mathrm{nuc}}}{L} \, , \tag{2.3}$$

where E_{nuc} is the energy released by nuclear fusion. The nuclear timescale depends on the nuclear reaction chains taking place in the star (Weigert & Wendker 2010; Bhattacharya & van den Heuvel 1991). Assuming that a total of about 10% of the hydrogen is converted to helium, the Sun's nuclear timescale is about 10^{10} years. Since the mass-luminosity relation of main sequence stars is approximated as $L \propto M^4$, and the energy produced by hydrogen fusion is proportional to the hydrogen available for fusion, which is proportional
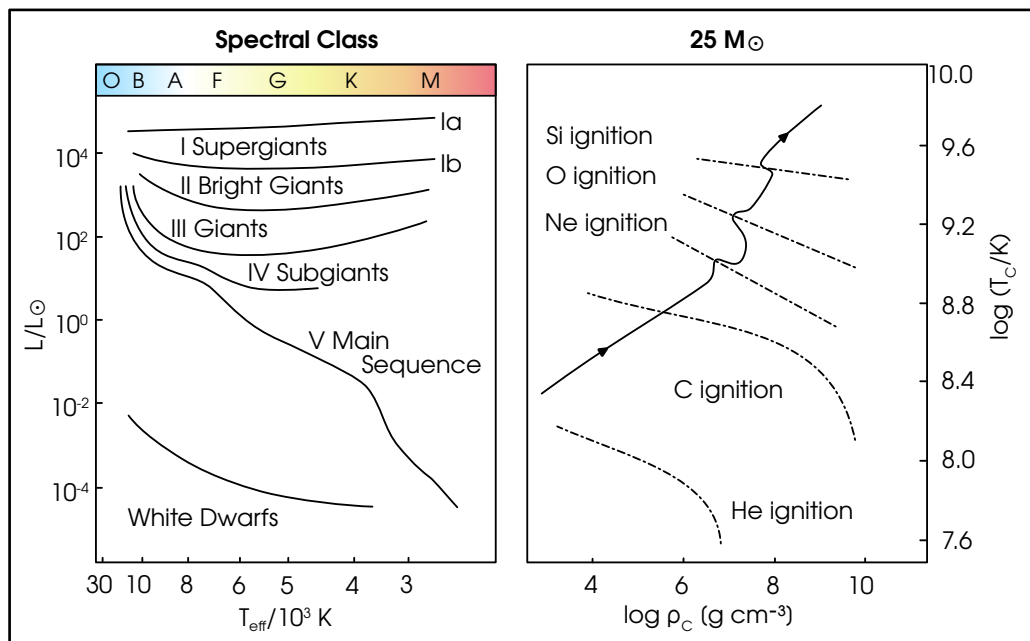
Figure 2.1: *Left:* The schematic Hertzsprung-Russell diagram plots the luminosity of stars against their effective temperature (lower abscissa) or spectral type (upper abscissa). Stars spend most of their lives on the main sequence. *Right:* This schematic central temperature versus central density diagram shows the evolutionary track of a $25\,M_\odot$ star, along with the locations where nuclear fuels ignite, indicated by dash-dotted lines. The figure is adapted from Figure 18 in Bhattacharya & van den Heuvel (1991).

Table 2.1: Burning phases and timescales for a $25\,M_\odot$ star. Based on Table 9 in Bhattacharya & van den Heuvel (1991).

Fuel	Ashes	Time (yr)
^{1}H	^{4}He, ^{14}N	5×10^6
^{4}He	^{12}C, ^{16}O, ^{22}Ne	5×10^5
^{12}C	^{20}Ne, ^{24}Mg, ^{16}O, …	60
^{20}Ne	^{16}O, ^{24}Mg, ^{28}Si	1
^{16}O	^{28}Si, ^{32}S	0.5
^{28}Si	^{56}Ni, $A \sim 56$ nuclei	0.01
^{56}Ni	n, ^{4}He, ^{1}H	10^{-6}
$A \sim 56$ nuclei	(depends on photo disintegration and neutralization)	10^{-6}
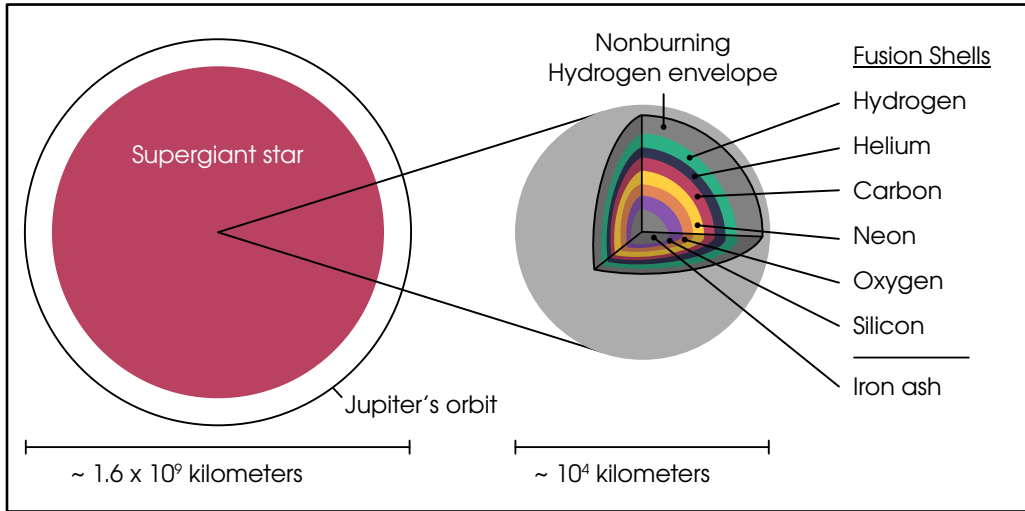
Figure 2.2: This illustration, though not to scale, shows the core of a massive star before a supernova explosion. Like the layers of an onion, the core is composed of nested spherical shells that fuse different elements, starting with hydrogen and helium, then carbon, and finally silicon. The scales shown are only imprecise and extremely approximate, they are meant to give a rough estimate of the potential dimensions a star may have. In fact, the range of possible sizes is extremely large.

to the mass of the star ($E_{nuc}^H \propto M_H \propto M$), the timescale of hydrogen burning is:

$$ t_{nuc}^H = \frac{E_{nuc}^H}{L} \propto \frac{M}{M^4} \approx 10^{10}\, a \left(\frac{M}{M_\odot} \right)^{-3}, \tag{2.4} $$

where

E_{nuc}^H $\ \ldots\ldots$ energy released by nuclear fusion of hydrogen, and
$M_\odot$ $\ \ldots\ldots$ solar mass.

As an example, Table 2.1 shows the various burning phases of a high-mass star with a mass of $25\,M_\odot$ (Bhattacharya & van den Heuvel 1991). In general, stars spend between about 10^6 and 10^{12} years on the main sequence, with higher-mass stars having shorter lifetimes (Weigert & Wendker 2010). For stars with a mass greater than about $12\,M_\odot$, these stages occur in a straightforward manner, as shown for a $25\,M_\odot$ star on the right side of Figure 2.1. When silicon burns in a star, it produces a core of mostly iron surrounded by concentric shells of silicon, oxygen, neon, carbon, helium, and hydrogen, see Figure 2.2 for an illustration. The pressure generated by the fusion reactions sustains the star during its time on the main sequence. However, once the iron core of a star has formed, thermonuclear

fusion no longer produces energy because elements heavier than iron can only release energy by fission. As a result, the pressure drops and the core collapses. The electrons in the core become degenerate, and when the mass of the core exceeds the Chandrasekhar limit of about $1.4\,M_\odot$, the electron degeneracy pressure can no longer support the core, causing it to collapse even further. In addition, two types of reactions occur within the core that absorb energy and further reduce the pressure. First, high-energy gamma rays can disrupt iron nuclei in a process known as nuclear photodisintegration, unbinding the nuclei and absorbing energy. Second, electron capture releases energy in the form of neutrinos (Ryan & Norton 2010, pp. 150 ff.). The reaction

$$p + e^- \rightarrow n + \nu_e \,, \tag{2.5}$$

where

$\quad p \quad \ldots\ldots$ proton,
$\quad e^- \quad \ldots\ldots$ electron,
$\quad n \quad \ldots\ldots$ neutron, and
$\quad \nu_e \quad \ldots\ldots$ electron neutrino,

is known as neutronization and it involves the combination of protons and electrons to create neutrons, resulting in a reduction in the number of electrons, which causes a rapid drop in the pressure they previously provided (Ryan & Norton 2010, pp. 150 ff.). The result of a core collapse supernova is either a neutron star or a black hole. In a first-order approximation, this is determined by the mass of the progenitor. In Figure 2.3 it is shown that stars with a mass of less than about 9 solar masses do not undergo core collapse. Instead, they become white dwarfs once they have exhausted their nuclear fuel and shed their outer layers in the form of a planetary nebula. White dwarfs are supported by the electron degeneracy pressure. On the other hand, for stars with masses between 9 and 25 solar masses, the result of core collapse is a neutron star. Above 25 solar masses, black holes are the most likely outcome. However, additional factors such as the metallicity of the progenitor can influence the evolution and the resulting remnant formation. Figure 2.3 shows that for stars with a mass greater than 25 solar masses, neutron stars could potentially form if the progenitor star has a high metallicity. Other factors that affect the evolution of the star and the resulting remnant formation are binary evolution, described in Section 2.3, and the rotation of the star (Heger et al. 2003; Ryan & Norton 2010).

In this thesis, and therefore in the following section, I will omit white dwarfs and black holes and focus on neutron stars.

2.2 Neutron Stars: Structure and Properties

At the end of the high-mass star's life, the core undergoes gravitational collapse until it reaches a stable state in which the neutron degeneracy pressure balances the gravitational
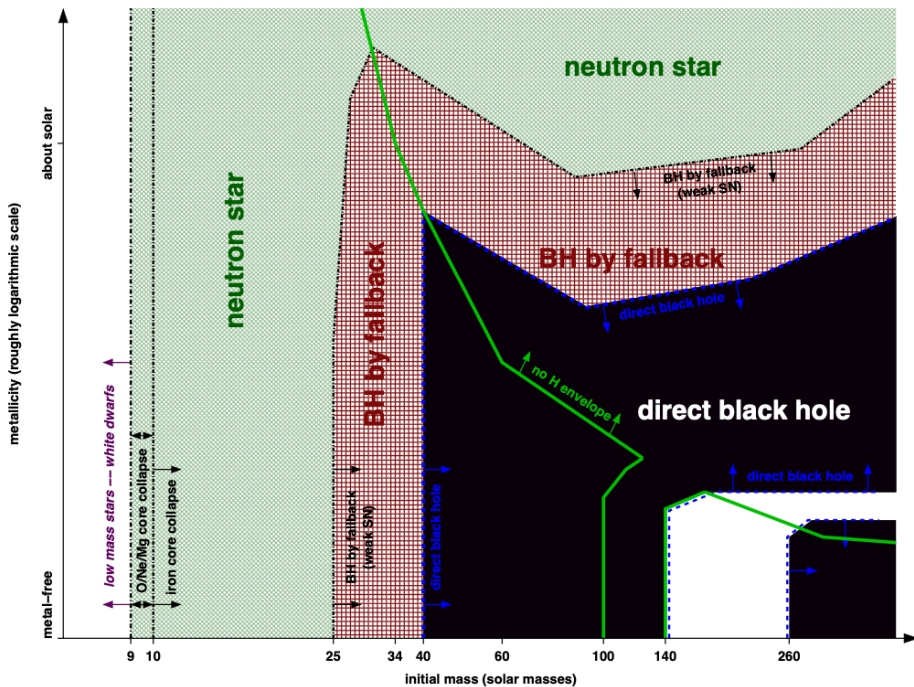
Figure 2.3: The formation of either a black hole or a neutron star in the final stages of a massive star's life is influenced not only by its mass, but also by its metallicity. If the star's mass is less than 9 times that of the Sun, it will become a white dwarf without undergoing core collapse. The boundary between neutron star and black hole formation is represented by a black dashed-dotted line. Neutron stars form for stars with masses between 9 and 25 solar masses. If the initial metallicity is high, neutron stars can also form from stars with masses greater than 25 solar masses. The figure is taken from Heger et al. (2003).

force. This pressure arises from two fundamental quantum mechanical effects: the Pauli exclusion principle and the Heisenberg uncertainty principle. The exclusion principle restricts the compression of matter to a certain limit and it applies to all fermions, including neutrons. These particles are confined to a finite volume in the core and can only occupy discrete energy states, which are a specific type of quantum state that characterizes the allowed energy levels in the system. As more neutrons are added or the volume is reduced, they have to adopt higher energy states. Eventually, the lowest energy states are fully occupied and the system becomes degenerate. On the other hand, Heisenberg's uncertainty principle states that the uncertainty in momentum (Δp) multiplied by the uncertainty in position (Δx) cannot be less than a certain amount ($\hbar/2$, where $\hbar$ is the reduced Planck constant). In the core of the neutron star, the positions of the particles have little uncertainty due to the compressed state. As a result, the uncertainty in the momentum must be large. This leads to the degeneracy pressure, which is much greater than the thermal pressure, and is able to counteract the gravitational collapse of the star and form a stable neutron star (Longair 2011, pp. 394 ff.).

2.2.1 Composition and Internal Structure

Inside the newly formed neutron star, the nuclear composition is determined by two fundamental forces: the nuclear force and the Coulomb repulsive force. At low densities, the nuclear force is stronger than the Coulomb force for atomic nuclei smaller than iron. At higher densities, however, the inverse electron induced β decay process (Equation 2.5) favors the formation of neutron-rich nuclei. For this reaction to occur, the electrons must have sufficient energy as the neutrons in the nucleus are degenerate. As the nuclei become increasingly neutron-rich, they become unstable and eventually break apart, releasing neutrons. This phenomenon is known as "neutron drip" and eventually an equilibrium is reached between the neutron drip and the inverse beta decay. As a result, the remaining matter consists of a combination of electrons, neutron-rich nuclei and free neutrons. In a non-degenerate gas, free neutrons decay into protons and electrons with a half-life of about 10.2 minutes. In a degenerate gas, this decay is prevented because there are no quantum states for the electrons to occupy. With increasing density, more matter is converted into neutrons, and at a density of about 10^{15} g cm^{-3} almost all the matter has been converted into neutrons. By this point, the neutron-to-proton ratio is about 200 : 1. This excess of neutrons gives neutron stars their name (Longair 2011, pp. 402 f., Shapiro & Teukolsky 1986, p. 43, Ryan & Norton 2010, p. 158). The layers of a typical neutron star, from its atmosphere to its core, are shown schematically in Figure 2.4:

Atmosphere: The atmosphere is the outermost layer of a neutron star, only a few millimeters to centimeters thick. Electromagnetic radiation comes from the photosphere, which is inside the atmosphere.
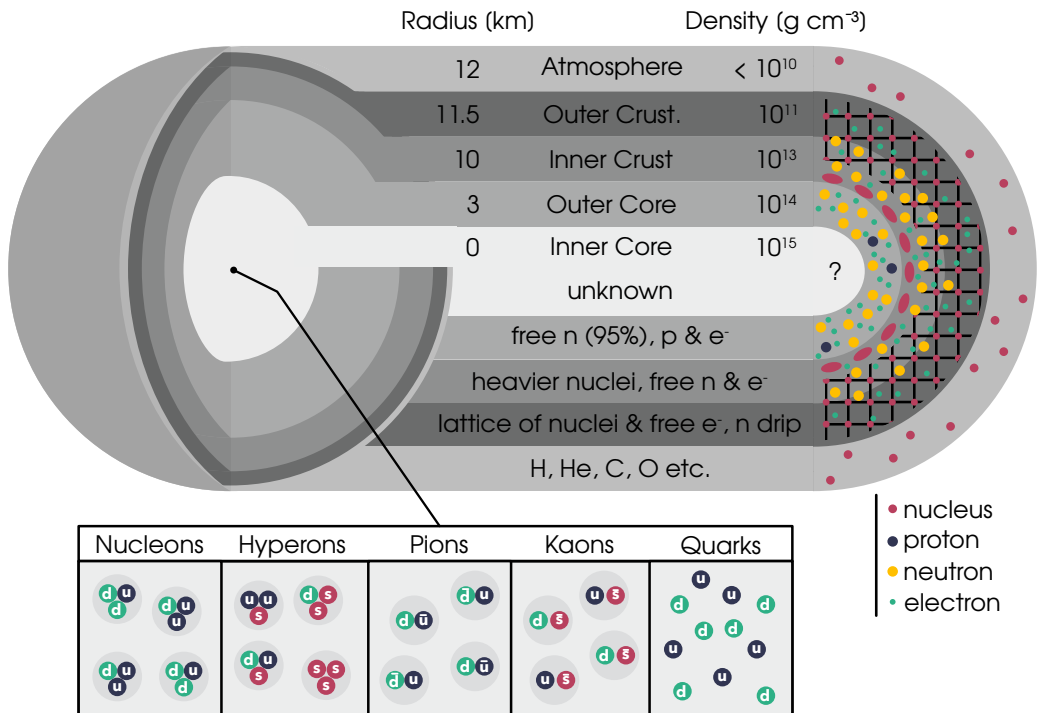
Figure 2.4: Schematic structure and composition of a neutron star (not to scale). Partly based on Weigert & Wendker (2010); Watts et al. (2016, 2019).

Outer Crust: In the outermost layer of the outer crust, which can be several hundred meters thick, there may be a small amount of non-degenerate electrons. The rest of the crust is a solid, consisting of atomic nuclei surrounded by degenerate electrons. In fact, this is roughly the same material that white dwarfs are made of. As the density increases with depth, the nuclei become more neutron-rich.

Inner Crust: Neutrons begin to drip out of the nuclei at the boundary between the outer and inner crusts, as described above. As a result, the inner crust is a mixture of electrons, free neutrons and a variety of neutron-rich nuclei. This layer is about a kilometer thick. At the bottom of the inner crust, depending on the model, the nuclei can become non-spherical and form a "mantle" structure.

Outer Core: The outer core of a neutron star is a few kilometers thick and consists of a mixture of neutrons, protons and electrons. The density and temperature of the core are high enough to create a state of degeneracy in these particles. In this layer, the equilibrium between beta decay and inverse electron capture is maintained, regulating the number of protons and neutrons.

Inner Core: The innermost layer of a neutron star is the densest region. The composition of this core is highly uncertain and varies depending on the model used to describe it. The core can be several kilometers thick and is characterized by extreme temperatures and pressures. There are several models to describe the composition of the inner core, such as the following. For an overview of the various particles and subatomic particles that are mentioned below, see Figure 2.5.

1. Hyperonization refers to the hypothesis that the core of a neutron star is composed mainly of hyperons. These subatomic particles are made up of u and d quarks similar to protons and neutrons, but with the addition of a strange s quark. Because s quarks are more massive than u and d quarks, hyperons have a greater mass than protons and neutrons.

2. Pions are a type of subatomic particle that belong to the class of mesons, which are particles made up of a quark and an antiquark. More specifically, pions are made up of u or d quarks and antiquarks. Pions are known to interact strongly with each other, and it has been hypothesized that under extreme conditions, such as in the core of neutron stars, pions may form a kind of Bose-Einstein condensate. In this state, the pions would all occupy the same quantum state, and the resulting condensate would have different properties to those of the individual pions.

3. Kaons are also known as K mesons and consist of either a u or d quark in combination with an s antiquark. Like pions, kaons are particles that could also undergo Bose-Einstein condensation in the interior of a neutron star.

4. Finally, the most exotic hypothesis is that the matter in the core of a neutron star could undergo a phase transition leading to the formation of a state of matter known as quark matter. This would happen if the density and temperature were high enough
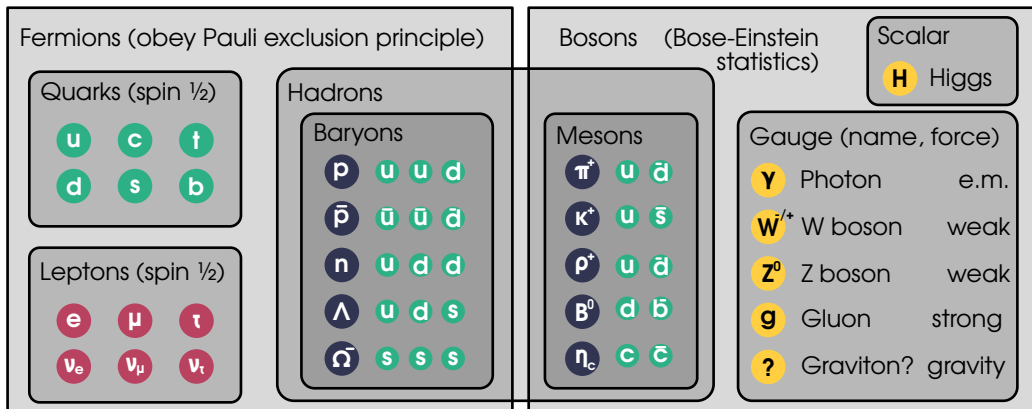
Figure 2.5: The Standard Model of particle physics is described by quarks, leptons, and bosons. Quarks and leptons, as fermions, obey the Pauli exclusion principle. The bosons in the Standard Model consist mainly of gauge bosons, which serve as force carriers. Hadrons, which are also shown here but are not part of the Standard Model, include baryons and mesons, and are formed by the strong force holding two or more quarks together. Specifically, baryons consist of an odd number of quarks, typically three, and the proton and neutron belong to this group and are fermions. On the other hand, mesons are bosons, made up of an even number of quarks, typically one quark and one anti-quark. Examples of mesons are the pion and the kaon. Note that this is not a complete picture and only captures the parts relevant to this thesis.

for the protons and neutrons to split into their constituent quarks, which would then form a new phase of matter. Quark matter is thought to be even denser than nuclear matter and could have very unusual properties.

Models 2-4 are also called "exotic models" of dense matter. These models directly affect the conditions and interactions between particles at super-nuclear density, which are not yet fully known and require further research to understand (Haensel et al. 2007, pp. 11 ff., Camenzind 2007, pp. 188 f., Longair 2011, p. 404). The properties of a neutron star, such as its mass and radius, are affected by the conditions in its core. These properties, and the equation that relates them to the inner conditions, are reviewed below.

2.2.2 Mass, Radius, and the Equation of State

2.2.2.1 Neutron Star Radius

Measuring the radius of a neutron star is a challenging task with large uncertainties. Typically, the determination involves measurements of observed fluxes, distances, temperature models of the atmosphere, and the mass of the star. Despite accurate determinations of most of these values, the distance measurements often have large uncertainties, resulting in radius determinations with significant uncertainties (Burgio et al. 2021, pp. 41 f.). Nevertheless, there have been many attempts to measure the radius of neutron stars, some of them are listed in Table 2.2.

Table 2.2: Some notable neutron star radius measurements.

Radius [km]	Ref.	Notes
10.4 - 12.9	[1]	assuming a mass of $1.4\,M_\odot$
$9.1^{+1.3}_{-1.5}$	[2]	for a wide range of masses, thermal emission of quiescent low-mass X-ray binaries
10.45 to 12.66	[3]	assuming a mass of $1.4\,M_\odot$
9.4 ± 1.2	[4]	for six quiescent low-mass X-reay binaries
$12.36^{+0.38}_{-0.73}$	[5]	assuming a mass of $1.4\,M_\odot$
$11.96^{+0.94}_{-0.71}$	[6]	assuming a mass of $2.0\,M_\odot$

References. [1] Steiner et al. (2013), [2] Guillot et al. (2013), [3] Lattimer & Steiner (2014), [4] Guillot & Rutledge (2014), [5] Lim & Holt (2022), [6] Lim & Holt (2022).

In their study of rapidly rotating neutron stars, Suleimanov et al. (2020) found that the estimated radius of these stars may be overestimated. For SAX J1810.8−2609, they found radii ranging from 11.2 to 12.3 km, depending on the rotation rate and inclination angle. This sample of studies shows that the radius is not tightly constrained and could vary between 8 and 13 km, additionally depending on the mass of the neutron star.

2.2.2.2 Neutron Star Mass

The lower limit of the mass of the neutron star that can be reached in a supernova is about $0.8\,M_\odot$ (Steiner et al. 2013). This is in agreement with the lowest mass of a neutron star that has to date been measured by Doroshenko et al. (2022b) with a value of only $0.77^{+0.20}_{-0.17}\,M_\odot$ with a radius of $10.4^{+0.86}_{-0.78}\,$km. This mass was determined using a combination of X-ray spectrum modeling and an accurate distance estimate from Gaia. The central compact object (CCO) is therefore either the lightest neutron star measured yet or it might also be a strange star with an exotic core composition that was described above.

The upper limit of the neutron star mass is called the Tolman-Oppenheimer-Volkoff (TOV) limit. This limit, based on work by Tolman (1939), was originally determined by Oppenheimer & Volkoff (1939) to be about $0.71\,M_\odot$. Thus it lies below even the analogous Chandrasekhar limit for white dwarfs of about $1.4\,M_\odot$ (see Longair (2011, pp. 397 ff.) for a description). The estimate assumes that the neutrons form a degenerate Fermi gas, and only later works take into account the strong nuclear repulsion forces between neutrons, as well as other compositions of the neutron star material, and get considerably higher estimates of the maximum mass, between 1.5 and $3.0\,M_\odot$ (Bombaci 1996). Empirically, the masses of neutron stars can be measured precisely using pulsar timing (Longair 2011; Watts 2019; Steiner et al. 2013; Lorimer 2008). Some neutron star masses that have been measured are listed in Table 2.3.

Table 2.3: A few noteworthy neutron star mass measurements.

Mass [$M_\odot$]	Ref.	Notes
1.4408 ± 0.0003	[1]	Hulse-Taylor pulsar
1.35 ± 0.04	[2]	determined for 26 pulsars
1.97 ± 0.04	[3]	PSR J1614-2230
2.01 ± 0.04	[4]	PSR J0348+0432
1.908 ± 0.016	[5]	PSR J1614-2230 updated
$2.14^{+0.10}_{-0.09}$	[6]	PSR J0740+6620
2.35 ± 0.71	[7]	PSR J0952−0607

References. [1] Hulse & Taylor (1975), [2] Thorsett & Chakrabarty (1999), [3] Demorest et al. (2010), [4] Antoniadis et al. (2013), [5] Arzoumanian et al. (2018), [6] Cromartie et al. (2020), [7] Romani et al. (2022).

For more on the limiting masses and radii of neutron stars, refer to Drischler et al. (2021) and for summaries of neutron star mass measurements to Stairs (2004); Lattimer (2012); Özel & Freire (2016); Lattimer (2019); Wolff et al. (2021).

2.2.2.3 Simultaneous Mass and Radius Measurements

The mass and radius of neutron stars can also be determined simultaneously using pulse profile modeling. The method proposes that the mass and radius of a neutron star can be estimated from a model of its surface emission properties, taking into account relativistic effects. These effects include gravitational light bending, which reduces the modulation of the pulsed emission and depends on the compactness or mass-to-radius ratio of the star. Another effect is Doppler boosting, which creates an asymmetry in the pulse shape due to the rotation of the star and depends on the radius of the star. Therefore, by modeling the pulse shape, the mass and radius can be determined simultaneously, see Figure 2.6 for a visualization (Leahy et al. 2009; Watts et al. 2016; Bogdanov et al. 2019b; Watts 2019; Watts et al. 2019; Burgio et al. 2021; Wolff et al. 2021). In the case of Hercules X−1 (Her X−1), the mass-to-radius ratio was determined by calculating the pulse shape. This was done by assuming a surface emitting in the shape of a filled cone (Leahy 2004). The Neutron Star Interior Composition Explorer (NICER) onboard the International Space Station was built precisely with this as one of its main goals (Özel et al. 2016; Bogdanov et al. 2019a).

Table 2.4: Some notable neutron star mass and radius measurements made simultaneously. With the exception of the most recent measurement, all were determined using pulse profile modeling. For a more comprehensive overview of different techniques for simultaneous mass and radius measurements, along with sample sources, see Nättilä & Kajava (2022), specifically their Table 2.

Mass [$M_\odot$]	Radius [km]	Source Name	Ref.
$1.34^{+0.15}_{-0.16}$	$12.71^{+1.14}_{-1.19}$	PSR J0030+0451	[1]
$1.44^{+0.15}_{-0.14}$	$13.02^{+1.24}_{-1.06}$	PSR J0030+0451	[2]
$2.072^{+0.067}_{-0.066}$	$12.39^{+1.30}_{-0.98}$	PSR J0740+6620	[3]
$0.77^{+0.20}_{-0.17}$	$10.4^{+0.86}_{-0.78}$	HESS J1731−347 (CCO)	[4]

References. [1] Riley et al. (2019), [2] Miller et al. (2019), [3] Riley et al. (2021), [4] Doroshenko et al. (2022b).

Some notable recent simultaneous mass and radius measurements are listed in Table 2.4. The pulsar PSR J0030+0451 was studied by Riley et al. (2019) and Miller et al. (2019) independently with pulse profile modeling using NICER data. They use different emitting spot models, but found similar shapes and locations and their results are consistent. After the detection of pulsations from PSR J0740+6620 (Wolff et al. 2021), Miller et al. (2021) reports a radius of the neutron star of $13.7^{+2.6}_{-1.5}$ km, consistent with the $12.39^{+1.30}_{-0.98}$ km radius determined by Riley et al. (2021).
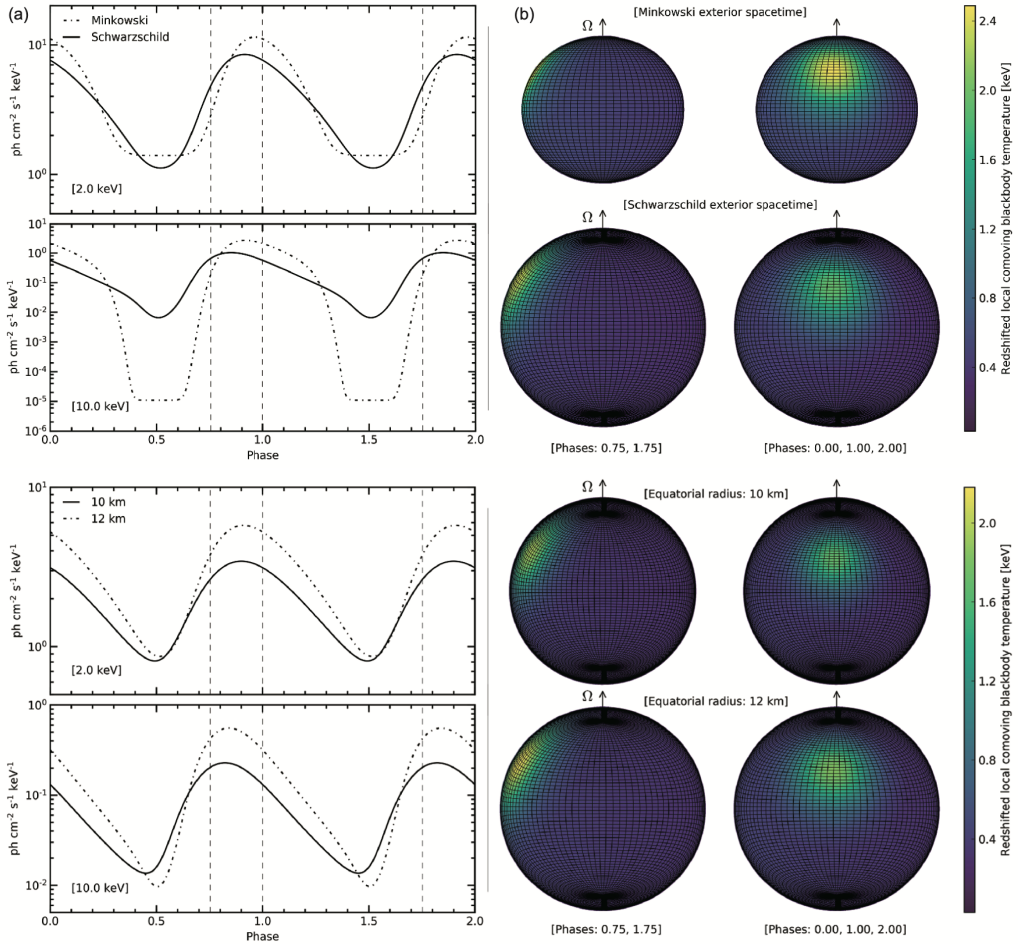
Figure 2.6: Top two rows: Relativistic effects can provide insight into the mass and radius of a neutron star by observing the pulse profiles. A comparison between Minkowski and Schwarzschild spacetime is shown for two energy bands. Bottom two rows: Pulse profiles in two energy bands for different radii, illustrating the sensitivity of the profile shape to the radius. The figure is adapted from Figures 4 and 5 in Watts et al. (2019).

2.2.2.4 The Equation of State

As explained in the section on neutron star structure (see Section 2.2.1), the composition of neutron star cores is essentially unknown. The presence of certain subatomic particles in the core remains unknown, making it difficult to establish a direct relationship between pressure and density in the core. This relationship, known as the equation of state (EoS), is key to understanding matter under extreme conditions and remains one of the greatest challenges in the field of neutron star physics (Haensel et al. 2007, pp. 14 ff., Camenzind 2007, pp. 189 f.).

The EoS for a neutron star at different densities is shown in Figure 2.7. Within the atmosphere, the EoS is governed by the ideal gas law at a given temperature, resulting in different solutions for different temperatures. In the deeper layers of the neutron star, the EoS is determined by the non-relativistic and relativistic electron gas. However, the EoS becomes highly uncertain in the core region of the neutron star (Watts et al. 2019, pp. 17 ff.).
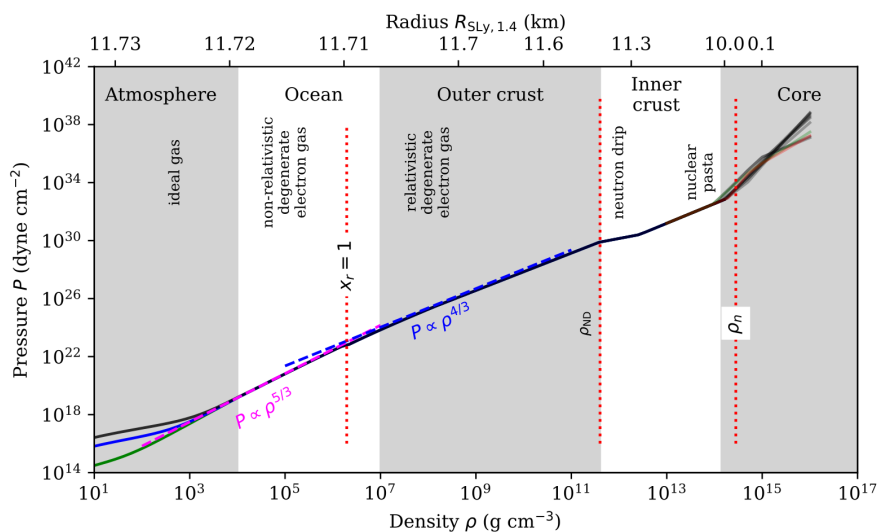
Figure 2.7: The equation of state (EoS) of dense matter in a neutron star, from the atmosphere to the core. In the atmosphere, the EoS is described by the ideal gas law, resulting in different solutions for different temperatures. In deeper layers, the EoS is influenced by the non-relativistic and relativistic electron gas. The equation of state in the core is unknown. For more information and the image source, see Watts et al. (2019).

One approach to meeting this challenge is to study the mass and radius of neutron stars, which have been discussed in previous sections. The pressure-density diagram in Figure 2.8 illustrates various model EoSs. By integrating the stellar structure equations,
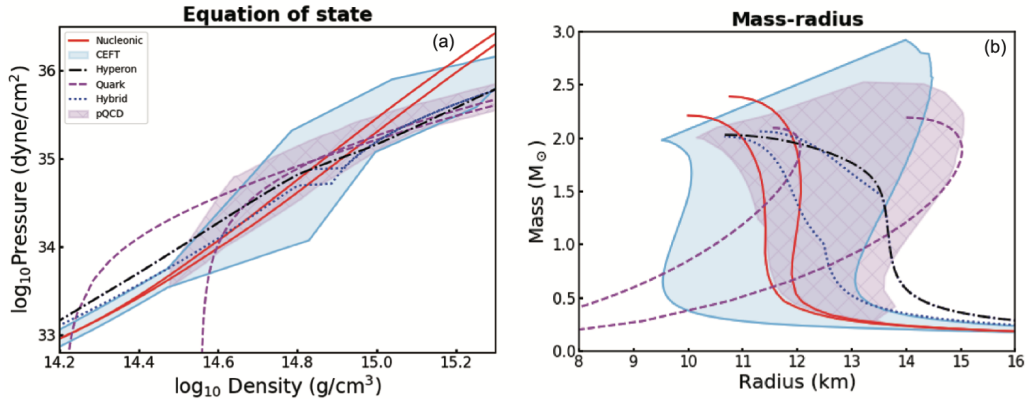
Figure 2.8: On the left is the pressure-density relation, with the equations of state for several example models describing the interior of a neutron star. By integrating the stellar structure equations, this relation can be used to determine the mass-radius relation, shown on the right. This can also be reversed and by determining the mass-radius relation, the equation of state can be mapped. The image is taken from Watts et al. (2019).

we can use the internal description of the EoS of the neutron star to determine external parameters such as mass and radius. Therefore, by accurately determining the mass and radius of a neutron star, we can also map its EoS (Watts 2019).

The large scatter and uncertainties in the radius and mass measurements, as discussed in Section 2.2.2.1 and Section 2.2.2.2, respectively, illustrate the limited understanding of the EoS for extremely dense matter. However, especially the measurements of high neutron star masses provide the strongest constraint on the nuclear EoS (Stairs 2004; Burgio et al. 2021). The maximum achievable mass, as well as the radius of a neutron star with a mass of 1.4 solar masses, are among the most significant yet unknown astrophysical quantities (Lattimer & Prakash 2004).

Figure 2.9 illustrates how the radius and mass measurements can help constrain the nuclear EoS. The multitude of possible EoS are shown in blue, the maximum mass constraints of neutron stars such as PSR J0740+6620 are used to reject EoSs, now displayed in gray. Further constraints can be imposed by NICER results of PSR J0030+0451, where the mass and radius have been determined, as discussed above. This greatly reduces the number of possible solutions. Refer to Dietrich et al. (2020) for more details on the procedure and the subsequent steps to further constrain the EoS that are not discussed here.

The study of the EoS of neutron stars is a very active area of research. The first results from NICER on simultaneous measurements of mass and radius show the potential for constraining the EoS. Expected future results promise to provide further insight into the

Potential equations of state in the mass-radius plane derived by chiral effective field theory. This theory serves as a means of determining nuclear forces from first principles.

The maximum mass constraints imposed by sources such as PSR J0740+6620, PSR J0348+4032, and PSR J1614-2230 constrain the equation of state. Only the blue ones agree with the observations.

The NICER mass-radius measurement of PSR J0040+0451 further restricts the equation of state set.

Figure 2.9: Schematic procedure for constraining the equation of state of a neutron star using measurements of its mass and radius. Only the part of the procedure involving neutron star mass and radius is shown. The allowed equations of state are shown in blue, while the rejected equations of state are shown in gray. The image is adapted from Dietrich et al. (2020).

internal composition of neutron stars and thus advance our understanding of supernuclear matter.

2.2.3 Pulsating Neutron Stars

The first evidence that neutron stars do in fact exist was the discovery of the first pulsar (pulsating radio source) by Jocelyn Bell Burnell and Anthony Hewish in 1967. The source was reported to rotate with a period of $1.3372795 \pm 0.0000020\,\mathrm{s}$ (Hewish et al. 1968). In order to make a pulsar, two things that are needed: rotation and a magnetic field. A star's rotation was measured as early as 1877 by Abney (1877a,b) using the broadening of lines in the spectra. Upon collapse, the star's radius is reduced to a fraction of the initial size and due to the conservation of angular momentum, the core spins up to the spin frequencies that are observed (Ott et al. 2006).

There are several ideas on the origin of magnetic fields in pulsars. The most common is the "fossil field" hypothesis. This hypothesis states that the neutron star magnetic field is simply a remnant of the progenitor star. However, at leas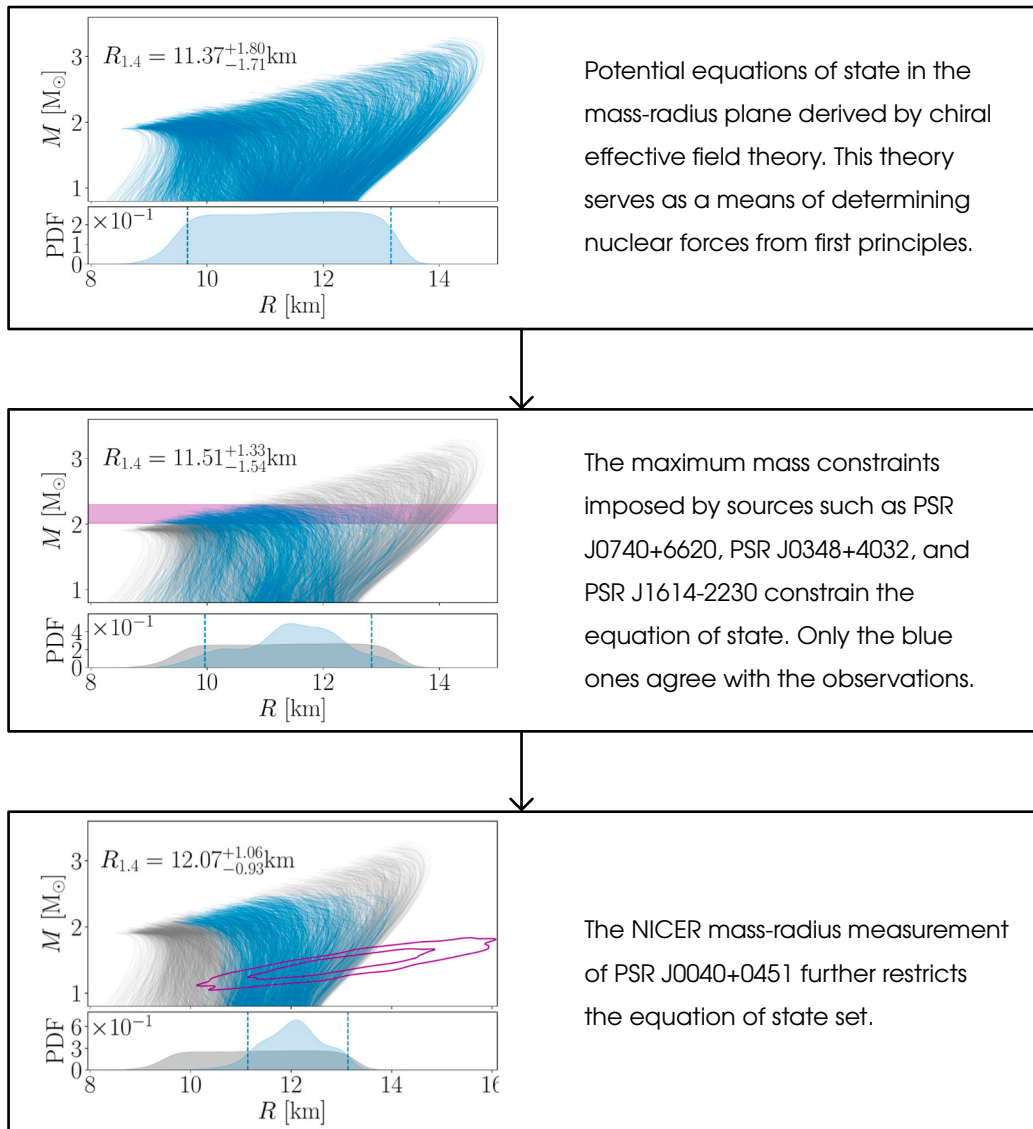t for magnetars, this idea is ruled out as the field strength needed of the progenitor main sequence star has to be larger than what we observe. For other pulsars, the magnetic coupling between the core and the outer layers of the progenitor should decrease the angular momentum from the core, which in turn would cause the remaining neutron star to have very long periods. To then explain the observed spin frequencies of pulsars, there would have to be "kicks" during formation that are spinning them up. The second idea is that the fields are generated internally in the supernova progenitor at an earlier stage, followed by an amplification during the core collapse, e.g. by flux conservation. However this is unlikely because the field strengths produced under this hypothesis are too low. The third idea is that the field is generated during the core collapse as a thermomagnetic effect in the neutron star crust. This effect is also likely not enough to produce the required field strength. Considering that the time of the collapse is very short and the initial field strength of the progenitor star is rather low, there has to be very efficient field amplification during the collapse (Spruit 2008). The observed strength of the magnetic field in pulsars is still under debate and an active area of research. For a review of the magnetic fields of neutron stars, see Konar (2017).

Radiation that is emitted at the magnetic poles of the neutron star, can be observed given a misalignment of the rotation and magnetic axis, given that the emission is within the line of sight of the observer. The resulting pulsations give pulsars their name. The pulsars found after the first discovery can be categorized into three main categories. It should be noted that the following list is not exhaustive, and some systems may have characteristics of several subtypes, so the classification is not always clear-cut. Some types may also represent different evolutionary stages of the same system. Ongoing research may result in further updates and modifications to the classification. The following list is therefore only intended to give a broad overview of the types of pulsars that exist. For

details on the following list, refer to Mason et al. (2009); Konar (2013); Konar et al. (2016); Konar (2017); Mushtukov & Tsygankov (2022).

Rotation Powered Pulsars (RPP) RPPs are powered by the loss of rotational energy due to magnetic braking.

- Classical radio pulsars (PSRs) are a type of rotation powered pulsar. The pulsations detected on Earth are caused by the build up of a large electrostatic field near the magnetic poles, leading to electron emission. The electrons are then magnetically accelerated along the field lines and produce synchrotron emission. The first pulsar discovered by Hewish et al. (1968) belongs to this category. PSR typically have rotation periods of about one second, magnetic field strengths of about 10^{11} to $10^{13.5}$ G and are powered by the loss of rotational energy due to magnetic braking.
- Millisecond radio pulsars (MSRPs) are a class of RPP with spin periods less than about 20 to 30 ms and and have low magnetic fields of less than 10^{10} G. It is likely that they have spun up to their observed spin periods by an accretion process in a binary system.
- Black widow (BW) and redback (RB) pulsars are classes of binary MSRPs that have strong pulsar winds and cause significant mass transfer from the companion star until the companion disappears, leaving the neutron star as an isolated millisecond pulsar.

Internal Energy Powered Neutron Stars (IENS) The mechanism that fuels IENS is thought to be related to an internal process, such as the decay of a magnetic field or residual heat of the supernova.

- Magnetars are young, isolated neutron stars powered by rotation. However, since they also have extremely strong magnetic fields of up to 10^{15} G, they are also powered by the decay of their magnetic fields.
- Soft gamma-ray repeaters (SGRs) and anomalous X-ray pulsars (AXPs) are likely magnetars at a different evolutionary stage. SGRs emit short bursts of γ- and X-rays at irregular intervals. AXPs on the other hand exhibit persistent X-ray emission with occasional γ-ray bursts.
- X-ray bright isolated neutron stars (INSs) and central compact objects (CCO) are powered through their residual thermal energy or the decay of the magnetic field. They are young, radio-quiet non-pulsating X-ray sources.
- Rotating radio transients (RRATs), similar to magnetars, belong to both the RPP and INES categories. These pulsars exhibit sporadic and infrequent single pulse radio bursts. Some RRATs also exhibit features such as nulling, a period of no detected radio emission, and mode changes.

Accreting X-ray Pulsars (XRP) XRPs, sometimes also called accretion powered pulsars (APPs), are neutron stars in binary systems that accrete matter from their companion star. The accretion process predominantly releases X-rays, and they are therefore called X-

ray binaries (XRBs). XRBs are typically classified according to their donor star properties and accretion mechanisms, and they exist in a variety of configurations. Since this thesis is concerned with the accretors in XRBs, these systems are introduced in the context of binary evolution in Section 2.3. At this point, we will only list the different types of XRBs for the sake of completeness. The details will be explained in the following section.

- Low-mass X-ray binaries (LMXBs) are binaries in which the companion star has a mass of less than about 2 solar masses. Some subclasses are Atoll sources, Z-type sources, and Millisecond X-ray pulsars.
- High-mass X-ray binaries (HMXBs) are binaries in which the companion star has a mass greater than about 10 solar masses. Some subclasses of HMXB are Be X-ray binaries (BeXRBs), Supergiant X-ray binaries (SgXRBs), and Supergiant fast X-ray transients (SFXTs).
- Intermediate-mass X-ray binaries (IMXBs) are binaries in which the companion star has a mass greater than about 2 and less than about 10 solar masses.

2.3 The Role of Binary Evolution for X-ray Pulsars

Section 2.1 covered the formation of neutron stars as endpoints in the stellar evolution of single high-mass stars. Now attention is turned to the evolution of binary systems and how this alters the evolution of each individual component star, with a special focus on binaries that have a neutron star as one component. In a binary system, mass might be transferred at some evolutionary stage between the two stars. This can happen when one star expands over time, when the orbit contracts, or via a stellar wind (Stairs 2004; Bhattacharya & van den Heuvel 1991). On the left side of Figure 2.10, the evolution of a binary star for a primary star of above 8 solar masses with a secondary star of about one solar mass is shown. Since the primary star, as the more massive one, will evolve faster beyond the main sequence (see Section 2.1), it will at some point undergo a supernova explosion leaving behind a neutron star, while the secondary will evolve more slowly on the nuclear timescale up to the red-giant branch of the Hertzsprung-Russell diagram (see Figure 2.1).

The combination of gravitational and centrifugal forces in a coordinate system co-rotating with a binary system results in equipotential surfaces. These surfaces are almost spherical and separate at low, very negative, potential values, centered on each of the components. Moving outwards from the two mass centers to higher potential values, the surfaces become more distorted and take on a pear shape until they touch at the inner Lagrangian point L_1 at a critical value. This point lies on the line connecting the two centers of mass of the binary system. As one binary component grows and fills its Roche lobe (RL), the net gravity at L_1 disappears and the pressure causes matter to flow out in a narrow stream. It then spirals in toward the compact object via a stable and long-lived (10^8 to 10^9 years) accretion disk and eventually be accreted by the neutron star, producing X-rays. Such mass transfer is called Roche lobe overflow (RLO; Bhattacharya & van den
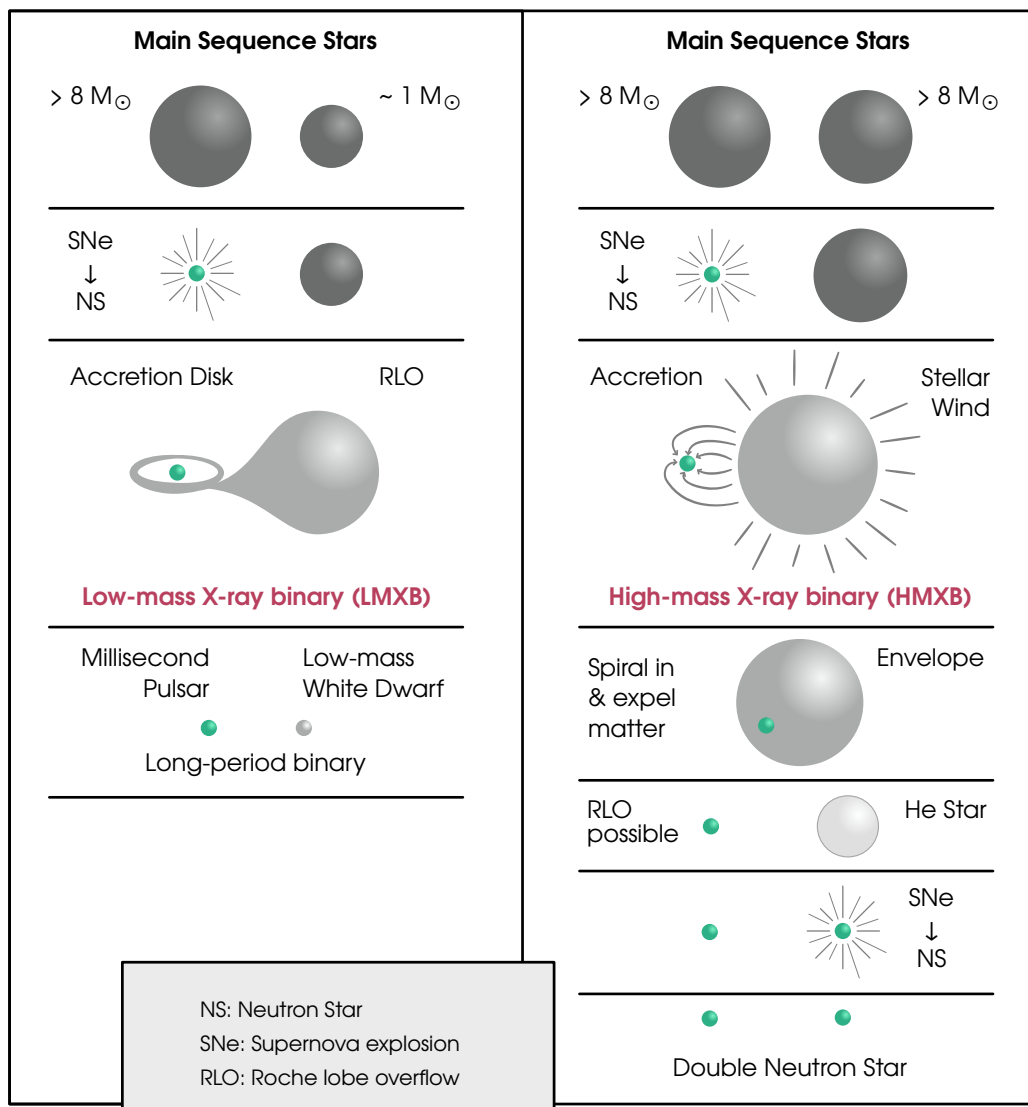
Figure 2.10: Two possible evolutionary paths of binary systems. The illustrations are not to scale. On the left are the evolutionary paths of a high-mass and a low-mass star. During its evolution it will pass through the low-mass X-ray binary (LMXB) phase. On the right is the evolution of two high-mass stars shown, which will pass through the high-mass X-ray binary (HMXB) phase. The image is based on Stairs (2004). It should be noted that these are very simplified scenarios and that more detailed evolutionary paths can be found, for example, in Iben (1991).

Heuvel (1991, pp. 41 ff.)). The system would then be visible as an X-ray binary (XRB).
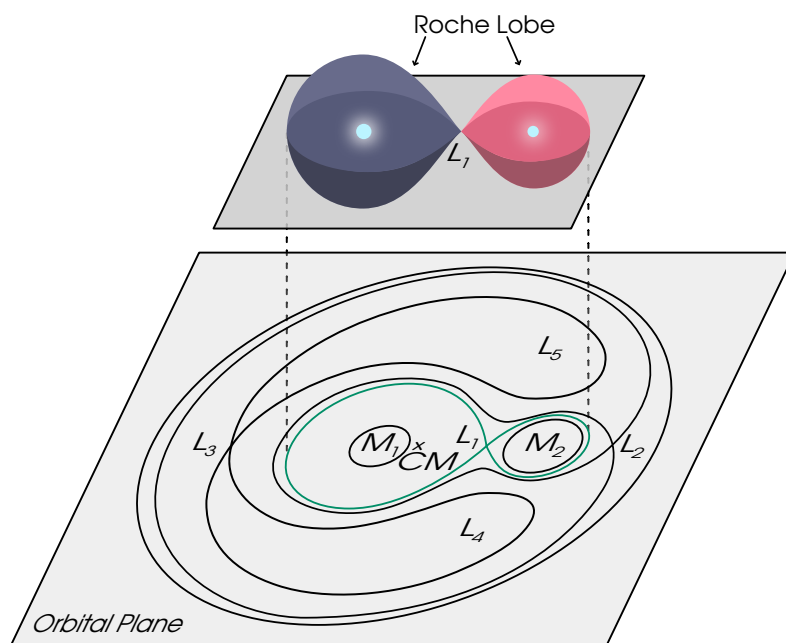
Figure 2.11: An illustration of the Roche lobe of a binary star can be seen on the top. The inner Lagrangian point L_1, where matter can flow from one star to another, is also shown. The bottom part of the picture roughly shows the equipotential lines a system like the top would have. The center of mass, CM, is close to the more massive star that has mass M_1. The other Lagrangian points in the system are shown in addition to L_1.

More specifically, since the companion in this case is a low-mass star with a mass less than the compact object, it is a low-mass X-ray binary (LMXB). The magnetic field of a neutron star in a LMXB is typically quite low, of the order of 10^8 G. The absence of regular X-ray pulsations indicates that the surface magnetic field is too weak to channel the accreted matter to well-defined magnetic poles on the stellar surface. If the field is very weak, the Alfvén surface, which is the region around a neutron star within which ionized gas is captured by its magnetic field, may almost coincide with the neutron star surface. Therefore, accretion may take place over a large part of the stellar surface. However, these sources often show time variability in form of X-ray bursts. The optical counterparts are faint, and their luminosities are one to four orders of magnitude lower than their X-ray luminosities. LMXB are typically older systems due to the low mass of the companion, and are therefore observed in greater numbers near the Galactic center. From the X-ray bursts, it can be deduced that the accreting objects are neutron stars with weak surface magnetic fields and that the bursts are most likely thermonuclear flashes occurring in the

accreted matter (Bhattacharya & van den Heuvel 1991, pp. 21 ff., 33 ff.). Three subclasses of LMXBs are the Z-type sources, Atoll sources, and Millisecond X-ray pulsars, which are classified based on their X-ray spectral and timing properties (Hasinger & van der Klis 1989; White & Zhang 1997). As the companion star keeps evolving, the final result of this evolutionary track would be a long-period binary system with a millisecond pulsar and a low-mass white dwarf companion (Stairs 2004).

The evolutionary track of two high-mass stars is shown schematically on the right side of Figure 2.10. One of the stars will first undergo a supernova explosion, leaving behind a neutron star. The other star, now the companion of the neutron star, has a mass which is greater than the neutron star, typically greater than $10\,M_\odot$. They are commonly bright and luminous early-type stars of spectral type O and B. The X-ray light curves might show eclipses, which allows to determine the orbital parameters of the system. Since the high-mass companion stars are short lived with ages $< 10^7$ yr, they belong to the youngest stellar population in the Galaxy and are therefore concentrated toward the Galactic plane but not the Galactic center (Bhattacharya & van den Heuvel 1991, pp. 21 ff.). The surface dipole magnetic field strengths of the neutron star are characteristically high of the order of about 10^{11} to 10^{15} G (Mushtukov & Tsygankov 2022). When the neutron star accretes matter from the companion, it releases X-rays and because of the high mass of the companion, the system is called a high-mass X-ray binary (HMXB). The first X-ray pulsar discovered was a HMXB, Centaurus X-3 (Cen X$-$3) by Giacconi et al. (1971a), for which Riccardo Giacconi received the Nobel Prize in Physics in 2002, in addition to his contributions to the Uhuru satellite.[1]

There are two main mechanisms of mass transfer in HMXBs, one is called atmospheric RLO, the other accretion from a strong stellar wind. As a star does not have a sharply defined radius, but instead there is an atmosphere in which the density exponentially decreases outwards, the RLO must start before the photospheric radius, which is defined at a distance where the optical depth is 2/3, meets the RL. The atmospheric matter will start to spill over through L_1 and this is called "beginning atmospheric Roche-lobe overflow" and it precedes the main phase of RLO. The mass loss will be roughly $1.5 \times 10^{-8}\,M_\odot\,yr^{-1}$. Accretion from stellar wind on the other hand is common for luminous early-type stars that have mass outflows with velocities of 10^3 km s^{-1}. For $20\,M_\odot$ stars and above, these mass losses happen on the main sequence during hydrogen core burning and the mass loss rates are about 10^{-8} or $10^{-9}\,M_\odot\,yr^{-1}$. The mass loss rates of early-type supergiants are significantly higher, about 10^{-6} to $10^{-5}\,M_\odot\,yr^{-1}$ (Bhattacharya & van den Heuvel 1991, pp. 21 ff., 33 ff.).

The outflows from massive supergiants are primarily driven by the absorption of

---

[1]Riccardo Giacconi got the Nobel Prize in Physics "for pioneering contributions to astrophysics, which have led to the discovery of cosmic X-ray sources". Source: The Nobel Prize in Physics 2002. `NobelPrize.org`. Nobel Prize Outreach AB 2023. Tue. 16 May 2023. `https://www.nobelprize.org/prizes/physics/2002/summary/`.

photons from the underlying photosphere. This is described by the CAK (Castor, Abbott, and Klein) model (Castor et al. 1975). The mass loss and acceleration of the wind are strongly dependent on several factors, including temperature, luminosity, radius, mass and effective surface gravity, although the precise values of these parameters are generally not known with certainty (Kretschmar et al. 2021). In a spherically symmetric configuration, the velocity of line-driven winds can be described by the β law, which determines how quickly the wind reaches its terminal velocity:

$$v = v_\infty \left(1 - \frac{r_*}{r} \right)^\beta ,$$

(2.6)

where

$\quad v_\infty \quad$ ...... terminal wind velocity,
$\quad r_* \quad$ ...... radius of the stellar photosphere,
$\quad r \quad$ ...... distance from the companion star, and
$\quad \beta \quad$ ...... gradient of the velocity field.

Due to the presence of internal shocks that can result from instabilities, the wind can form regions of higher density, or clumps. In the case of Vela X−1, for example, it is thought that a significant fraction of the wind is contained in clumps at a distance of one stellar radius from the photosphere (Kretschmar et al. 2021). Consequently, accretion to an X-ray pulsar would occur from a stellar wind that is at least partially clumpy in nature.

Mass accretion from a stellar wind was first calculated by Davidson & Ostriker (1973) based on the work of Bondi & Hoyle (1944). The accretion radius can be determined from

$$r_a = \frac{2GM}{v_w^2 + c_s^2} ,$$

(2.7)

where

$\quad G \quad$ ...... gravitational constant,
$\quad M \quad$ ...... mass,
$\quad v_w \quad$ ...... wind velocity, and
$\quad c_s \quad$ ...... speed of sound in the wind,

and the mass accretion rate can be approximated, given $c_s \ll v_w$, to

$$\dot{M}_a = \frac{G^2 M^2 \dot{M}_w}{d^2 v_w^4} ,$$

(2.8)

where

$\quad \dot{M}_w \quad$ ...... mass loss rate of the wind, and
$\quad d \quad$ ...... distance between companion and neutron star.

For a HMXB like Vela X−1, a fraction of about 2×10^{-5} of the wind mass will be accreted by the neutron star. This is a typical value for O and early B-type supergiants. The resulting accretion rate is about 10^{-11} to 10^{-10} $M_\odot$ yr^{-1}. As the accretion rate depends on v_w^{-4}, it is highly sensitive to the wind's velocity (Bhattacharya & van den Heuvel 1991, pp. 55 ff.).

There are two sub-types of HMXB, the "standard" HMXB, also known as supergiant X-ray binaries (SgXRB), and the HMXB with a B-emission type companion, also known as BeXRB (Bhattacharya & van den Heuvel 1991, pp. 29 ff.). In a SgXRB, such as Cen X−3 and SMC X−1, the companion star is an evolved giant or blue supergiant with a radius of about 10 to 30 $R_\odot$, luminosity exceeding 10^5 $L_\odot$ and mass greater than 20 $M_\odot$. Orbital periods in these systems are between around 1.4 and 10 days long. The accretion mechanism is likely the atmospheric RLO, i.e. from strong winds and stars nearly filling their RL. Finally, they are persistent, always observable, X-ray sources (Bhattacharya & van den Heuvel 1991). A sub-class of SgXRBs are Supergiant fast X-ray transients (SFXTs). These sources have low luminosities ($L_X \leq 10^{34}$ erg/s, Sidoli 2017) most of the time and exhibit short and bright flares lasting a few hours. Observational properties vary widely and the models proposed to explain them include clumpy wind accretion, propeller mechanism, and others (Mushtukov & Tsygankov 2022).

In contrast, BeXRB have unevolved companions with spectral types O5 to B9 with small radii of no more than about 5 to 10 $R_\odot$, luminosity less than about 10^4 $L_\odot$ and masses 8 to 20 $M_\odot$. The orbital periods in these systems are longer than SgXRBs with 10 days to several months, or up to several years. The companion is deep within the RL, there is no RLO and no enhanced winds. With some exceptions, for example X Per, LS I +61 235 (Haberl et al. 1998; Doroshenko et al. 2012), BSD 24-491 and LS 1698 (Reig & Roche 1999), BeXRB are transient, which means they can become unobservable or in an "off" state, for months to years. Then they may suddenly turn on as strong X-ray sources for weeks to months. The mass transfer must be due to intrinsic mass-loss properties of the Be components, such as stellar wind or mass ejection from the equatorial region. This produces the characteristic emission lines in optical spectra, which gives them the qualifier "e" in their spectral types. The rapid rotation of the Be star leads to a unique mass transfer phenomenon caused by the equatorial ejection of matter. This ejection is driven by the rotation of the star, and as material is ejected from its surface, it can form an equatorial disk. However, the exact mechanisms of the formation and dynamics of this disk are not fully understood. During its moderately to highly eccentric orbit, the neutron star in the BeXRB system encounters the circumstellar disk at periastron. During these encounters, the neutron star can accrete matter from the disk. This accretion mechanism is an example of wind accretion, where the neutron star captures material from the outflows of the Be star in the form of a disk (Bhattacharya & van den Heuvel 1991; Reig 2011).

In the following evolution, the slower evolving star might become a giant and, the

neutron star might spiral in and both stars might share a common envelope at this point. In the resulting neutron star and He-star tight binary system, matter might again overflow the Roche lobe and be transferred to the neutron star. The secondary star can then explode in a supernova and the result will be a double-neutron-star system in an eccentric orbit (Stairs 2004). For more details on the evolution of high-mass single and binary stars, refer to Iben (1991), Bhattacharya & van den Heuvel (1991) and Langer (2012).

3. Observables and Properties of X-ray Pulsars

Neutron stars in X-ray binaries (XRBs) can accrete matter from their companion star via stellar winds or Roche lobe overflow. In high-mass X-ray binaries (HMXBs), the accretion process is typically quasi-spherical, while in low-mass X-ray binaries (LMXBs) an accretion disk often forms around the neutron star. In highly magnetized neutron stars with magnetic fields of about 10^{12} G, as matter approaches the compact object, the magnetic field redirects the matter along the magnetic field lines to the magnetic poles. This is where the X-rays are produced, as the gravitational potential energy is released in the form of X-rays (see Section 3.1.2 for details). The observed pulsations occur due to the misalignment of the magnetic and spin axes when the observer is in the line of sight of the beams, and hence the objects are called X-ray pulsars (XRPs). Reviews on accreting XRPs can be found in White et al. (1983); Nagase (1989); Bildsten et al. (1997); Caballero & Wilms (2012); Mushtukov & Tsygankov (2022).

In this chapter, observables such as imaging, spectra, polarization, and light curves will be explored in relation to some of the physical properties of XRPs. Their pulse profiles will be introduced and the main challenges and complications involved in their formation are discussed. Finally, the modeling of these profiles will be reviewed and some state-of-the-art approaches for decomposing them will be presented.

3.1 Linking X-ray Observables to Physical Properties

X-ray astronomy is primarily concerned with the detection of individual photons. As a result, the data collected is in the form of event lists, containing entries such as the time of photon detection, its energy, and spatial information about its position on the detector, which can be converted into celestial coordinates. Some detectors, such as PCA on RXTE (see Section 4.2), are collimating and provide only limited spatial information. On the other

hand, more recently, polarization has emerged as another property that can be observed by some satellites, e.g. IXPE (Arnaud et al. 2011, p. 59).

The event lists are the raw data that must be processed to produce usable data analysis products. This typically requires dimensionality reduction, such as binning on the spatial axis to obtain images, which results in the loss of time and energy information. Spectra and light curve data products are obtained in a similar way. The following sections briefly discuss the different data products and the physical properties of XRPs that can be obtained (Arnaud et al. 2011, p. 75).

3.1.1 X-ray Images

When an image is acquired with a multi-pixel instrument, the spatial axis is binned, which typically results in a loss of energy and time information in the data. In astrophysics, imaging is primarily used to identify sources, distinguish between extended and point sources, detect structure in extended sources, and possibly observe variations with energy. However, X-ray imaging presents two challenges: the low count range and the varying point-spread function of the instrument on and off axis. Although it is not currently possible to obtain resolved images of XRPs due to their distance and size, imaging remains an important tool for analysis, as it allows the determination of source and background regions and their corresponding counts. The background counts must be taken into account in subsequent analyses. Although this is straightforward for high counts, it can be difficult for low counts because the background can be overestimated, resulting in unphysical negative counts. As a result, background subtraction may not always be possible, and analysis for source and background must be performed simultaneously. An example of a background extraction region is shown for an X-ray image taken with XMM-Newton's EPIC-pn detector in Figure 3.1, where the source region is defined as a circle around the center of the source, and the background region is also circular, but placed as far away from the source region as possible. Often, the background region can be defined as an annulus around the source region (Arnaud et al. 2011, pp. 105 f., 144 f.).

3.1.2 Spectral Analysis

X-ray instrument event files do not provide direct energy information; instead, they typically contain columns of pulse height amplitude (PHA) or PHA invariant (PI) information representing the energy levels of the recorded photons. The PHA can vary with time and detector location. When these variables are corrected, the new value, the PI, is obtained and can also be stored in the event list. The response matrix (RMF) can then be used to convert the PI to energy for analysis. However, when the spectral axis is binned to obtain a spectrum, the spatial and temporal information is lost (Arnaud et al. 2011, pp. 63, 77).

The following is a discussion of three topics often studied using spectral analysis in the context of XRPs. Note that the discussion is highly simplified and is intended only as
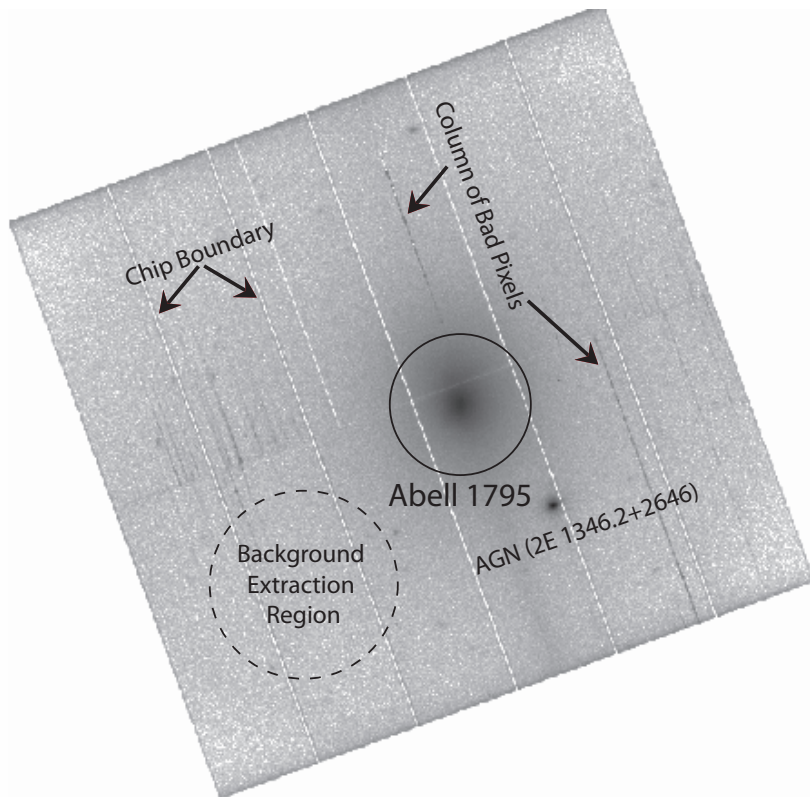
Figure 3.1: Example of an X-ray image taken with XMM-Newton's EPIC-pn detector (ObsID 0097820101), with the background and source regions indicated. Figure from (Arnaud et al. 2011, p. 97).

a general overview. The first topic is the broadband spectrum and its associated physical components, the second is the absorption lines in the spectra and what they can tell us about the companion's wind. Finally, the only direct measure of the magnetic field that we know of so far is also encoded in the spectrum in the form of a cyclotron resonance scattering feature (CRSF; Walter & Ferrigno 2017; Mushtukov & Tsygankov 2022).

Broadband spectrum: The broadband spectra of accreting XRPs can typically be described by a phenomenological model consisting of an absorbed power law with an exponential cutoff at high energies. The formation of XRP spectra involves a number of processes such as magnetic Compton scattering, cyclotron emission and absorption, and magnetic bremsstrahlung. For more information on this topic, see Wilms et al. (2000); Orlandini (2006); Piraino et al. (2007); Longair (2011); Caballero & Wilms (2012); Walter & Ferrigno (2017); Mushtukov & Tsygankov (2022), and references therein.

Absorption, stellar wind and chemical composition: By analyzing the lower energies of the XRP spectrum, we can determine physical properties of the accreting matter and the accretion flow, as well as the presence and properties of absorbing material along the line of sight. The amount of X-ray absorption between the XRP and the observer can be used to determine the location and properties of the absorbing material. By studying the spectrum over time, small scale variations can be detected and may indicate the presence of a structured or clumpy wind intermittently crossing the line of sight and increasing absorption. Another structure that can be studied by spectral analysis is the accretion wake, which is the region behind the XRP where the flow of matter is disturbed by the gravitational field of the accreting object. The accretion wake is characterized by its turbulent and chaotic nature, and studying its properties can provide insight into the dynamics of the accretion process. In addition to absorption features, broad emission lines associated with different elements in the accreting matter can be observed in the XRP spectrum. These lines can provide information about the velocity of the gas and the ionization state of the material (Kreykenbohm et al. 2008; Ducci et al. 2009; Malacaria et al. 2016; Grinberg et al. 2017; El Mellah et al. 2020; Diez et al. 2023).

Cyclotron Resonant Scattering Feature (CRSF) and the Magnetic Field: The magnetic fields of XRPs are among the strongest in the Universe and therefore have received much attention. Early estimations of the magnitude of the magnetic fields were based on the conservation of magnetic flux through the surface:

$$\Phi_{\mathrm{B}} = \int \mathbf{B} \cdot \mathrm{d}\mathbf{S} \, , \tag{3.1}$$

where $\mathrm{d}\mathbf{S}$ is a surface area element. The conservation of flux can be understood intuitively by looking at the magnetic field lines that pass through the surface of the star. Since the

number of lines remains the same, the total flux through the surface remains the same. Magnetic flux density is proportional to magnetic field strength, so a smaller area will have a higher flux density than a larger area. Thus, if the progenitor and the neutron star have the same number of field lines passing through their surfaces, but one has a smaller surface area, then the smaller one will have a higher flux density and a stronger magnetic field strength (Nättilä & Kajava 2022).

When estimating the magnetic field strength of the neutron star after the supernova, we need to consider the magnetic field strength of the progenitor, and the radii of the star before and after the explosion. The magnetic field strength of the progenitor might be on the order of one to 10^2 G. Just for comparison, the magnet of the iPhone 12 series that aligns the phone for wireless charging has a field strength of the order 10^2 G close to the surface (Seidman et al. 2021). The radius of the progenitor is about 10^{11} cm, which then contracts to the neutron star radius of about 10^6 cm. Given these order of magnitude estimates, the magnetic field strength should be amplified to about

$$B_{\mathrm{NS}} \sim B_{\mathrm{prog.}} \left(\frac{R_{\mathrm{prog.}}}{R_{\mathrm{NS}}} \right)^2 \sim 10^{10} \text{ to } 10^{12} \,\mathrm{G}. \tag{3.2}$$

However, there are some problems with this scenario. For example, the neutron star is formed from only about 15% of the progenitor's mass, and the radius used for the estimate should not include the entire progenitor radius. More sophisticated calculations, for example taking into account dynamo amplification, nonetheless predict comparable magnetic field strengths in the range of 10^{11} to 10^{15} G (Spruit 2008; Nättilä & Kajava 2022; Mushtukov & Tsygankov 2022).

In these strong magnetic fields, charged particles, in this case electrons, are strongly influenced by the Lorentz force. The motion of the electrons is confined to quantized circular orbits perpendicular to the magnetic field lines and their energy is quantized, they can only occupy certain energy levels called Landau levels. The radius of the orbit is called the gyroradius or cyclotron radius and the angular frequency of the electrons is given by

$$\omega = \frac{eB}{m_e c} \,, \tag{3.3}$$

where

e ...... electron charge,
B ...... magnetic field strength in the scattering region,
m_e ...... electron mass, and
c ...... speed of light.

Thus, Landau levels are linearly related to the strength of the magnetic field. Near the magnetic poles of accreting neutron stars, the kinetic energy of the infalling material is

converted into X-rays. These X-rays can undergo resonance scattering, i.e. the absorption and immediate re-emission of photons of a certain energy, on the quantized electrons, leading to the generation of resonance absorption features in the X-ray spectrum. These features are called cyclotron resonance scattering features (CRSF; Longair 2011; Walter & Ferrigno 2017; Staubert et al. 2019; Mushtukov & Tsygankov 2022). The observation of such features then allows a direct measurement of the magnetic field strength using the centroid energy of the CRSF (Staubert et al. 2019):

$$E_{\text{cyc}} = \hbar\omega \frac{n}{1+z} \approx 11.6 \,[\text{keV}] \times \frac{n}{1+z} B_{12} \,, \tag{3.4}$$

where

$\quad B_{12}$ ...... magnetic field strength in units of 10^{12} G,

$\quad z$ ...... gravitational redshift caused by neutron star mass, and

$\quad n$ ...... number of Landau level.

In practice, the CRSF is often described by a multiplicative gaussian absorption line model (Mushtukov & Tsygankov 2022). The detection of a CRSF was first reported by Truemper et al. (1978) and since then they have been extensively studied. A review of XRP magnetic field strengths that have been determined using the CRSF can be found in Staubert et al. (2019). In addition to its strength, any observed variation in the CRSF can point to the dynamics of the accretion flow and its inhomogeneous nature (Walter & Ferrigno 2017, p. 8). The general consensus is that the CRSFs are formed in the hot, magnetized plasma surrounding the magnetic poles of the accreting neutron star (Staubert et al. 2019). However, observations of the correlation between the cyclotron line and luminosity have led to new theories regarding the exact location of these line-forming regions (Mushtukov & Tsygankov 2022). These observations are categorized with the critical luminosity as a reference (Basko & Sunyaev 1976; Mushtukov & Tsygankov 2022):

$$L_{\text{crit}} \approx 4 \times 10^{36} \left(\frac{\sigma_{\text{T}}}{\sigma_{\text{eff}}} \right) \left(\frac{l_0}{2 \times 10^5 \,\text{cm}} \right) \left(\frac{10^6 \,\text{cm}}{R} \right) \left(\frac{M}{M_\odot} \right) \text{erg s}^{-1} \,, \tag{3.5}$$

where

$\quad \sigma_{\text{T}}$ ...... Thomson scattering cross section,

$\quad \sigma_{\text{eff}}$ ...... effective cross section in accretion channel,

$\quad l_0$ ...... length of accretion channel base,

$\quad R$ ...... radius of the neutron star, and

$\quad M$ ...... mass of the neutron star.

Below this critical luminosity, accretion is considered sub-critical, and this sub-critical luminosity is associated with a positive correlation between CRSF and luminosity that has

been observed in a number of sources, such as Her X−1 (Staubert et al. 2007), GX 304−1 (Klochkov et al. 2012; Rothschild et al. 2017), and GRO J1008−57 (Chen et al. 2021). There are two ideas that could explain this observation, see Figure 3.2 for illustrations. The first is based on a collisionless shock. The height of the shock above the surface of the neutron star is anticorrelated with the mass accretion rate. The higher the mass accretion rate, the closer the shock is "pushed" to the surface, and the cyclotron energy probes the matter closer to the surface, which means a higher magnetic field (case A in Figure 3.2). The other idea on how to explain a positive correlation is to assume hotspots on the surface and the velocity at which the accretion flow approaches the neutron star surface (case B in Figure 3.2). This idea is best understood by considering that the cyclotron energy is always redshifted. The observation of the positive correlation of cyclotron energy with luminosity then leads to the question of why the cyclotron line is *less* redshifted at higher luminosities than at lower luminosities. In general, when matter approaches the surface of the neutron star at high velocity, the resonance scattering line appears redshifted as the electrons move toward the surface. The cyclotron line is therefore observed at lower energies than the magnetic field near the surface would imply. The amount of redshift depends on the velocity of the electrons. The faster they are, the higher the redshift, and the lower the energy of the line is observed. As the luminosity increases, the electrons are slowed down by the increased radiation pressure. This means that the electrons move more slowly, there is less Doppler redshift, and the line moves to higher energies. This would explain a positive correlation between observed line energy and luminosity (Mushtukov et al. 2015c; Mushtukov & Tsygankov 2022).

Above the critical luminosity (Equation 3.5), the accretion is super-critical, and a radiation-dominated shock can form above the surface of the neutron star. A negative correlation between CRSF and luminosity is associated with this regime and considered a strong indication of super-critical accretion. Such a negative correlation has been observed in 4U 0115+63 (Mihara et al. 2004) and V 0332+53[1] (Tsygankov et al. 2006). There are two theories to explain the negative correlation. The first considers the radiation-dominated shock above the surface (case D in Figure 3.2). At higher mass accretion rates, and thus at higher luminosity, the shock will form at a greater distance above the surface. The magnetic field strength decays as $B \propto r^{-3}$ with distance r, so the higher the shock forms, the lower is the magnetic field strength. Hence the negative correlation. The problem with this model is that the line-forming region could be very large, and thus the cyclotron feature should be very broad or disappear. Also, small variations in height should significantly affect the energy, which is not observed. Therefore, a second theory has been proposed to explain the negative correlation. In this model, the CRSF forms as a reflection of the X-rays in the atmosphere of the neutron star (case E in Figure 3.2). The higher the luminosity, the

---

[1]In fact, both a positive and a negative correlation were reported in V 0332+53, see Doroshenko et al. (2017); Vybornov et al. (2018).

Sub-critical case and the positive correlation

(A) Collisionless shock
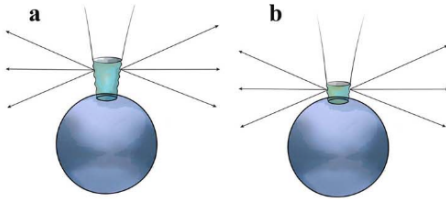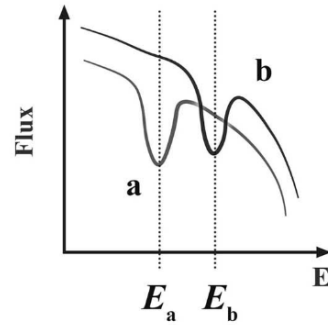
(B) Doppler effect in accretion channel
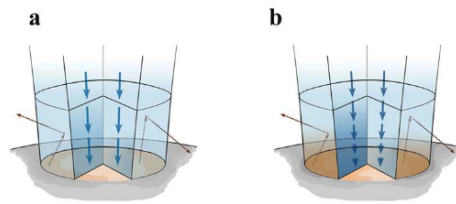
Super-critical case and the negative correlation

(D) Cyclotron line from accretion column
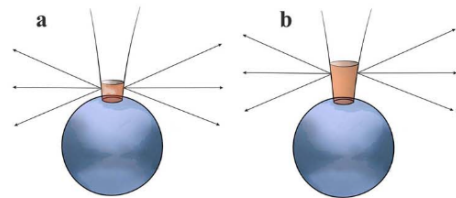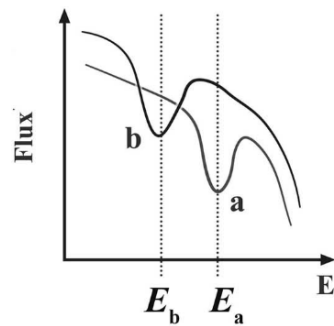
(E) Cyclotron line due to reflection
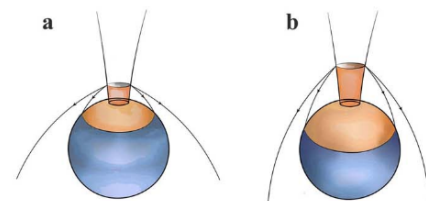
Figure 3.2: Two theories to explain the positive correlation between luminosity and cyclotron energy in X-ray pulsars are a collisionless shock (A) and the Doppler effect in the accretion channel (B). The observed negative correlation could be explained by the accretion column (D), or by a cyclotron line formed by reflection from the neutron star surface (E). See text for details. Image from Mushtukov & Tsygankov (2022).

higher the accretion column, and thus the larger the fraction of the neutron star's surface that is illuminated by X-rays. Since the magnetic field strength decreases towards the equator, the average magnetic field decreases with increasing luminosity (Mushtukov & Tsygankov 2022).

Note that the CRSF is an indication of the magnetic field, but does not necessarily measure the dipole field strength at the poles. Instead, it measures the local field strength wherever resonant scattering occurs. This has already been implied by the theories mentioned above to explain positive and negative correlations of cyclotron energy with luminosity, e.g. the height of an accretion column shifts the location of the scattering region. But the field strength itself could also be altered by the geometry near the polar cap (Mukherjee & Bhattacharya 2012), or another possible deviation from the actual field strength is the potential presence of multipole components. For Her X−1 the measured cyclotron energy was higher than expected from modeling. A possible explanation for this could be that the field structure near the neutron star surface contains higher multipole moments with stronger magnetic field strengths than the overarching dipole field (Staubert et al. 2019).

Long et al. (2007) investigated the effect of higher multipole components on accretion using simulations. They found that dipole and quadrupole fields produce funnels and hotspots on the surface with distinct features. For example, in the case of a dipole field, matter is accreted in two funnels, producing arc-like hotspots near the pole. In the quadrupole field, accretion occurs in a belt along the magnetic equator. NGC 5907 (Israel et al. 2017) as well as SMC X-3 (Tsygankov et al. 2017) exhibit signs of significant contributions from non-dipolar components to their magnetic fields (Mushtukov & Tsygankov 2022).

3.1.3 X-ray Polarimetry

In general, an electromagnetic wave consists of an oscillating electric field and an associated perpendicular magnetic field, and the direction of propagation is perpendicular to both fields. The orientation in which the electric field oscillates is called polarization. If light is unpolarized, the electric field oscillates randomly in all directions perpendicular to the direction of propagation, and in polarized light, it oscillates in a specific direction.

Birefringence is a polarization dependent phenomenon, the best known example of which is double refraction. In birefringent materials, the index of refraction varies with the direction of polarization of the light, causing the light to have different paths. The two paths are called ordinary and extraordinary. The optic axis of a birefringent material is the direction of rotational symmetry with respect to the optical behavior of the material. This optic axis and the propagation direction of the photon form a plane. When the electric field oscillates parallel to this plane, it is called the ordinary mode. The extraordinary mode consists of light whose electric vector is perpendicular to the plane. As a result, the ordinary and extraordinary rays follow different paths (Becker &

Wolff 2007), see Figure 3.3 for a sketch. Birefringence in crystals can be explained by the
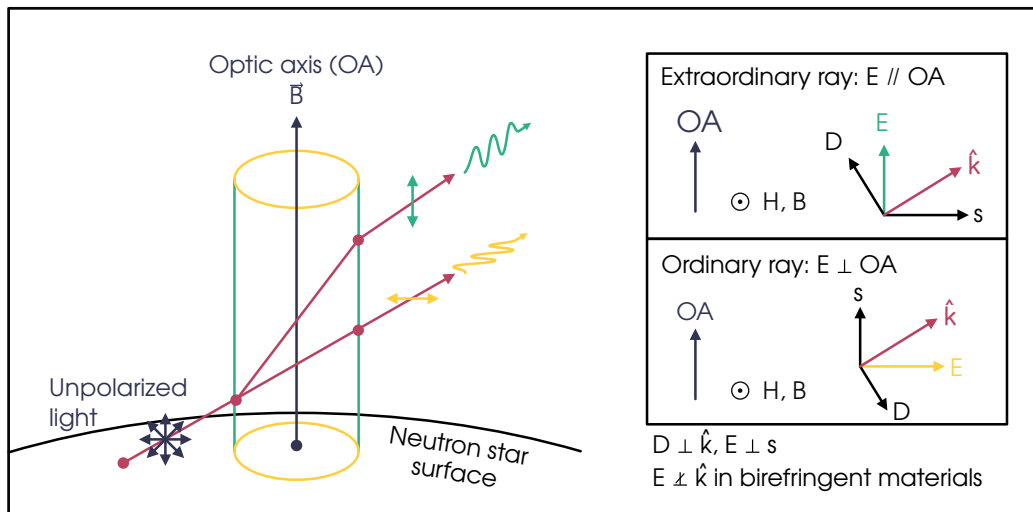

Figure 3.3: The plasma surrounding the emission region of a neutron star becomes strongly birefringent due to its strong magnetic field. In this case, the optic axis (OA) is parallel to the magnetic field. When unpolarized light passes through the birefringent plasma, it is split into two modes: the ordinary mode, where the electric field intensity (E) is perpendicular to the optic axis, and the extraordinary mode, where the electric field intensity is parallel to the axis. In the right insets, the magnetic flux density (B) and the magnetic field intensity (H) are perpendicular to the plane of the paper. It is important to note that in birefringent materials, the electric field intensity (E) is not perpendicular to the wave-normal ($\hat{k}$), but perpendicular to the ray (s) defined by E × H. In addition, the electric displacement field (D) is always perpendicular to the wave-normal.

structure of their lattice. If the lattice structure of a crystal is more tightly packed in one direction than in another, this can result in different refractive indices of light. Birefringent materials have two different refractive indices, unlike isotropic materials, which have only one refractive index that is independent of polarization (Nättilä & Kajava 2022, p. 30). In strongly magnetized environments, such as near the surface of a highly magnetized neutron star, vacuum birefringence, a quantum electrodynamic (QED) phenomenon, can occur. This phenomenon arises from the presence of virtual electron-positron pairs that spontaneously appear and then annihilate. In the strong magnetic field, the temporarily appearing charged particles rotate around the magnetic field, creating an imaginary crystal lattice in the vacuum. As a result, the vacuum can have different refractive indices along and perpendicular to the magnetic field, which changes how light can pass through it. Near the emission regions of XRPs (see Figure 3.3) this vacuum birefringence can significantly

affect how photons propagate through the magnetic field, and the emitted radiation may therefore be aligned with the magnetic field, and the ordinary and extraordinary modes can have very different scattering cross-sections (Mushtukov et al. 2015b), as can be seen in Figure 3.4 (Nättilä & Kajava 2022, p. 30, Mushtukov & Tsygankov 2022, p. 50, Harding & Lai 2006, pp. 16 ff., Becker & Wolff 2007).
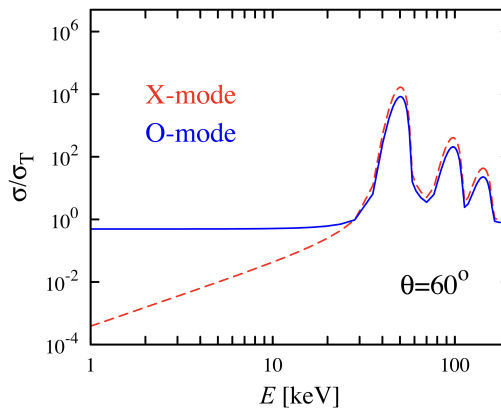
Figure 3.4: The energy dependent total Compton scattering cross-section is shown for the two polarization modes for an angle θ between the initial momentum direction and the magnetic field. Figure from Mushtukov et al. (2015b).

In addition to birefringence, polarization-dependent processes such as photon-electron scattering can occur in the emission regions of XRPs. When unpolarized light scatters off free electrons, known as Thomson scattering, the scattered light can become polarized depending on the orientation of the electron's magnetic field. Therefore, the radiation from the emission regions is expected to be polarized (Mushtukov & Tsygankov 2022; Becker & Wolff 2007). Studying the polarization of the radiation emitted by XRPs can provide valuable information about the emission geometry and the accretion flow. For example, depending on the strength of the magnetic field and the accretion rate, X-rays may be emitted in a "pencil" or "fan" beam (the details of which will be discussed in Section 3.2.1). Studying the polarized light can help distinguish between these geometries and identify the origin of the X-rays (Rees 1975). Polarization can also probe details of the accretion flow. At low energies, below about 10 keV, the polarization can change abruptly due to absorption of the X-ray emission by clumps of matter (Elsner & Lamb 1976). Furthermore, as the pulsar rotates, the angle and degree of polarization should change. By observing these changes, we can place constraints on the orbital parameters, such as the inclination, and reduce uncertainties in measurements of the mass and radius of neutron stars (Rees 1975; Watts et al. 2019).

The Imaging X-ray Polarimetry Explorer (IXPE, Weisskopf et al. 2022) was launched

on December 9, 2021 and has already provided numerous results. Her X−1 shows a significant polarization signal, although the degree of polarization of about 10% is well below the expected level. Nevertheless, the degree and angle of polarization allowed the determination of the spin position, magnetic obliquity, and misalignment of the spin axis of the neutron star and the angular momentum of the binary orbit (Doroshenko et al. 2022a). When the polarization was examined in combination with a spectral analysis in different states (i.e., main-on and short-on of the super-orbital period), the results supported the notion that the neutron star could be partially obscured from the line of sight by a warped accretion disk. During this period, a change in the degree of polarization could be explained by the partial obscuration of one of the magnetic poles (Garg et al. 2023).

Similarly, a study of Cen X−3 allowed the geometry of the system to be determined, including the pulsar's spin-position angle and magnetic obliquity. The analysis also provided insight into the neutron star's atmosphere and raised questions about the reflection of radiation from different parts of the system, such as the neutron star surface or accretion curtains (Tsygankov et al. 2022). In the case of Vela X−1, a low degree of polarization was detected, supporting previously reported ideas about the structure of the neutron star's atmosphere (Forsblom et al. 2023).

The polarization results of Tsygankov et al. (2023) and Mushtukov et al. (2023) determined the geometry of the transient XRP GRO J1008−57 and the persistent source X Persei, respectively, suggesting that they may be nearly orthogonal rotators. In addition, the polarimetric study of EXO 2030+375, combined with spectral and timing analysis, indicated that the accretion geometry in this source is highly complex, including asymmetric magnetic multipoles (Malacaria et al. 2023).

These polarimetric studies of XRPs highlight the importance of X-ray polarimetry in the study of these systems and the potential for future missions, such as the Enhanced X-ray Timing and Polarimetry (eXTP, Zhang et al. 2019) mission.

3.1.4 X-ray Light Curves

When energy and spatial information are discarded in the event list, the resulting light curve can provide information about the properties of XRBs through their time variability. Pulsations are observed when the emission region crosses our line of sight, which occurs on the timescale of the neutron star's rotation. By averaging the flux over several rotation periods, a pulse profile is obtained. Since this key feature is a central part of this thesis, it will be discussed in a separate section, along with its physical implications (Section 3.2). The spin-up and spin-down behavior of some XRPs, related to changes in the rotational period of the neutron star, should only be mentioned here. These changes can be explained by accretion torques transferred from the accreted matter to the neutron star, and are described by the coupling of the matter to the magnetic field, as introduced in Ghosh & Lamb 1979b (Fürst et al. 2019).

The orbit of the neutron star around its companion defines the orbital period. When the inclination of the system is high, the orbit can be followed by eclipses, which cause dips in the light curve. In Be-systems the orbit is more likely to be traced by bursts as the neutron star passes through the circumstellar disk. In both cases the observations help to determine the orbital ephemeris. However, a better approach is to use pulse timing, which takes advantage of the Doppler shift in the rotation period of the neutron star throughout the orbit (Fürst et al. 2019).

A super-orbital period is observed as a change in the orbital period over time. This phenomenon has been observed in Her X−1 and SMC X−1 and has been associated with a precessing and warped accretion disk (Iping & Petterson 1990; Staubert et al. 2006). However, observations of supergiant systems have challenged the theory of a precessing accretion disk. Therefore, the super-orbital period is not fully understood and remains an active area of research (Fürst et al. 2019).

In addition to the periodic variability mentioned above, XRP light curves also exhibit aperiodic variability, also known as flickering. This type of variability is typically associated with variations in the accretion rate. For example, the log-normal distribution that is observed can be explained by larger clumps of matter breaking up into smaller clumps that eventually accrete. The power spectra[2] of XRPs are characteristic of accretion processes and follow a power law up to a break frequency, beyond which they show a power law with a steeper slope, see Figure 3.5. Both the power density spectrum and the break frequency are luminosity dependent. This is mainly due to the variable rate of mass accretion onto the surface of the neutron star. It therefore provides information about the geometry and physical conditions of the accretion, including wind or disk accretion, the size of the accretion disk, or instabilities. In addition, the break frequency is associated with the magnetosphere, which means that it can be used to estimate the magnetic field strength (Fürst et al. 2019). For more information on flicker noise, see Lyubarskii (1997), on power density spectra of XRPs, see Revnivtsev et al. (2009), and for other aspects of aperiodic variability, refer to Walter & Zurita Heras (2007); Ducci et al. (2009); Fürst et al. (2010); Mönkkönen et al. (2022); Mushtukov & Tsygankov (2022) and references therein.

3.2 Understanding Pulse Profiles of X-ray Pulsars

The magnetic field of a neutron star plays an important role in accretion, and its effect depends on the distance from the surface. At great distances, the magnetic field has a minimal effect on the accretion flow, allowing matter to approach the neutron star in a disk or spherical configuration. Closer to the surface, however, the magnetic field dominates and controls the way the gas flows. The radius of the magnetospheric boundary, known as the Alfvén radius, determines where the magnetic field begins to control the flow. Inside this

---

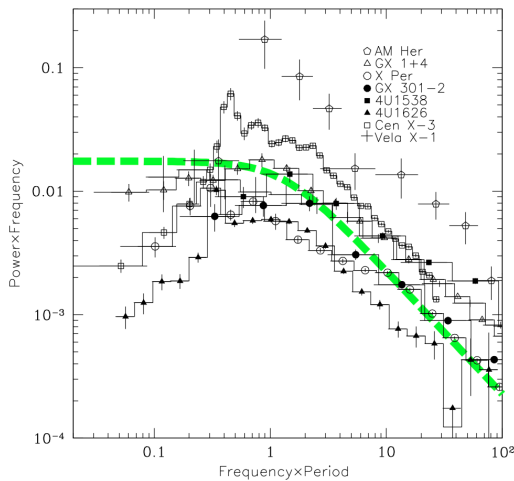[2]A power spectrum is the distribution of signal power versus frequency.

Figure 3.5: Power density spectra of several accreting X-ray pulsars, along with a model shown as a green dashed line, with the x-axis in units of the neutron star's spin frequency. The spectra show aperiodic variability over a wide range of frequencies, including the spin frequency, and can be described by a broken power law with a break around the pulse frequency. This image is taken from Revnivtsev et al. (2009).

radius, the magnetic field lines direct the matter to the surface of the neutron star. Exactly how this happens is a complex problem. The basic idea is that a standing shock near the Alfvén surface stops the accretion flow, and the matter can tunnel down to the magnetic poles through a narrow accretion column. The cross-sectional area of the accretion column can be estimated from the last undistorted dipole field lines, which should be close to the Alfvén surface, and is about 10^{10} cm^2. This means that it is about 1000 times smaller than the surface of a neutron star with a radius of 10 km, i.e. about 10^{13} cm^2 (Shapiro & Teukolsky 1986, pp. 451 ff.).

In many cases, the entry of matter into the magnetosphere can be affected by Rayleigh-Taylor instabilities, leading to a larger cross-sectional area of accretion near the magnetic poles. More information on this can be found in Arons & Lea (1976, 1980); Elsner & Lamb (1976, 1977). This is one of the challenges described in Section 3.2.1 related to pulse profile formation. The details of the accretion process are the subject of ongoing research. Early studies examined accretion in the presence of an accretion disk for a slowly rotating neutron star, details of accretion in the context of rotating neutron stars, and how the radiation produced escapes, possibly sideways from the base of the accretion funnel, and then reflects off the surface of the neutron star (Pringle & Rees 1972; Lamb et al. 1973; Davidson & Ostriker 1973). Regardless of the details, the X-ray emission typically originates near the polar cap and is therefore highly anisotropic. For an oblique rotator

with a misaligned rotational and magnetic field axis, there is an off-axis spot on the surface that produces X-ray pulsations (Shapiro & Teukolsky 1986, pp. 451 ff.). The observed intensity modulation, which occurs on the time scale of the rotation period, can be averaged over the phase, and the light curve folded with the spin period is called the pulse profile. Although this general concept of how pulse profiles are formed was understood early on, the details of the process and the observation of pulse profiles that vary with energy and luminosity have raised questions about this model (for a brief overview see e.g. Fürst et al. 2019; Mushtukov & Tsygankov 2022). One of the major challenges in understanding XRP emission is the inability of terrestrial laboratories to reproduce the complex interplay between extreme gravity, radiative processes, and magnetic fields that occurs in these astrophysical systems.

In Section 3.2.1 we will examine some of the key aspects and challenges that arise in the formation of pulse profiles. This is followed by a section on pulse profile modeling from a theoretical perspective and some state-of-the-art observational methods in Section 3.2.3.

3.2.1 Key Challenges and Complications

The pulse profiles of accreting X-ray pulsars are shaped by several factors that can be grouped into four categories. These factors include the geometrical configuration of the system; the spatial distribution and emission footprint, which is primarily affected by the magnetic field and instabilities that determine how and where the matter meets the surface of the neutron star; the vertical emission structure, which is determined by the rate of mass accretion; and finally, the modifications that the emitted X-rays undergo as they travel away from the neutron star.

I. Geometric Configuration: Observing pulsations and therefore pulse profiles of XRPs requires a misalignment between the spin axis and the magnetic axis. The geometric configuration, sketched in Figure 3.6, is characterized by two angles. The first is the angle α between the spin axis and the orbital axis, which is usually aligned with the disk axis in the presence of an accretion disk. The second angle θ, known as the magnetic obliquity, is defined as the angle between the spin axis and the magnetic moment.

The effect of geometry on pulse profiles can be seen, for example, by examining the shape of hotspots in disk accretion. The configuration of these hotspots depends on the magnetospheric radius and the magnetic obliquity. When the angle exceeds about 30 degrees, the hotspots have a circular shape. However, when the angle is smaller, the hotspots tend to be less circular and take on a more bow-shaped appearance, curving around the magnetic pole (Romanova et al. 2004).

In addition to the aforementioned angles, the observer's line of sight to the system is important in determining the observable parts of the neutron star and the emitted X-rays, after taking into account the effects that modulate their propagation, which will be discussed below (Meszaros et al. 1988; Biryukov & Abolmasov 2021).
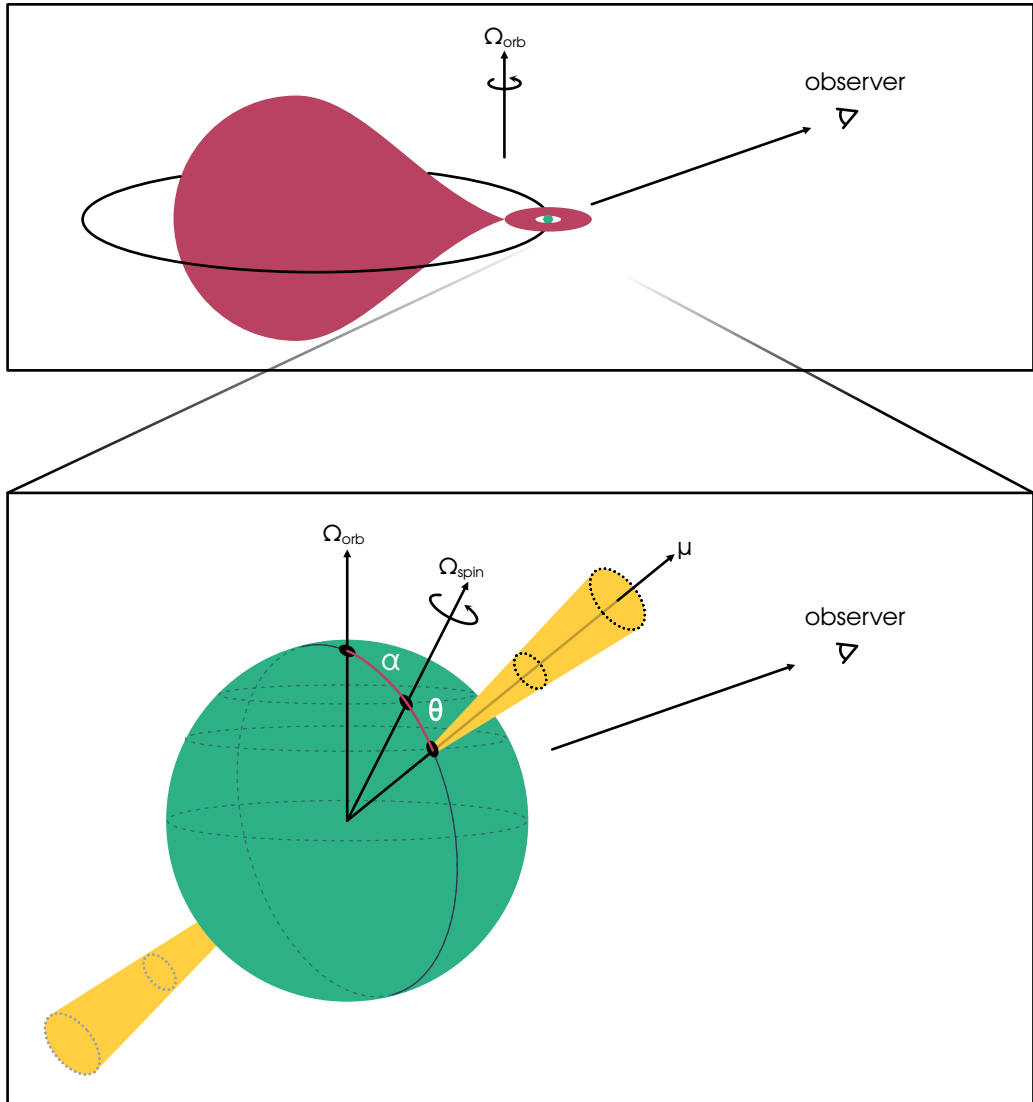
Figure 3.6: The geometric configuration of an XRP (not to scale). The top part of the sketch shows a Roche-lobe overflow system. The orbital axis (Ω_{orb}), which is typically aligned with the disk axis, and the observer's line of sight are shown. The lower part of the image shows the neutron star with its spin axis (Ω_{spin}) and magnetic moment (μ). The configuration is characterized by two angles: the first angle, denoted α, is the angle between the spin axis and the orbital axis, while the second angle, known as the magnetic obliquity θ, is the angle between the spin axis and the magnetic moment.

II. Spatial Distribution and Emission Footprint: The matter falling onto the surface of a neutron star shapes the pulse profile by converting gravitational potential energy into X-rays. The observed pulse profile is an integration of the total flux visible to the observer, which means that all locations where the matter hits the surface contribute. The specific locations depend on the geometry and magnetic field configuration (Romanova et al. 2003, 2004).

In the case of spherical accretion, matter approaching the magnetosphere is stopped at its boundary and can enter through Rayleigh-Taylor instabilities, similar to raindrops. The clumps of plasma can penetrate between the magnetic field lines and can reach the surface of the neutron star without being threaded. As a result, the matter tends to land near the poles, but the impact area is relatively large (Shapiro & Teukolsky 1986). Threading can occur when the clumps of matter attach to the field lines within the magnetosphere (White et al. 1983). The presence of a strong magnetic field or instabilities near the polar cap can cause the matter to reach the surface in the form of elongated structures (resembling strings or spaghettis) or flattened structures (resembling pancakes). In addition, the matter tends to arrive primarily along certain sections or the outer perimeter of the field lines within the polar cap, rather than being uniformly distributed along all lines. If significant instabilities are present near the cap, the accretion column may become fragmented, possibly leading to a hollow-section funnel configuration. With fewer instabilities, the accretion column is more likely to be a filled funnel with a relatively uniform distribution of matter, see Figure 3.7 for an illustration of the different geometries (Basko & Sunyaev 1976; Mészáros 1984; Meszaros 1984; Kraus 2001).

As the matter follows the field lines toward the neutron star, there may be a cusp-like configuration of the magnetic field above the poles. The density and pressure of the matter increases as it approaches the cusp. Some of the matter will leak through, which means that the rate at which matter is channeled to the surface of the neutron star is regulated. This acts as a gateway, controlling the accretion rate and preventing immediate accretion of all incoming matter (Lamb et al. 1973; Arons & Lea 1976; Elsner & Lamb 1976).

When an accretion disk is present, matter spirals inward until it reaches the magnetospheric boundary. At larger distances, such as the inner accretion disk, the dominant magnetic field is the magnetic dipole field. The stellar magnetic field penetrates the inner accretion disk. This leads to the formation of a broad transition region. Within the boundary layer, the magnetic field undergoes minimal deformation, while at larger radii it becomes increasingly distorted. The magnetic field threads through the disk, and the plasma couples with the magnetic field lines and is guided by the magnetic field, resulting in a circular ring of matter falling at the magnetic poles (Ghosh & Lamb 1979a,b). The contact between the accretion disk and the magnetic field may also be uneven, changing the shape of the footprint. It could break up the matter flow into segments or cause a divergence from a spherically symmetric flow. This would have similar effects on the
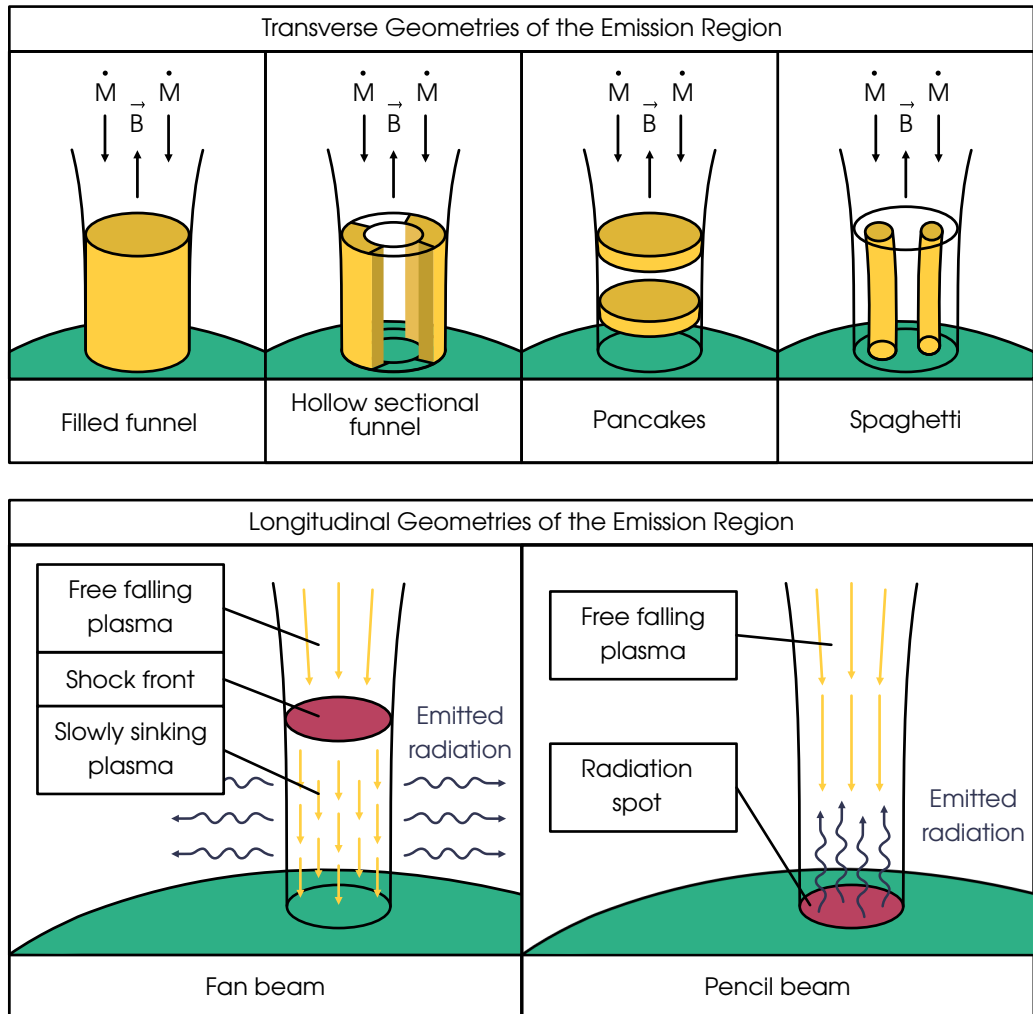
Figure 3.7: The configuration of the emission region depends on the transverse structure, perpendicular to the magnetic field, of the matter arriving at the surface of the neutron star. The upper part shows four such arrangements: a filled and a hollow funnel, as well as pancake and spaghetti-like formations. The longitudinal structure, parallel to the magnetic field, is commonly characterized as either a fan beam or a pencil beam, shown in the lower part. At high mass accretion rates, a shock forms above the surface of the neutron star, causing the plasma to gradually sink, with radiation being emitted laterally in a fan beam (left). In the absence of a shock, a hot spot is formed on the surface, and radiation is emitted radially upward in a pencil beam (right). These sketches, modified from Basko & Sunyaev (1976); Meszaros (1984), are not drawn to scale.

accretion funnel as the previously discussed instabilities. The size of the threading region might determine if the accretion column is a thin-walled hollow funnel, or a filled cylinder (see Figure 3.7). In a small threading region, compared to the size of the polar cap, the column is more likely to be uniformly filled. When it is larger, it might break up and follow specific channels or threads in the magnetic field, which causes the funnel to break up into a sections of a hollow funnel.

The shape and structure of the emission region near the surface of the neutron star is influenced by a number of factors, including the instabilities and threading regions mentioned above, as well as additional factors such as the strength of the magnetic field and the rate of accretion. This illustrates the complexity of the processes, which are not yet fully understood.

In both spherical and disk accretion, the multipole components of the magnetic field become more important near the surface, redirecting some of the accretion flux to regions other than the poles (Romanova et al. 2003; Long et al. 2007). Furthermore, any distortion or displacement of the dipole field axis will affect the location of the emission regions (Kraus et al. 1995, 1996). In addition, the presence of an accretion mound, which refers to a thin flat layer on the polar cap, can influence the magnetic field lines. As a result, the magnetic field lines will become distorted and no longer remain perpendicular to the surface. This change in the magnetic field configuration can have consequences for the accretion flow and the structure of the emission region (Mukherjee & Bhattacharya 2012).

It is therefore clear that the magnetic field plays a crucial role in the formation of the pulse profiles. The specific points where matter interacts with the neutron star surface depend on it, as do the shape and position of the footprints where the X-rays are generated (Lamb et al. 2009).

III. Vertical Emission Structure: The vertical or radial structure of the emission region above the surface of the neutron star is affected by the feedback of the emitted X-rays themselves, which in turn is affected by the accretion rate. When the accretion rate is low and the corresponding luminosity is below the critical luminosity (introduced in Equation 3.5), about 10^{36} to 10^{37} erg s^{-1}, the emission originates mainly from accretion hotspots on the surface of the neutron star. In such cases, X-rays are likely to be emitted in an upward direction, forming a narrow beam, called a pencil beam, aligned with the magnetic field lines (see Figure 3.7) (Basko & Sunyaev 1976; Mészáros 1984; Mushtukov & Tsygankov 2022). The shape of the hotspots does not need to be circular, as discussed above. Crescent- or ring-shaped emission regions are feasible as well and in some cases, such as when the magnetic obliquity is very small so that the emission region is close to the spin axis, they could also move on the surface instead of being stationary (Romanova et al. 2004; Lamb et al. 2009).

Above the critical luminosity threshold, when the accretion rate is high, the infalling matter undergoes deceleration and compression, resulting in the formation of a shock front.

This shock marks the beginning of the accretion column, and below it, the plasma slowly sinks towards the neutron star. In this regime, the emitted X-rays tend to be directed to the sides of the accretion column, propagating in a fan beam pattern. This fan beam, illustrated in Figure 3.7, is perpendicular to the magnetic field lines, indicating a broader emission distribution compared to the pencil beam emitted at lower accretion rates.

IV. Photon Modulation Factors: The X-rays emitted near the surface of a neutron star are affected and modulated by several phenomena in its immediate vicinity, including beaming, surface reflection, gravitational light bending, and scattering. Beaming is associated with anisotropic emission from the surface of the neutron star. X-rays emitted from the accretion column or hotspot are strongly beamed, resulting in concentrated emission along certain directions. For example, in the case of a pencil beam, this would be along the magnetic field lines. In addition to beaming, X-rays can be reflected off the surface of the neutron star after their initial emission from the hotspot or accretion column. This reflection process can cause phase shifts and intensity changes due to the interaction between the X-rays and the surface material. The strong gravitational field of the neutron star also affects the emitted X-rays, causing deflection and bending. The specific effects and their strength depend on the mass and compactness of the neutron star. Furthermore, X-rays can be scattered at different locations within the binary system, such as the accretion disk or the stellar wind of the companion star. This scattering process introduces time delays and energy-dependent phase shifts. These processes affect the intensity of the emitted X-rays visible to an observer and can change the perceived origin of the X-rays. For more information about these topics, see Riffert & Meszaros (1988); Kraus (2001); Poutanen & Beloborodov (2006); Becker & Wolff (2007); Ferrigno et al. (2009); Becker et al. (2012); Poutanen et al. (2013); Mushtukov & Tsygankov (2022).

Understanding the physical processes that shape the observed pulse profiles can be challenging. The configuration and strength of the magnetic field determine the geometry and physical conditions of the emission region, as well as the intrinsic beam pattern of the emitted radiation. In addition, the radiation produced by the XRP can interact with the accretion flow, which in turn depends on the rate at which matter is being accreted onto the compact object. This complex interplay adds another layer of complication to the already challenging task of modeling XRP emissions. However, there are two complementary approaches, namely modeling and observational methods, that attempt to do this. Modeling allows one to test various physical parameters and provides a theoretical framework for understanding the formation and shape of pulse profiles. On the other hand, the observational approach provides empirical data that can be compared with theoretical models, leading to improved modeling of the pulse profiles. In the following sections, these two approaches are discussed and specific examples are given.

3.2.2 Pulse Profile Modeling Techniques

Theoretical modeling of pulse profiles involves simulating the physical conditions and mechanisms that are responsible for their formation. The simulations typically involve factors such as the geometry of the accretion flow, magnetic field strength and structure, and properties of the neutron star atmosphere. Magnetohydrodynamic simulations for example take into account the interaction between the accreting matter and the magnetic field. This helps to understand the formation of accretion columns and how X-rays are emitted in them, see for example Mukherjee et al. (2014); Takahashi & Ohsuga (2017). Monte Carlo simulations can also be used to study the scattering of X-rays by the accretion disk or the stellar wind, and thus give insight into their effects on the pulse profiles. For this type of approach, see for example Mushtukov et al. (2021); Hou et al. (2022).

For an accurate model of XRP pulse profiles, the contributions of each emission region must be taken into account. This is typically done by creating a model that specifies the emission region geometry, the number of emission regions, and the shape of the local beam pattern. The emission is then integrated over all viewing angles for a given phase and over all visible emission regions (or parts thereof). The emission region geometry can be a hotspot, a slab, or an accretion column. A hotspot is a small localized region that emits X-rays, while a slab is a flat region of accreted material that can be self-emitting or externally illuminated. The accretion column can also have different shapes, as discussed above.

In addition to the geometry of the emission region, in some cases an isotropic beam pattern can be assumed, while in others the beam pattern may be a pencil or fan beam shape, or a mixture. Furthermore, relativistic effects can play a significant role in determining the observed pulse profiles. It is therefore important to take these effects into account when modeling XRP pulse profiles. This is typically done by using ray tracing techniques that account for the effects of general relativity on the initial emission of the intrinsic beam pattern.

In addition to the beam pattern and relativistic effects, other parameters such as the size of the polar cap, the magnetic field, and the location of the emission regions on the surface of the neutron star must be considered. These parameters can vary between models and can affect the resulting pulse profiles, as well as the orientation of the observer. Each XRP model has its own set of assumptions, parameters, and advantages and disadvantages. More concrete, some theoretical models that have been proposed to interpret observed pulse profiles can be found in Wang & Welter (1981); Meszaros & Nagel (1985); Kraus et al. (1995); Ferrigno et al. (2011); Cappallo et al. (2017); Iwakiri et al. (2019); Caiazzo & Heyl (2021) (and references therein), to name a few. As an example, Figure 3.8 shows how the model from Cappallo et al. (2017) accounts for beam patterns and relativistic light bending. However, this approach of theoretical modeling relies on the adequacy of the underlying assumptions and assumed values of the various parameters, such as the beam
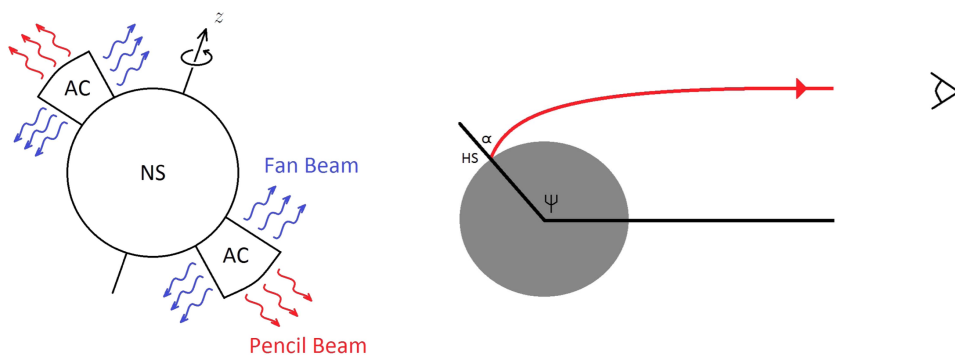
Figure 3.8: The model of Cappallo et al. (2017) considers fan and pencil beams originating from the sides and top of the two accretion columns (left). The axis of rotation is along the z-axis, and the magnetic dipole axis passes through the accretion columns. The geometry of the light-bending approximation of Beloborodov (2002) is shown on the right. The figures are taken from Cappallo et al. (2017).

pattern, which is difficult to test.

3.2.3 State-of-the-Art Approaches to Profile Decomposition

An alternative to modeling is the observational approach. By using additional information from observations, elements of the pulse profile formation factors discussed in Section 3.2.1 can be inferred. As an example, the transition through the critical luminosity ($L_X \approx 10^{37}$ erg s^{-1}, see also Equation 3.5) can also be analyzed in the pulse profile shape and is associated with a transition of accretion disk state and with the onset of an accretion column. This implies changes in the intrinsic beam pattern that affect the shape of the pulse profile. Studies that have taken this approach include Doroshenko et al. (2020); Tuo et al. (2020); Wang et al. (2022); Kong et al. (2022).

The pulse profiles for a large number of XRPs show little variation with energy at low X-ray luminosities, but there is a significant energy dependence at higher luminosities, above about 5×10^{36} erg s^{-1}. This observation is seen as evidence for the accretion column formation (Basko & Sunyaev 1976), and under this assumption, more information can be inferred. For example, the orientation angle of the magnetic axis can be determined, and the inclination of the magnetic axis is likely small (Karino 2007). Therefore, such observational analyses can help to understand the formation of pulse profiles by providing a better understanding to the emission regions.

One piece of information that is still unclear, but essential to understanding the geometry of the emission regions and the physical processes involved, is knowing the contributions of the individual emission regions to the total pulse profiles. As seen in Section 3.2.1 this

is a challenging task as the emission from both poles may occur at the same pulse phase. Beam patterns, column geometries, gravitational light bending and beaming of X-ray are some of the causes for this complication (Mushtukov & Tsygankov 2022).

Decomposition Approach: Prompted by the observation that most XRPs have asymmetric pulse profiles, Kraus et al. (1995) proposed a method to analyze the profiles and decompose them into the contributions of two emission regions. The basis of the method is the assumption that the observed asymmetry is a consequence of a distorted magnetic dipole field, causing the axis connecting the two poles to deviate from the center of the neutron star. This distortion implies that the magnetic poles are not antipodal, but shifted with respect to each other and this causes asymmetry even when assuming symmetric beam patterns. The contributions that can then be disentangled, make it possible to determine the locations of the magnetic poles and reconstruct the beam pattern that is visible to an observer. This method has been applied to several sources, such as Cen X−3 (Kraus et al. 1996), Her X−1 (Blum & Kraus 2000), EXO 2030+375 (Sasaki et al. 2010), 1A 0535+262 (Caballero et al. 2011), 4U 0115+63 and V 0332+53 (Sasaki et al. 2012), and with it, the geometry and intrinsic beam patterns were reconstructed.

Recently, Hu et al. (2023) performed a broadband analysis of Insight HXMT data during a giant outburst in 2020 to revisit the source 1A 0535+262. They decomposed the pulse profiles of the source using the method proposed by Kraus et al. (1995). It is important to note that there are multiple solutions for any choice of symmetry points. However, the solutions must meet certain selection criteria in order to be considered. First, the solutions must be non-negative, since the profiles represent counts or count rates. Second, the "no ripples" criterion ensures that there are no small scale features that cancel out in the sum. In addition, the two single-pole pulse profiles should not be more complex than the observed total profile. Finally, the choice of symmetry points should be consistent for all pulse profiles at different energies. Note that the set of selection criteria used in the method may lead to incorrect results, which is a potential limitation. An illustration of an application of the method is presented in Figure 3.9, which shows the pulse profile decomposition of 1A 0535+262 in the 15-30 keV energy range that meets the specified criteria. Once an acceptable decomposition is found, the beam pattern as seen by a distant observer can be calculated. The angle θ_{obs} between the line of sight and the axis passing through the magnetic pole changes with the rotation of the neutron star. Since there is no way to determine which symmetry points correspond to the closest or furthest point from the line of sight, both solutions are presented in Figure 3.9. Finally, to compute the intrinsic beam pattern, relativistic effects must be taken into account, specifically the local direction of the photon emission relative to the distant propagation from the neutron star. Given standard values for the neutron star's mass and radius, the intrinsic beam pattern can be computed for each of the solutions shown in the bottom panel of Figure 3.9. The

θ_{obs}^- solution shows strong intensity in the 90° direction, indicating a possible fan emission. The detailed analysis of 1A 0535+262 is published in Hu et al. (2023).

Limitations and Challenges of the Method: The method introduced by Kraus et al. (1995) is based on two fundamental assumptions: the emission originates from the two magnetic poles of the neutron star, and the emission characteristics are identical with an axisymmetric beam pattern. These assumptions allow the decomposition of the pulse profile into two symmetrical single-pole pulse profiles. However, the assumption of an axisymmetric beam pattern is not necessarily always valid. According to Kaminker et al. (1983) and Burnard et al. (1988), this assumption only holds when the magnetic field is perpendicular to the surface of the neutron star. If the angle between them is less than 90 degrees, the intrinsic beam pattern can be significantly asymmetric (see Figure 1c in Kaminker et al. 1983).

There are several reasons why the magnetic field at the magnetic pole may not be perpendicular to the surface of the neutron star (see also Figure 3.10). For example, the circular dipole magnetic field lines, which have a cosine relationship, imply that there is an angle between the surface normal and the magnetic field at the radius of the neutron star. In addition, although the dipole magnetic field dominates at larger distances, the surface magnetic field may be dominated by higher multipole components, which means that the field angle may not be perpendicular to the surface. Another possibility is that an extended accretion mound could cause the magnetic field lines to bend to support the pressure of the matter confined within it, causing a distortion of the magnetic field relative to the plasma at the surface of the neutron star (Mukherjee & Bhattacharya 2012). It is therefore difficult to argue that the magnetic field lines must be perpendicular to the plasma, and this can lead to a non-axisymmetric beam pattern, which poses a challenge to the method proposed by Kraus et al. (1995).
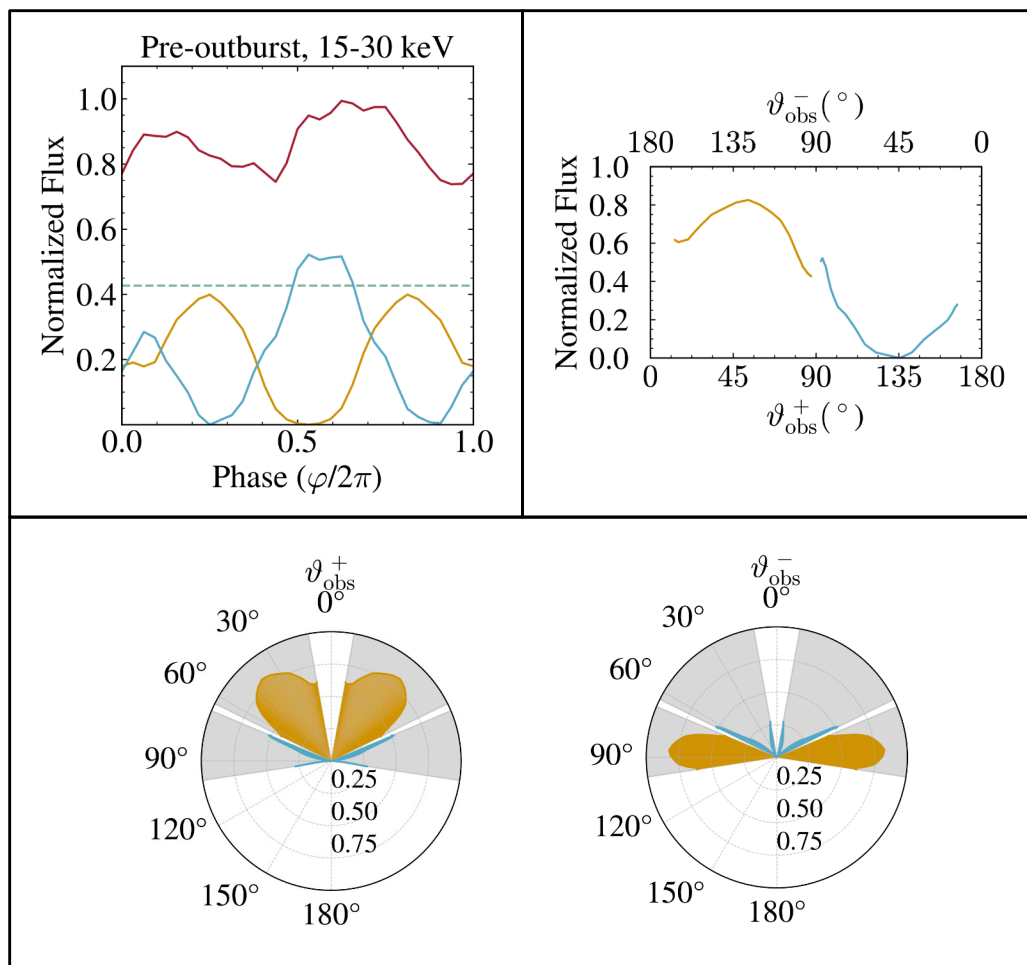
Figure 3.9: Top left: Decomposition of the pulse profile (red line) of 1A 0535+262 in the 15-30 keV energy range before its giant outburst in 2020 into two single-pole pulse profiles (yellow and blue) according to the method of Kraus et al. (1995), together with a constant baseline (green dashed line). Top right: The inferred beam pattern from the single-pole pulse profiles. The two x-axes show the two possible solutions from the ambiguity of the symmetry points. Bottom: Intrinsic beam patterns for the two solutions. The colors indicate the results from the two emission regions, where the upward direction (0°) is straight up from the magnetic pole and 90° is tangential to the neutron star surface at the pole. The radius represents the intensity. The white areas have no information. I created the figures shown here to illustrate the working principle of the outlined decomposition method of Kraus et al. (1995). Detailed results are published in Hu et al. (2023).
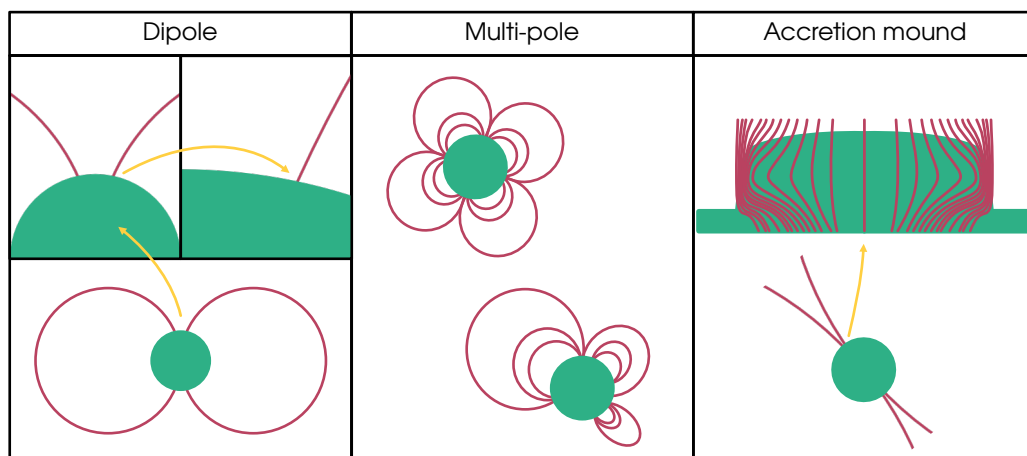
Figure 3.10: There are several possible explanations for why the magnetic field of a neutron star may not be perpendicular to its surface at the magnetic pole. The figures provided are not to scale and are greatly exaggerated for illustrative purposes. The first figure shows the magnetic field lines of an idealized dipole with circular field lines. However, at the surface of the neutron star the field lines will not be perpendicular to the surface. The second image shows more complex and higher multipole configurations of the magnetic field. Finally, the third image shows the accretion mound at the magnetic pole, which may cause the field lines to bend in order to support the pressure of the accreted matter (Mukherjee & Bhattacharya 2012).

4. X-ray Satellites & Instruments

X-rays are absorbed by the Earth's atmosphere, so X-ray telescopes must be placed in space. This imposes several constraints on observatories, including size, weight, and cost. There is often a trade-off between the best angular resolution and the largest possible collecting area. While good angular resolution is beneficial for many purposes, certain applications may benefit from a non-imaging instrument with a large collecting area (Arnaud et al. 2011, p. 6). Proportional counters are an example of an instrument that can be used without focusing optics. By using a collimator, the field of view can be limited to individual sources. The Uhuru satellite (Giacconi et al. 1971b) and the proportional counter array on the Rossi X-ray Timing Explorer (RXTE) satellite, which have been used to time X-ray pulsars (XRPs), are examples of this concept in use (Arnaud et al. 2011, p. 24).

The following Section 4.1 presents an overview and comparison of a selected group of X-ray satellites, including their time resolutions and geometric areas. In addition, a brief discussion of the selection of a telescope for research purposes, specifically tailored to this thesis, will be included. Following this, Section 4.2 provides an overview of the RXTE payload, with particular emphasis on the Proportional Counter Array (PCA).

4.1 Overview and Comparison of X-ray Satellites

In this thesis, pulse profiles are studied by exploiting pulse-to-pulse variability. This requires high quality phase-resolved light curves. The choice of telescope for this study is limited by the requirement for a large effective area to ensure sufficient counts in each phase bin. As a result, only X-ray telescopes with geometric areas larger than $5000\,\mathrm{cm}^2$ were selected for the following comparison. This limits the choice of different X-ray telescopes and narrows the options to the

- High Energy Telescope (HE, Liu et al. 2020) on the Hard X-ray Modulation Telescope (HXMT, Li 2007; Zhang et al. 2020), named "Insight", the
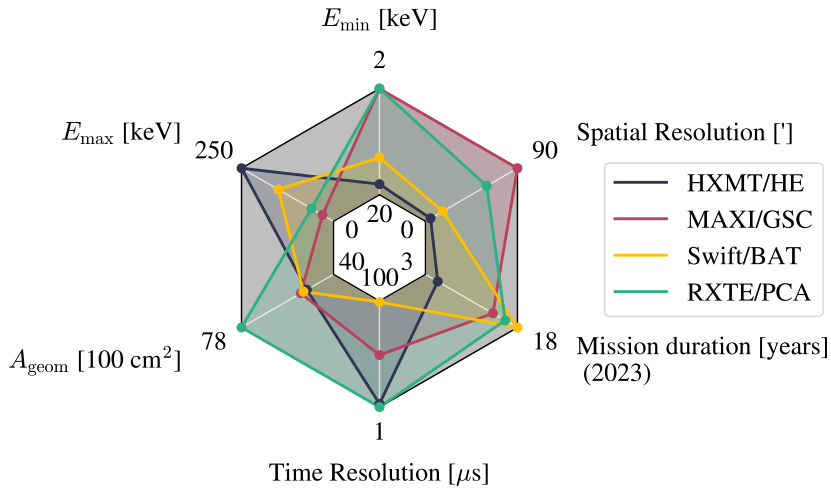
Figure 4.1: The spider diagram shows some of the main characteristics of a few satellites and instruments. These instruments were selected because they have effective areas greater than $5000\,\text{cm}^2$. Note that each axis is scaled so that the outermost value represents the preferred property. That is, lower energy and time resolutions are generally preferred, so the axes are inverted. Table 4.1 lists the sources of the data shown in the figure.

- Gas Slit Camera (GSC, Mihara et al. 2011) on the Monitor of All-sky X-ray Image (MAXI, Matsuoka et al. 2009) experiment, which is located at the International Space Station (ISS), the
- Burst Alert Telescope (BAT, Barthelmy et al. 2005) on the Neil Gehrels Swift Observatory Gehrels et al. 2004, and the
- Proportional Counter Array (PCA, Glasser et al. 1994) as part of the Rossi X-ray Timing Explorer (RXTE, Bradt et al. 1993).

An overview comparison of various characteristics relevant to this thesis is shown in Figure 4.1 and the values and references are given in Table 4.1. Note that the instruments and detector principles differ greatly between the satellites, so the numbers should only be used as rough approximations for comparison purposes.

In the following, the effective areas as well as the time resolution of the telescopes will be discussed in more detail.

4.1.1 Effective Areas of X-ray Instruments

The effective area (A_{eff}) of an instrument is given by the product of the efficiency and the geometric collecting area (A_{geom}) (Aschenbach 1985, p. 609).

The geometric collecting area depends on the type of telescope and instrument used.

Table 4.1: Some of the main characteristics of a few satellites and instruments with geometric areas greater than $5000\,\mathrm{cm}^2$. A visual comparison of the data is shown in Figure 4.1.

	RXTE/PCA		MAXI/GSC		Swift/BAT		HXMT/HE	
	Value†	Ref.	Value	Ref.	Value	Ref.	Value	Ref.
Launch [year]	1995†	[1]	2009	[5]	2004	[7]	2017	[11][12][13]
$E_{\min}$ [keV]	2	[1][2][3]	2	[5]	15	[8][9]	20	[11][12][14]
$E_{\max}$ [keV]	20	[1][2][3]	30	[5]	150	[8][9]	250	[11][12][14]
A_{geom} [cm^2]	7800	[4]	5350	[5]	5240	[8]	5100	[11][13][14]
Time Resolution [μs]	1	[2][3]	50	[5]	100	[10]	2	[12][14]
Spatial Resolution [']	60	[2]	90	[6]	17	[9]	< 5	[13][15]

Note. †Deactivated in 2012.
References.
RXTE/PCA: [1] Jahoda et al. (1996), [2] Zhang et al. (1993), [3] Glasser et al. (1994), [4] Jahoda et al. (2006).
MAXI/GSC: [5] Mihara et al. (2011), [6] Sugizaki et al. (2011).
Swift/BAT: [7] Romano et al. (2005), [8] Gehrels et al. (2004), [9] Barthelmy et al. (2005), [10] Sun et al. (2019).
HXMT/HE: [11] Zhang et al. (2020), [12] Li et al. (2020), [13] Nang et al. (2020), [14] Li et al. (2019), [15] Li (2007).

In a Wolter Type I configuration (Wolter 1952a,b), the collecting area is the projection of the primary surface onto the entrance aperture, while the efficiency is the average of the reflectivities of the mirrors (primary and secondary in a two-mirror system) over all incidence angles. Reflectivity is wavelength dependent, so efficiency and effective area are also wavelength dependent. (Aschenbach 1985, p. 609). In addition to reflectivity, the effective area takes into account all other losses of photons entering the telescope, such as the quantum efficiency of the detector and losses in the optical system (Longair 2011, p. 775).

Collimating instruments, such as RXTE's PCA, have a geometric collecting area corresponding to the area exposed to X-rays. Therefore, collimating instruments generally have larger effective areas than focusing X-ray telescopes. RXTE/PCA has the largest geometric area of about $7800\,cm^2$ (effective area of about $6500\,cm^2$), followed by HXMT/HE, MAXI/GSC, and Swift/BAT, which all have areas ranging from $5000\,cm^2$ to $5400\,cm^2$, as listed Table 4.1.

4.1.2 Time Resolution of X-ray Observatories

To study the properties, changes, and dynamics of XRPs, adequate time resolution is essential. The time resolution of an X-ray satellite depends on a number of factors, including its design, acquisition speed, signal processing capabilities, and other technical features.

Because X-ray sources exhibit variability over a wide range of timescales, each observation can be a time measurement because it can be compared to earlier or later measurements. That being said, the timescales of interest (see also Section 3.1.4) range from the free-fall time of accreted matter (on the order of 100 microseconds), to spin periods (from 0.1 to 1000 seconds), to orbital periods (from 10^3 seconds to 10^2 days), or even to superorbital periods that can span multiple orbital periods. While all X-ray missions can be used for timing, the detection of the lower end of the timescales often requires specialized instruments (Bradt & Swank 1989).

Among current and past instruments, RXTE/PCA stands out for its exceptional time resolution of about 1 microsecond. This makes it a valuable tool for studying the pulse profiles of XRPs, as well as for measuring other fast X-ray variability. However, the high time resolution of RXTE/PCA comes at the expense of lower sensitivity and spectral resolution, limiting its usefulness for certain other types of research (e.g. faint sources). Each instrument is designed with different trade-offs between time resolution and other observational capabilities. Future developments will further improve our ability to study and understand XRPs and their properties and physical processes on small timescales.

4.1.3 Selecting a Telescope for a Study

There are several parameters to consider when selecting a telescope for a particular study. For example, for spectral analysis, energy range and resolution are important. In addition, when analyzing the evolution of spectral parameters over time, e.g. during an orbit, each spectrum in a given time interval should have sufficient counts to support a meaningful analysis. When studying pulse profiles, the energy range is also an important consideration. The pulse profiles may vary with energy, requiring a wide energy range to follow the changes. Alternatively, if a stable pulse profile is desired, the energy band should be chosen accordingly. In addition, the possible exposure time for a source is another important factor. Since MAXI is on the ISS, it scans the sky about every 92 minutes and can observe each source for only 40-150 seconds (Sugizaki et al. 2011; Torregrosa et al. 2022). If longer observations are needed, stacking observations in time could be a solution depending on the purpose, but for continuous observations another telescope should be chosen. It should be noted that other parameters may also be essential for selecting the appropriate telescope for a particular study. This work uses the RXTE/PCA instrument. Some of the notable features of PCA are its large effective area of $6500\,\mathrm{cm}^2$, its time resolution of $1\,\mu$s, and its extensive observation of multiple X-ray sources over 16 years with long exposure times. For example, it observed Cen X$-$3 for 119,968 seconds (about 33 hours) in one observation. The following section provides a more detailed introduction to RXTE, including descriptions of the payload and PCA.

4.2 The Rossi X-ray Timing Explorer (RXTE)

The Rossi X-ray Timing Explorer (RXTE) was a NASA satellite that operated from December 30, 1996 until January 12, 2012, when it was deactivated. The satellite was named in honor of Bruno Benedetto Rossi. Rossi was a physicist and astrophysicist who was born in Venice, Italy, on April 13, 1905, and died in the United States on November 21, 1993. He was involved in early rocket-borne detectors searching for extrasolar X-ray sources. In 1928, Rossi invented an electronic coincidence circuit capable of recording signals with a time resolution better than 1 millisecond. Feeling the dangers of the Fascist state, Rossi left Italy in 1938 and settled in the U.S. after visiting Denmark and England. In 1943, he participated in the development of the atomic bomb before being appointed professor of physics at the Massachusetts Institute of Technology in 1946. Rossi and his group studied cosmic rays and air showers with primary cosmic ray energies up to 10^{20} eV. Rossi was also interested in carrying detectors above the atmosphere to investigate the possibility of extrasolar X-ray sources. An experiment developed under Riccardo Giacconi and launched in 1962 discovered the first extrasolar X-ray source, Sco X$-$1, and an unresolved X-ray background. Throughout his life, Rossi remained active in the fields of space physics and X-ray astronomy, receiving numerous honorary doctorates and awards. The RXTE satellite was named in honor of his work. The satellite was originally named

the X-ray Timing Explorer (XTE) at launch, before being renamed the Rossi X-ray Timing Explorer (RXTE). The satellite's mission was to study X-ray sources such as black holes and neutron stars by making precise timing measurements of their X-ray emissions. It was decommissioned in 2012 after 16 years of successful operation and re-entered Earth's atmosphere on April 30, 2018 (Hockey et al. 2007, pp. 985 f.).

The primary scientific goal of RXTE was to study the nature, environments, and evolution of galactic and extragalactic compact objects and systems by analyzing the temporal evolution of radiation in the 2-200 keV X-ray bandpass. Objects of interest included white dwarfs, neutron stars, stellar black hole candidates, and active galactic nuclei containing massive black holes (Bradt 1997).

To accomplish these scientific goals, RXTE had a payload consisting of three instruments, see Figure 4.2. In the following section, the All-Sky Monitor (ASM) and the High Energy X-ray Timing Experiment (HEXTE) will be discussed. A more detailed description of the Proportional Counter Array (PCA) is given in Section 4.2.2.

4.2.1 Payload Description

All-Sky Monitor (ASM) The ASM is made of 3 Scanning Shadow Cameras (SSC) that are located on a rotating boom. The total net effective is $180 \, cm^2$ without, and $90 \, cm^2$ with masks. The field of view of a single camera is $6° \times 90°$ (FWHM) with an angular resolution of 0.2°. The SSC detectors are proportional counters that are filled with xenon-CO_2. It is sensitive to X-rays of 2-10 keV in three energy channels. The ASM rotates in increments of 6°, taking 100 second exposures at each step. A complete rotation therefore takes about 100 minutes (Bradt et al. 1993; Bradt 1997).

High Energy X-ray Timing Experiment (HEXTE) HEXTE covers the energy range 20 to 200 keV with 8 phoswich detectors. The detectors are divided into two clusters and each detectors has an effective area of about $200 \, cm^2$. Thus, the total net area is about $1600 \, cm^2$, with a field of view of about 1° FWHM. HEXTE is coaligned with PCA. The clusters of detectors are rotated on and off the observed source about every 15 seconds, which allows for the source and background to be measured alternating, but the timing of the rotation is such that one cluster is always on target. See Figure 4.3 for a sketch of HEXTE (Bradt et al. 1993; Bradt 1997).

4.2.2 The Proportional Counter Array (PCA)

The PCA consists of five proportional counter units (PCUs) with a total effective area of approximately $6250 \, cm^2$. These PCUs are designed to give stable, low background performance. The cross section of a PCU can be seen in Figure 4.4. At the top of each unit is a collimator composed of five rectangular modules containing hexagonal cells about 0.3 cm across. The collimator limits the field of view to 1°. Beneath the collimator, two Mylar
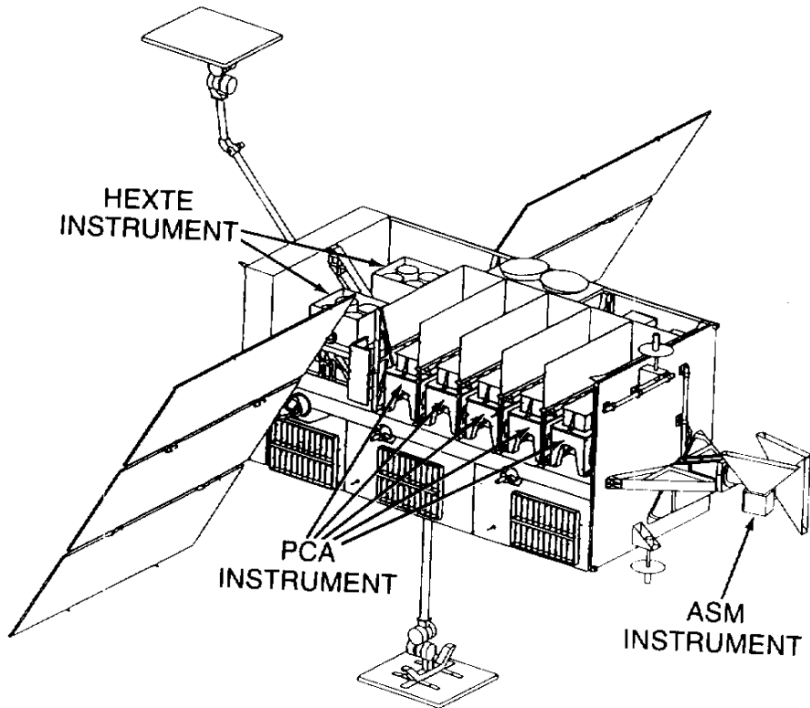
Figure 4.2: The payload of the RXTE satellite is shown, including the HEXTE instrument consisting of two clusters each with four phoswich detectors, the five instruments of the PCA, and the ASM. Also shown are the solar panels, antennas (located at the top, bottom, and near the ASM), and star tackers (visible as circular objects located behind the PCA). This image is from Glasser et al. (1994).
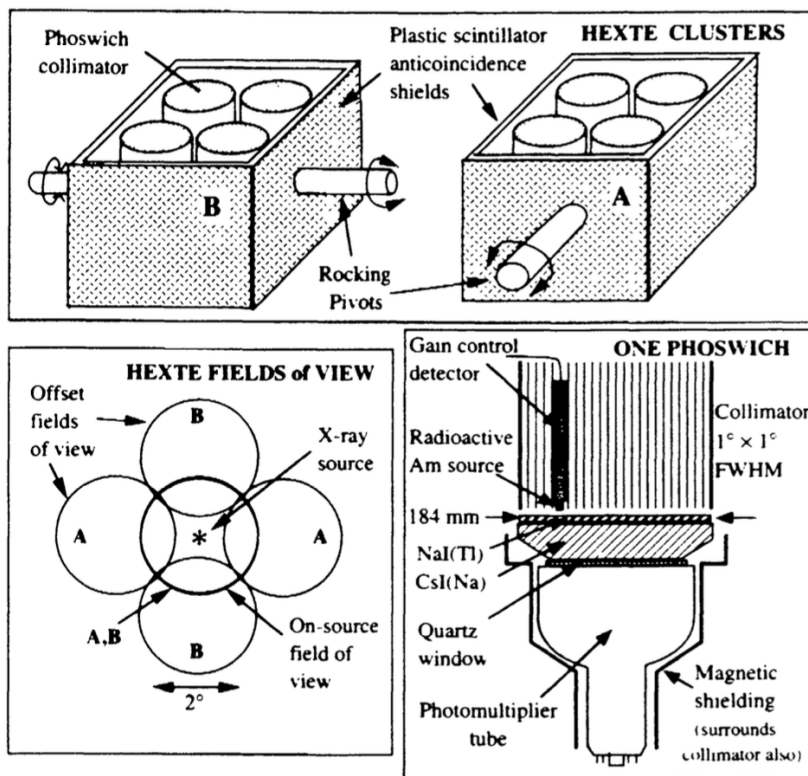
Figure 4.3: The HEXTE instrument onboard RXTE consists of eight phoswich detectors, the cross section of one phoswich is shown in the lower right panel of the figure. The top panel shows two clusters, each containing four of the phoswich detectors. The clusters are orthogonal to each other and are rotated to ensure that the source is always within the field of view. Four background regions are measured, as shown in the lower left. This image is taken from Bradt et al. (1993).

windows are the boundaries of a 1.3 cm deep propane volume that is used as an electron veto region and a front anti-coincidence shield. The main component of the detectors is a chamber containing a xenon gas with about 10% methane. The chamber is surrounded by a wire mesh. When an X-ray photon enters the chamber, it ionizes a gas atom. The wire mesh is held at a high voltage, which accelerates the free electrons toward it. As the electrons pass through the wire mesh, they cause additional ionization, creating a cascade of electrons that produce a measurable electrical signal.
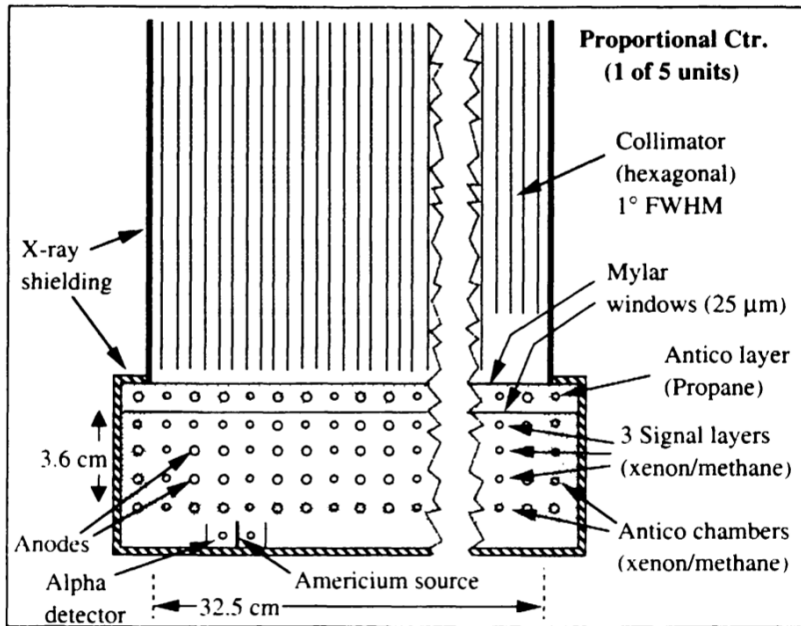
Figure 4.4: Cross-section of an RXTE/PCA unit. Each unit consists of three detector layers filled with xenon/methane and surrounded by an anticoincidence chamber. In addition, there is an anticoincidence layer of propane above the detector layers surrounded by Mylar windows. A collimator limits the field of view of each unit to 1° FWHM. This image is from Bradt et al. (1993).

The PCA detector on RXTE has a sensitivity of 2-60 keV with an energy resolution of 18% at 6 keV and 255 energy channels. It also has microsecond timing capabilities and a field of view of 1° FWHM. The data is binned and analyzed on board by the Experiment Data System (EDS). The EDS is capable of timing photon arrivals to about 1 microsecond and consists of six independent Event Analyzers (EAs). Each of the EAs can analyze the PCA data in parallel and includes a digital signal processor (DSP) chip that bins the events according to different criteria, such as good energy resolution and coarse time resolution, that can be specified for each observation. The DSP uses a table lookup scheme

to achieve the required speed. Two of the EAs are reserved for standard modes, which include consistent timing and standard parameters for a mission database. The time series mode has a 0.1 second binning and 6 energy channels, while the spectral mode has a 16 second binning and 128 energy channels. Two additional EAs process the All Sky Monitor (ASM) data and control its rotation. Finally, the EAs generate data packets for transmission to the ground (Bradt et al. 1993; Zhang et al. 1993; Arnaud et al. 2011).
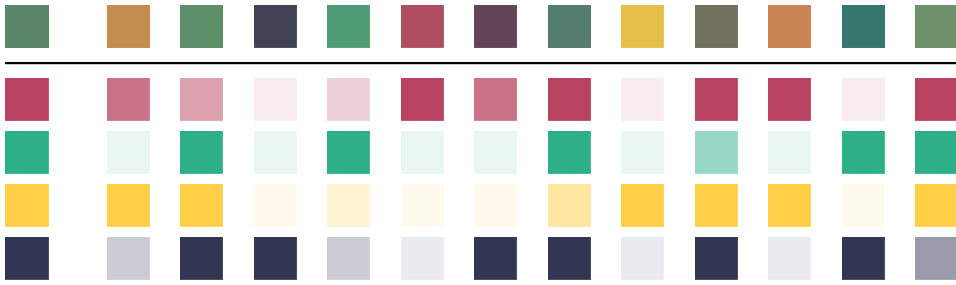
Method Development

5. Blind Source Separation

In Chapter 3 I introduced X-ray pulsars (XRPs) and explored their various observables and properties. In Section 3.2 I focused on the challenges of understanding their pulse profiles in detail. One of the main difficulties in this context is understanding the complex emission regions and beam patterns corresponding to the two neutron star poles involved. In addition, determining the individual contributions of the two emission regions to the overall pulse profile is a difficult problem. If the emission originates primarily from the two magnetic poles, various factors such as geometry, beam pattern, gravitational light bending, and other effects may be responsible for the simultaneous visibility of emission from both poles during some phases of the pulse. Disentangling these contributions is the first step towards understanding the pulse profile formation and testing theoretical models of the emission.

In this chapter I describe the approach to this problem based on the analysis of the observed stochastic variability in XRPs. The observed fluctuations in the X-ray flux trace the mass accretion rate to the surface of the neutron star. By studying the correlation properties, it may be possible to separate the flux coming from the individual poles of the neutron star. In essence, this approach allows the extraction of two distinct signals: the flux from each pole as it varies throughout the pulse phase. This problem can be formulated in terms of a technique known as blind source separation (BSS). The detailed explanation of why such separable signals are expected to exist in XRPs will be discussed in Chapter 6, along with the details of how this can be put into the context of BSS. But first, the basic concept of classical BSS is introduced below.

The classic "cocktail party" provides a popular analogy for this problem. In this scenario, a guest is at a party with multiple conversations and various background noises. In the midst of this chaos, the guest tries to focus on a particular conversation while filtering out the surrounding noise. Although the human brain is capable of this selective listening, it remains a challenging task for machines. The following is an outline of the

basic framework of such a problem.

Consider a scenario where there are multiple source signals, denoted as s, which can be represented as a vector:

$$s(t) = [s_1(t), s_2(t), \ldots, s_m(t)]^\mathsf{T},$$

where T is the transposition.

To better understand this, let's imagine a lively cocktail party with two speakers at different locations. In this case, we have $m = 2$ source signals, namely $s_1(t)$ and $s_2(t)$. The party venue is equipped with several (n) microphones placed around the room. These microphones capture the ambient sounds, and the resulting observed signals can be represented as another vector, x:

$$x(t) = [x_1(t), x_2(t), \ldots, x_n(t)]^\mathsf{T}.$$

For example, if we have five microphones, we would have five data sets of signals, namely $x_1(t), x_2(t), \ldots, x_5(t)$. Mathematically, these observed signals are a mixture of the two source signals, i.e., the sounds from the speakers in the party room, influenced by a mixing operator $A = [a_{ij}] \in \mathbb{R}^{n \times m}$ in addition to other background noise. The mixing operator, represented by the matrix A, contains the mixing coefficients that determine the contributions of each source signal to the observed signals captured by the microphones. Each microphone captures the source signals with different intensities, which are precisely defined by these coefficients. In essence, the observed signal vector x is given by the multiplication $x = As(t)$.

It is not possible to disentangle or separate two signals with less than two observations. In other words, having at least two microphones are required to accurately recover the source signals. Both the source signals $s(t)$ and the mixing operator A are unknown. This is the problem that BSS addresses. The goal of BSS is to recover the source signals and thus determine the mixing operator by finding a matrix $B = [b_{ij}] \in \mathbb{R}^{n \times m}$. This matrix allows us to approximate the original source signals. By applying this matrix to the observed signals, denoted as $y = Bx(t)$, we can obtain an estimate of the source signals:

$$y(t) = [y_1(t), y_2(t), \ldots, y_m(t)]^\mathsf{T}.$$

In the context of our cocktail party, the speakers $s_{1,2}$ correspond to the estimated source signals $y_{1,2}$. In general, BSS is an underdetermined problem, and any method used to solve it requires certain assumptions or constraints. However, a common assumption of all BSS methods is that the signals are to some extent independent, and the desired solution for the source signals and mixing operator corresponds to maximally independent signals.

5.1 Applications of Blind Source Separation

BSS is a well-established technique used in many areas. Three of them are presented below for illustration: communication systems, medical signal analysis, and astrophysical applications.

5.1.1 Communication Signal Processing

A communication system serves the purpose of transmitting, exchanging, and receiving information from a source to a receiver, typically located at a considerable distance. This information can be of various types, such as images, sounds, or other forms of data. For the communication system to work, the information must first be converted into a signal, a task performed by the transmitter. The signal then travels through a medium, which can be a wire, cable, or a wireless channel such as air. At the receiving end, the signal is picked up and decoded by the receiver. To ensure compatibility and understanding between the transmitter and receiver, most communication systems have specific protocols and standards that must be followed. One of the earliest significant advances in telecommunications was Samuel F. B. Morse's work on telegraphy around 1844. Morse used signals of varying durations, dots and dashes, to encode text that was then transmitted. Following the work on telegraphy, telephony was developed, and some notable mentions in the further development of communication systems are Alexander Graham Bell's invention of the telephone system in 1876, G. Marconi's wireless telegraph system in 1897, developments in television in the 1920s, and J. Pierce's contributions to satellite communication systems in the 1950s (Wright & Reynders 2004; Crilly & Carlson 2009). Some examples of wired communication systems include landline telephony using the Public Switched Telephone Network (PSTN), which is still in use today, although its use has declined, Ethernet networks, and cable television systems. For wireless communications, notable examples include cellular networks, Wi-Fi technology, satellite communications, and radio communications. The ability of terrestrial television viewers to watch astronauts working in space is an impressive and fascinating example of communication systems at work (Chan 2013).

In an ideal scenario, the signal received at the end of a communications system should match the original input signal. However, there are numerous factors that degrade signal quality, including attenuation, crosstalk, noise, and other influences. As a result, the power of the signal tends to decrease with distance. Attenuation refers to the phenomenon where signals experience degradation when transmitted through any medium over a given distance. For example, in the case of PSTN, the copper cables used introduce resistance that contributes to attenuation. As a result, some of the energy from the signal transmission may be converted to heat, leading to a continuous decrease in signal amplitude, see Figure 5.1 for a sketch. In addition, the presence of physically adjacent cables or circuits can contribute to crosstalk, which is the interference caused by their proximity. Shielding

techniques can help reduce crosstalk. Another important factor that can negatively affect signal quality is noise. As the signal propagates, the molecules within the transmission medium can vibrate and emit electromagnetic signals, which can be considered a form of noise. The problem arises when the signal strength is insufficient, causing the signal to become indistinguishable from the surrounding noise. As a result, the receiver may have difficulty isolating the intended signal from the noise, leading to communication errors. More generally, noise can be broadly defined as random or unpredictable signals generated by natural processes, both internal and external to the system. See Figure 5.1 for a visual sketch of noise affecting a signal (Wright & Reynders 2004; Crilly & Carlson 2009).
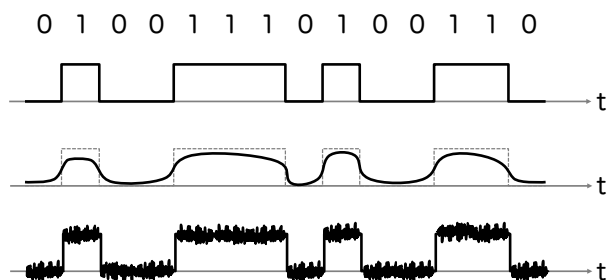
Figure 5.1: Visualization of potential contamination of a signal as it travels from a transmitter (left end) to a receiver (right end). The top row shows the original signal and its sequence. The effect of attenuation on the signal is shown below. This effect becomes more significant as the distance increases. The bottom row shows the effect of noise on the signal.

A common example of noise is wind noise. It can pose a significant challenge when attempting to understand voice signals contaminated by wind noise in situations such as cell phone conversations, video recordings, or hearing aids. Since it is not feasible to install physical wind filters in most cases, digital signal processing techniques are required to address this issue. In addition to its role in communications signal processing, digital signal processing (DSP) plays an important role in understanding various phenomena. With millions of sensors around the world and an abundance of elements to track and analyze, DSP contributes to numerous applications. For example, the electrocardiogram (ECG) provides insight into the condition of our hearts and will be explored in a later section focusing on medical signals. Another example is the use of fingerprints for personal identification, which highlights the importance of signal separation and extraction for efficient communication (Nelke et al. 2016; Zieliński 2021).

BSS Techniques in Telecommunications: To improve the quality of telecommunications signals, the effects of interference and crosstalk should be reduced. These factors can significantly degrade the signal and its clarity. One approach to this challenge is the

use of BSS, which allows mixed signals to be recovered with minimal prior knowledge. Electronic implementations of BSS have been widely used, but have certain limitations. These include narrow bandwidths and the high power consumption associated with digital signal processors (DSPs), which limits their overall versatility. A study conducted by Zhang et al. (2023) investigated a photonic BSS approach. The use of a photonic chip resulted in a significant increase in bandwidth, enabling processing capabilities of around 19 GHz while maintaining good energy efficiency. This photonic BSS system showed promising results in signal mixing and recovery, as shown in Figure 5.2. It is clear that BSS combined with a photonic implementation can reduce interference and crosstalk in telecommunications, thereby improving signal quality.
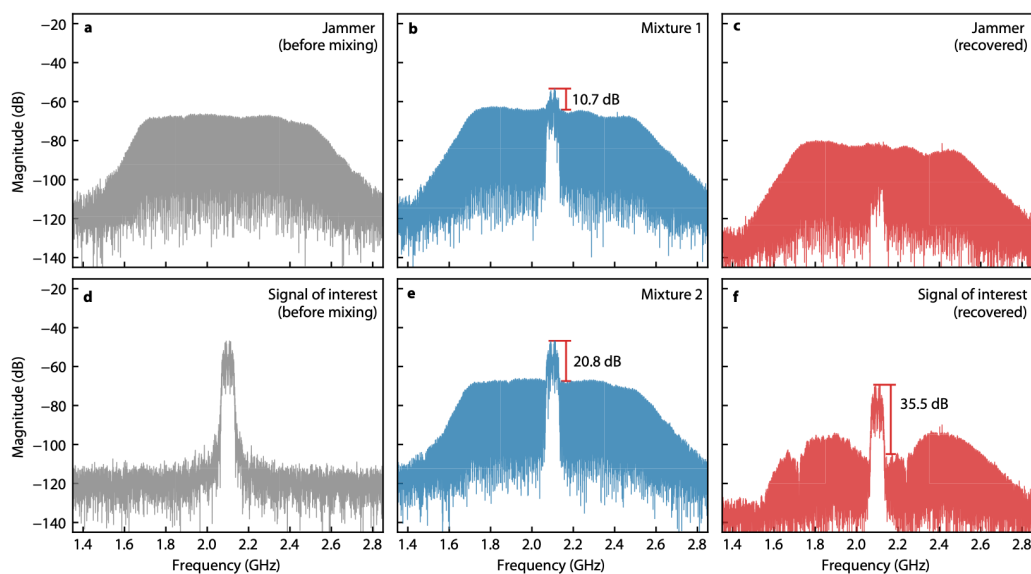
Figure 5.2: Example of BSS use in telecommunications. Panels a and d show the jammer and source signal spectra respectively. These are mixed to obtain the mixed spectra shown in panels b and e. After BSS, the jammer and source signal spectra are shown in panels c and f, respectively. The figure is taken from Zhang et al. (2023).

Another BSS application in communications systems is Radio Frequency Identification (RFID) tags. In medium and large corporate warehouses and logistics, RFID tags can be used to manage inventory, identify and locate items, monitor stock levels, track and trace items, all to improve efficiency, transparency, customer service and cost savings. However, in these situations there are typically a large number of tags that need to be read in a short period of time on the same radio communication channel. When multiple tags receive a request from a reader, tag collisions (i.e. signals interfering with each other) can occur, reducing system performance. Zhang et al. (2019) uses an identification anti-collision

algorithm based on non-negative matrix factorization (NMF), a BSS solution algorithm, to address this problem. Simulations showed that NMF outperformed other algorithms aimed at solving the same problem. It has lower cost and complexity, while achieving stable and reliable RFID performance. It also identified more tags with fewer antennas, making identification more efficient.

These are just a few examples of how BSS is being used in telecommunications, more examples can be found in the review by Luo et al. (2018) and references therein.

5.1.2 Medical Signal Analysis

Signal and image processing is widely used in the medical field for diagnosis, monitoring, and treatment. There are many biomedical signals that can be studied to gain insight. For example, the electrocardiogram (ECG) records an individual's heartbeat as a function of time, while the electroencephalogram (EEG) measures and records electrical brain activity in different regions. In addition to these medical signals, imaging techniques provide invaluable information. Functional Magnetic Resonance Imaging (fMRI) measures and visualizes brain activity by detecting blood flow. It is used to study healthy and pathological brain conditions, as well as the brain's response to different tasks. When used with EEG, it can identify epileptic seizures and detect changes in brain activity. Computed tomography (CT) uses a rotating X-ray tube to image different tissues in the human body, which is primarily useful for anatomical studies. Ultrasound imaging, on the other hand, allows visualization of muscles and internal organs, including the heart, and helps assess fetal growth and health, among many other applications. The combination of fMRI, CT, and ultrasound imaging can be used to analyze ventricular tachycardia, detect breast cancer or liver tumors, and for many other diagnostic purposes. Positron emission tomography (PET) uses radioactive tracers to image tumors and detect metastases (Najarian & Splinter 2012; Rajeswari & Jagannath 2017).

These are just a few of the possible biomedical signals that can be studied. For an overview, see Rajeswari & Jagannath (2017). However, in order to achieve the best quality diagnosis and treatment, accurate images or signals that are free of contamination from other signals are required. This can be a challenging task because there are many possible sources of contamination from noise, artifacts, or a mixture of many source signals in the medical data.

BSS Techniques in Medical Signal Analysis: BSS can help address the challenges of medical signal analysis. By effectively removing artifacts and reducing noise from observed data, BSS can improve data quality and, for example, help localize sources even in complex images. It has been used to analyze data sets affected by problems such as bearing defects, mechanical vibrations, motion artifacts in ECG signals, and fetal heart sounds, among others (Zhou et al. 2022). One notable application of BSS is the extraction of fetal ECG (FECG) signals. ECG recording is a well-established, non-invasive monitoring tool.

However, in addition to the FECG, several other sources contribute to the recorded signals. These sources include electrical noise, baseline drift (which refers to fluctuations caused by small electrode movements, respiration, changes in body position, and changes in skin conductance), fetal brain activity, muscle artifacts, and instrumentation noise.

Given the role of FECG in monitoring fetal health and reducing the risk of stillbirth and neonatal death, it is clear that removing these interfering sources from the data is extremely important. Particularly challenging is the presence of maternal ECG (MECG), which must also be removed from the data. This task is complicated by the potential overlap in frequency domain between MECG and FECG signals, which makes a simple filtering approach ineffective. In this context, BSS approaches have been investigated to overcome these challenges and extract meaningful FECG signals by effectively separating the mixed sources. These techniques offer promising solutions to overcome the complexities associated with MECG interference and enable accurate monitoring and assessment of fetal well-being (Taha & Abdel-Raheem 2020; Ramli et al. 2020).

5.1.3 Astrophysical Signal Separation

Astrophysical signals in general consist of electromagnetic radiation, high-energy particles, neutrinos, gravitational waves, and possibly hypothetical dark matter particles. Electromagnetic radiation is emitted by various objects and phenomena in the Universe, including stars, galaxies, planets, supernovae, remnants, black holes, gravitational waves, and the cosmic microwave background. These signals contain information about the physical properties, origin, and evolution of these sources, as well as the structure and history of the Universe itself. Therefore, the analysis of astrophysical signals allows us to gain insights into the Universe and learn about the various objects it contains.

However, the analysis of astrophysical signals can be challenging. Depending on the field of study and analysis, the quality and quantity of data can leave much to be desired. In addition, there are other obstacles such as interference from various sources that can affect the observed signals. For example, the cosmic microwave background (CMB), which provides information about the early universe, can be contaminated by galactic dust or synchrotron radiation, and possibly other emissions. When studying the CMB, these factors are considered noise and must be separated from the desired signal. Instrumentation also introduces noise into the data. For example, detectors may have thermal noise, electronic noise, or other problems that affect the quality of the data. Accounting for these changes over time can be even more challenging. Similar to CMB data, other sources can suffer from foreground contamination. For example, when observing a galaxy, the data may be affected by other matter along the line of sight, such as dust, gas clouds, or gravitational lensing in imaging.

To effectively study any astrophysical source, it is crucial to separate the signal from the noise. Several approaches can be used to do this. Model-based methods, for example,

rely on prior knowledge and assumptions about the data or the mixing process. They use physical models of the sources or their spectra to fit or subtract them from the data. Blind methods, on the other hand, do not require these assumptions and are based solely on the observed data (Ozgen et al. 2008; Fahes et al. 2022; Carloni Gertosio et al. 2022).

BSS Techniques in Astrophysics: An example of BSS in astrophysics is the imaging of extended sources, including galaxy clusters, individual galaxies, the diffuse interstellar medium, and pulsar wind nebulae. When applying BSS to X-ray data from these sources, their morphology and dynamics can be studied by analyzing the spectra of individual components. Supernova remnants are yet another type of extended source that can be analyzed using this method. By decomposing the different components, the explosion mechanism, gas heating, and particle acceleration can be studied and understood better. For example, Picquenot et al. (2019) used the spectra of Cassiopeia A, exploiting the expected differences between thermal emission, synchrotron emission, and background contributions, to decompose images into different physical components, see Figure 5.3.
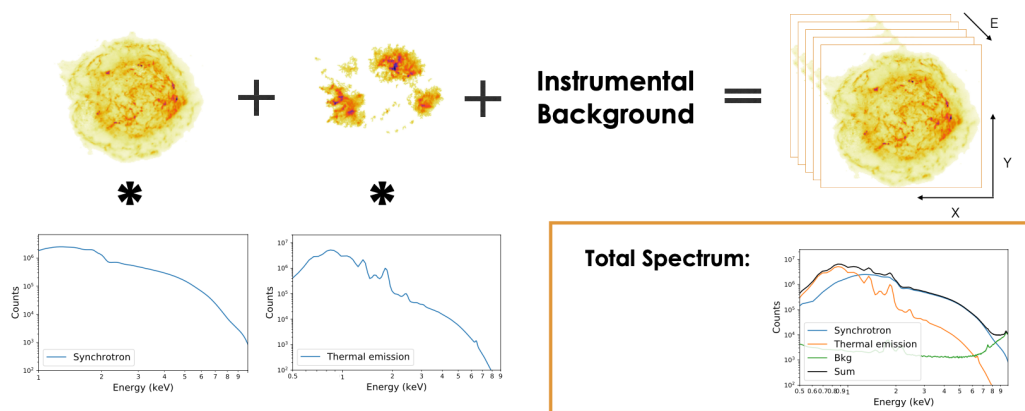
Figure 5.3: BSS can be used to spatially separate parts of supernova remnants, such as Cassiopeia A, with similar spectral properties. In this case, the model consists of a sum of images multiplied by theoretical spectra. The figure is taken from Picquenot et al. (2019).

When observing the sky at the microwave wavelength, the emitted signals are a mixture of several potential sources, as shown in Figure 5.4. Satellites such as WMAP and Planck were designed specifically to study the Cosmic Microwave Background (CMB). However, they inevitably simultaneously observe microwave signals from other sources, including galactic foreground emission. This galactic foreground emission is composed of several spectral contributions, such as free-free emission, galactic synchrotron emission, and dust emission. Analyzing each of these components separately can provide insight into the underlying processes, and BSS techniques can be used to disentangle them. The CMB

itself contains information about the origin, evolution, and structure of the Universe. To effectively study the CMB, other components such as galactic dust, synchrotron emissions, and point sources can be considered noise or interference that must be separated from the CMB signal. Once these components are successfully separated, the data can be used to estimate important cosmological parameters, including the Hubble constant, the density of matter and energy in the Universe, and the amplitude of the primordial fluctuations (Kuruoğlu et al. 2003; Ozgen et al. 2008; Bobin et al. 2015; Picquenot et al. 2019; Fahes et al. 2022; Carloni Gertosio et al. 2022). These examples are just a few of the many applications of BSS in astrophysics.
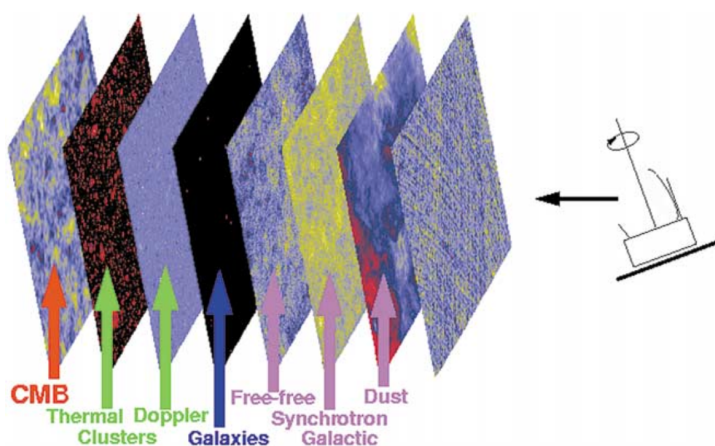
Figure 5.4: Illustration of how microwave wavelength observations are composed of different sources, such as the CMB, synchrotron emission, and dust. The figure is taken from Kuruoğlu et al. (2003).

The preceding examples of blind source separation in telecommunications, medical signal analysis, and astrophysics highlight the fact that the principle of BSS and its associated algorithms are well established and regularly used to solve related problems. Variations exist depending on the specific use case. In the following section, three commonly used BSS algorithms are introduced and briefly described, along with their respective advantages, disadvantages, and requirements.

5.2 Algorithms for Blind Source Separation

This chapter has highlighted both the importance and the challenges of blind source separation (BSS). BSS aims to extract valuable information from all kinds of fields containing mixed signals or data. Algorithms of this type allow, in principle, the separation of different sources that are combined or mixed without prior knowledge of the sources or the

mixing process. This section introduces several popular algorithms used to solve the BSS problem: Principal Component Analysis (PCA), Independent Component Analysis (ICA), and Non-Negative Matrix Factorization (NMF). While all three algorithms are classified as unsupervised learning methods and address the BSS problem, each takes a different approach and has unique characteristics, assumptions, and applications. Understanding their principles allows for a better understanding of their applications and enables informed decision making when selecting the most appropriate approach for a specific BSS task.

PCA, ICA, and NMF are all matrix factorization methods commonly used in BSS. However, it is important to note that these methods are often underdetermined, meaning that additional constraints are necessary for their solution. In the case of PCA, the constraint lies in the requirement for the components to be orthogonal to each other. On the other hand, ICA requires maximum independence among the components, while NMF additionally requires non-negativity in both the data and the components. These different constraints have different effects on the outcomes. In PCA, the components are ranked based on the variance they account for in the data. This ranking allows for the identification of the most significant components. However, NMF and ICA do not impose this orthogonality, and therefore their solutions cannot be straightforwardly ranked or ordered. Consequently, interpreting the results of NMF and ICA requires alternative approaches. One advantage of NMF, stemming from its non-negative constraint, is its intuitive nature. The additive nature of its solutions often facilitates easier interpretation. In contrast, both PCA and ICA solutions can have positive and negative components, which can cancel each other out when combined. This characteristic of PCA and ICA results often makes their interpretation more difficult.

An important parameter affecting all these algorithms is the number of components to be determined. In the case of PCA, this parameter is less important due to the orthogonality constraint. This means that higher-order components inherently have less weight than lower-order components, as defined by their variance. On the other hand, for ICA and NMF, the choice of the number of components becomes much more important. This decision has a direct impact on the decomposition and consequently on all the other components involved (Lazar & Doncescu 2009; Sompairac et al. 2019).

Since BSS is often introduced using the cocktail party problem as an analogy (see the introduction to this chapter), the following sections will use the analogy of a long drink to explain the differences and principles of the algorithms. Consider a gin and tonic as an example, where the task is to separate and identify the individual ingredients, primarily gin and tonic, while ignoring smaller contributions from additives such as pepper, cucumber, or similar elements, see Figure 5.5. By isolating and understanding the different contributions of each component, we gain insight into their role in shaping the overall taste experience.
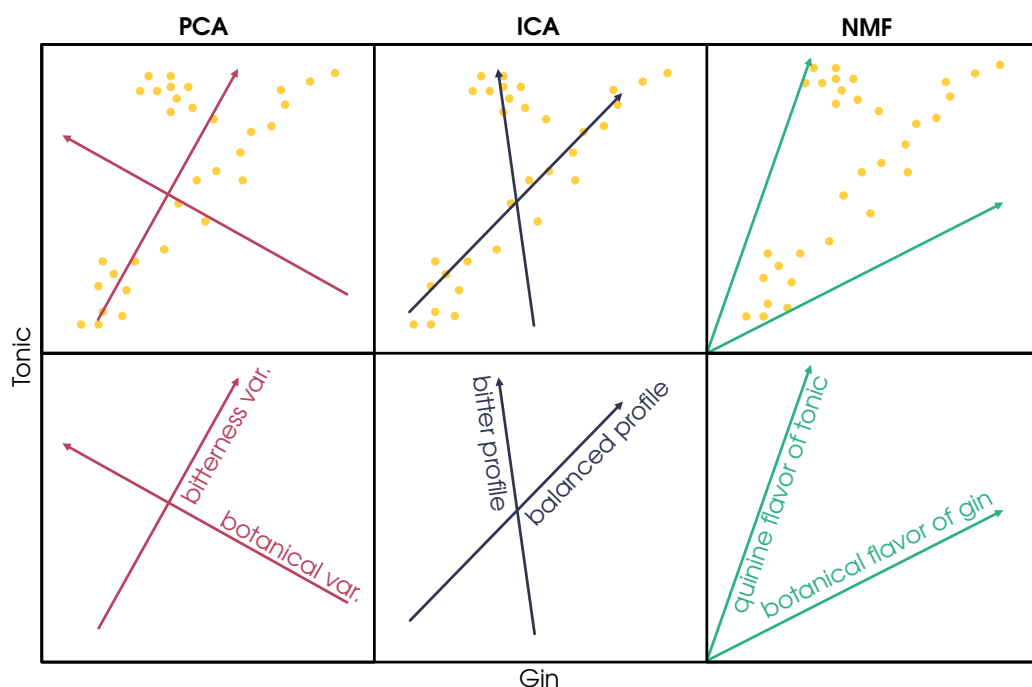
Figure 5.5: A long drink analogy to illustrate and compare BSS algorithms. A set of long drinks consisting of a mixture of gin and tonic is represented by the yellow data points. The goal is to separate the two components, gin and tonic. The left panels of the figure show the PCA approach, which searches for orthogonal components that represent the maximum variance observed in the data. In the middle panels, ICA separates maximally independent profiles. The right panels show how the most representative components of the long drink are identified using NMF. The figures are qualitative in nature and further details can be found in the accompanying text.

5.2.1 Principal Component Analysis (PCA)

Principal component analysis (PCA) was first introduced and developed by Pearson (1901). Since then, it has become a widely used method for separating linear combinations of data. PCA is a machine learning technique used to address the BSS problem, specifically as an unsupervised learning method that attempts to identify patterns within data and separate them into distinct components without any prior knowledge of the data. The basic concept of PCA is to transform the original high-dimensional data into a lower-dimensional representation by identifying the directions, called principal components, that capture the maximum variance in the data. This transformation effectively reduces the complexity of the data while preserving the most significant trends and patterns. By capturing the essential characteristics of the data, the resulting components serve as summaries that highlight the intrinsic properties of the data.

To summarize the data with a limited number of principal components (PCs), the data is geometrically projected onto these components, which have fewer dimensions than the input data. This projection aims to capture the best possible summary of the data. The first PC is determined by minimizing the total distance between data points, effectively maximizing variance. Subsequent PCs are determined in a similar manner, with the additional constraint that they must be geometrically orthogonal and uncorrelated with the previously determined PCs. In Figure 5.6, you can see how the principal components are determined using a 2D data example. It is worth noting that while PCA shares similarities with linear regression, the key difference is that PCA minimizes the perpendicular distance, rather than the response variable, between the data and the PC (Lever et al. 2017; Hassan & Ramli 2018).

PCA can be an effective way to summarize data and gain insight when the desired patterns in the data contribute to increased variance in projections onto orthogonal components. However, PCA has limitations. As shown in Figure 5.7, several conditions must be met for PCA to yield good results. First, the data must have a linear relationship. PCA relies on linear transformations, and non-linear patterns may not be adequately captured. It is also important that the patterns within the data are uncorrelated. If patterns are highly correlated, PCA may not effectively separate them into distinct components. In addition, the primary goal of PCA is to maximize the variance of the data along the identified principal components. If the goal is to identify specific clusters within the data, PCA may not be the most appropriate approach, as clustering using this technique alone can be challenging. Alternative methods, such as clustering algorithms, should be considered if the primary goal is to identify distinct clusters. Also, the data should not be scaled or adjusted based on prior knowledge, as this can introduce bias and distort the results. PCA uses the original data without any prior adjustments (Lever et al. 2017).

In the illustration shown in Figure 5.5, the two PCs are used to describe a set of observed gin and tonic long drinks. In this analogy, the PCA aims to maximize the variance of the
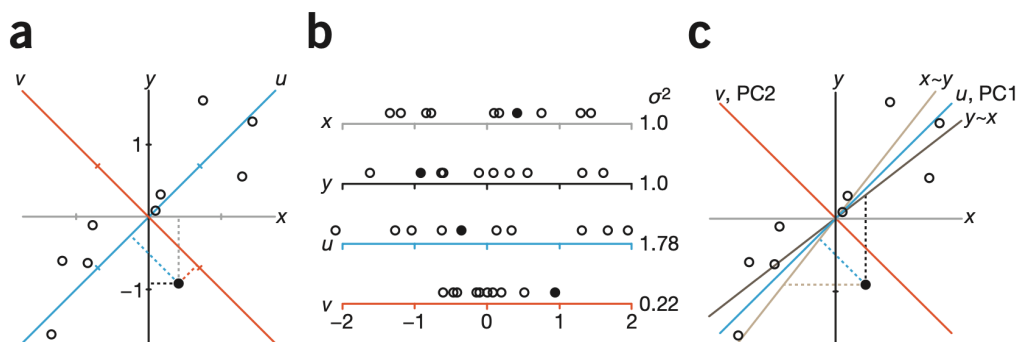
Figure 5.6: Working principle of PCA. In panel (a), 2D data points are projected onto 1D lines (u and v) along a perpendicular path, as shown exemplary for the solid circle. The projected values are shown in (b) and the variance is larger for the line u compared to v. Panel (c) shows the principal components 1 and 2 as well as the linear regressions (y vs. x in dark brown and x vs. y in light brown). The figure is taken from (Lever et al. 2017).
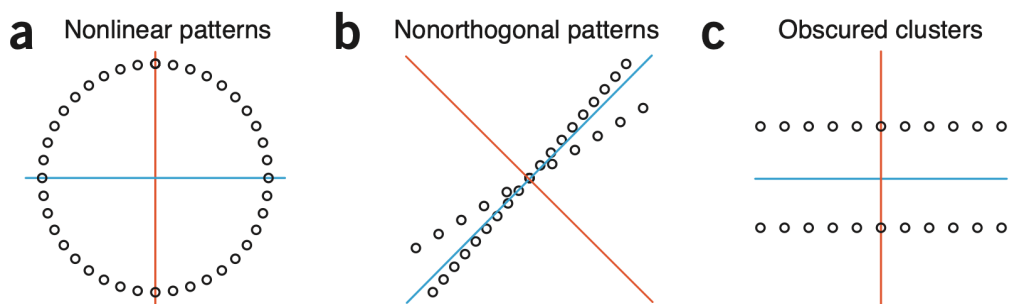

Figure 5.7: Limitations of PCA. PCA will miss patterns if the data is not linear (a), if it is not orthogonal to previous PCs (b), or if the principal component does not separate two obvious clusters (c). The figure is taken from (Lever et al. 2017).

two primary taste characteristics: bitterness and botanical notes. The first PC captures the variation in bitterness, while the second PC, which is geometrically orthogonal to the first, describes the variation in botanicals. The goal of using PCA in this context is to identify and summarize the key dimensions of taste variation in gin and tonic drinks. The first PC, representing bitterness, allows understanding the range and intensity of bitterness across the observed samples. The second PC, orthogonal to the first, highlights the distinct variations in botanical flavors. Together, these two PCs provide a summary of the flavor characteristics observed in the data set. Thus, each mixture can be mapped onto the bitterness/botanical flavor coordinate plane based on how bitter it is and what botanical flavor it has. The goal of PCA is to find and show that this is the most appropriate way to understand and describe the mapping.

5.2.2 Independent Component Analysis (ICA)

Independent Component Analysis (ICA) is another matrix factorization approach used to address the BSS problem. Its general framework was introduced and developed in the 1980s by Herault & Jutten (1986) and others. The fundamental constraint used by ICA in solving the problem is independence. The goal of ICA is to extract signals from the data that are optimized to be as statistically independent as possible. ICA is closely related to PCA and can be considered as an extension of PCA. While PCA aims to reduce the feature dimension towards the direction of maximum expression, ICA focuses on finding independent sources. In other words, ICA captures the underlying structures within the data by minimizing the statistical dependence between the extracted components. A key difference between ICA and PCA is the approach used to determine the components. ICA maximizes the non-Gaussianity of the data, while PCA relies on variance. This means that ICA is not suitable for working with Gaussian data, since it assumes non-Gaussian distributions to identify and separate independent sources (Chien & Chen 2006).

ICA is a well-established and successful technique for BSS. Among the various algorithms available, the fast fixed-point algorithm (fastICA) is widely used and is known for its fast convergence and accurate signal separation. For ICA to work best, the data should be pre-processed to reduce complexity. This typically includes centering the data to remove the mean and whitening the data, i.e. transforming it to have unit variance, to decorrelate the variables. Preprocessing increases the likelihood of a successful decomposition and facilitates a more meaningful interpretation of the results. It is worth noting that with appropriate preprocessing, ICA can be viewed as a rotation of the PCA components, see Figure 5.8, making it an extension of PCA (Hassan & Ramli 2018; Sompairac et al. 2019).

An advantage of ICA over PCA is that the results are often easier to interpret, especially when the statistical assumptions of the data are consistent with those of the ICA method. However, it is important to recognize that extracting meaningful information from the extracted sources can still be challenging in real-world applications (Sompairac et al. 2019).

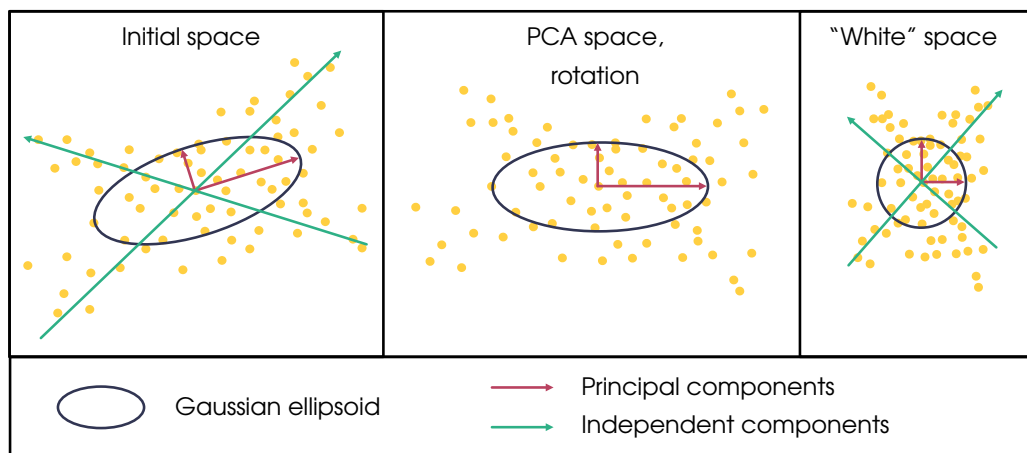For a comprehensive text on ICA, see Hyvärinen et al. (2004).

Figure 5.8: Independent Component Analysis (ICA) compared to Principal Component Analysis (PCA). ICA can be thought of as a rotation of the PCA axis when performing data whitening. The principal components are shown in red, and the independent components are shown in green. The figure is modified from Sompairac et al. (2019).

In the long drink analogy shown in Figure 5.5, the middle panel shows a schematic representation of how ICA might separate the components. By maximizing independence, ICA aims to identify the unique flavor patterns of the balanced and bitter flavors. These components correspond to the different sources contributing to the observed taste patterns in the dataset. Through the process of ICA, the goal is to disentangle the underlying sources that give rise to the observed mixture of taste characteristics in the long drink. By uncovering these independent components, ICA provides a more complete understanding of the distinct taste patterns present.

5.2.3 Non-negative Matrix Factorization (NMF)

Non-negative matrix factorization (NMF) is a matrix factorization technique used in BSS problems that makes use of a non-negativity constraint. In NMF, both the input data and the resulting decomposed matrices are necessarily non-negative. This constraint is based on the assumption that the underlying sources in the data are non-negative in nature. In the analogy of the long drink depicted in Figure 5.5, NMF aims to identify relevant patterns without explicitly separating the data. Instead, it seeks to find the most representative taste components that contribute to the overall flavor profile. For instance, in the case of the long drink, NMF would identify the dominant taste components such as the quinine flavor of the tonic and the botanical flavor of gin.

NMF is an unsupervised learning method that learns how to represent the data based on its constituent parts. It achieves this by finding a linear projection of the original data onto a new set of base directions or components. Unlike PCA, where the basis vectors are orthogonal and ordered by maximum variance, NMF vectors tend to align with single clusters or components. This implies that NMF identifies the most discriminating subspace of the data, capturing the most relevant patterns for the given problem (Lazar & Doncescu 2009; Hassan & Ramli 2018).

The example in Lee & Seung (1999) provides valuable insight into the qualitative differences between PCA and NMF algorithms when applied to facial image analysis, see Figure 5.9. Both PCA and NMF can represent a face as a linear combination of base images, but their results have qualitatively different characteristics. When using PCA, the decomposition of faces produces "eigenfaces", which can appear as distorted versions of typical faces. These eigenfaces represent the principal components of facial variation in the data set. NMF, on the other hand, produces a different set of basis images that capture the features of faces, resulting in a representation that is more intuitive to our perception of a face. The NMF basis images correspond to additive combinations of facial features, which is consistent with the notion of assembling parts to form a complete entity. This parts-based representation is learned through NMF's ability to enforce non-negative and additive combinations (Lee & Seung 1999).

It is important to note that NMF is not limited to image analysis and can be applied to various types of data. Text analysis is a completely different domain where NMF is well suited. In this context, a collection of documents can be analyzed using NMF to decompose them into semantically related words that are grouped into meaningful semantic features. By using NMF, it becomes possible to distinguish between multiple meanings of the same word and to extract interpretable information from text data. The easy interpretability of the results makes NMF an attractive choice for many BSS problems, as it facilitates a clear understanding of the underlying patterns and components present in the data (Lee & Seung 1999).
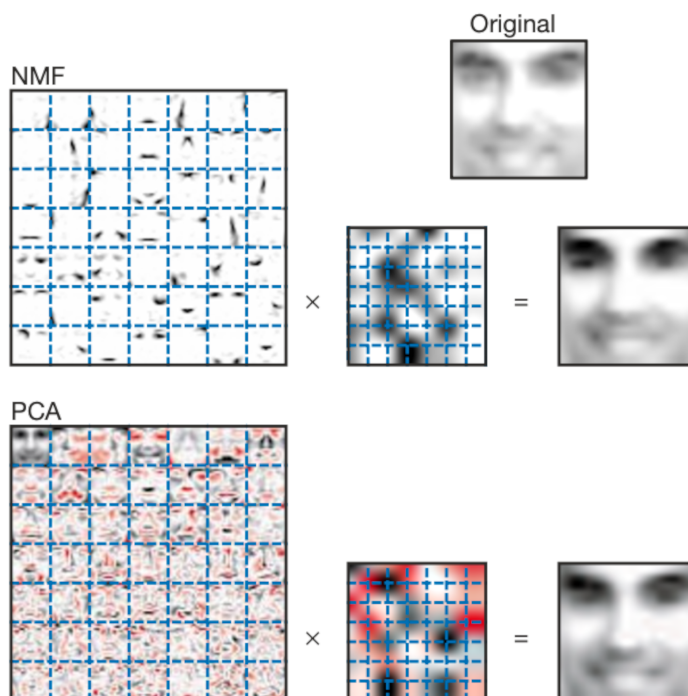
Figure 5.9: Decomposition of a set of face images using different techniques. The upper part of the figure shows the NMF decomposition with its parts-based representation. The lower part of the figure shows the PCA solution. Both solutions are considered adequate, but each has different limitations, as explained in the text. In the images, the left part shows 49 basis images, where the black pixels represent positive values, while the red pixels represent negative values. The middle image shows the mixing coefficients, and the resulting superpositions are shown on the other side of the equals sign. In addition, an example of a face is shown above the NMF solution. Note that only the NMF solution decomposes the data into different face parts, which is more intuitive for our perception of faces. The figure is taken from Lee & Seung (1999).
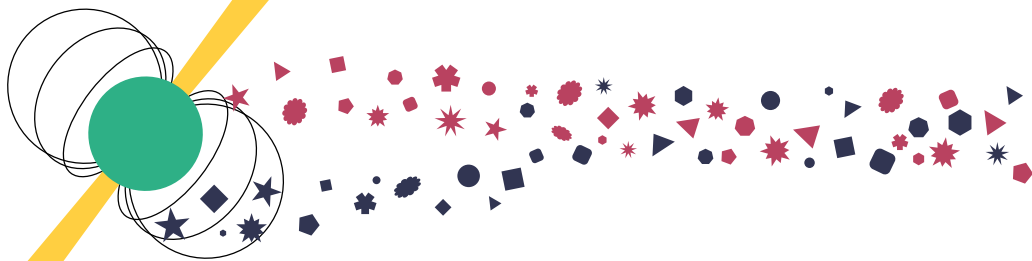
6. Phase Correlated Variability Analysis (PCVA)

Understanding the pulse profiles in X-ray pulsars (XRPs) remains a complex problem, with many aspects still not fully understood (Section 3.2). A meaningful physical interpretation requires an understanding of the geometry of the emission region and the associated intrinsic beam patterns. This work presents a novel data-driven approach that provides an independent way to separate the different contributions within a pulse profile. It is based on the application of blind source separation (BSS, see Chapter 5) to flux observations.

The observed light curves of XRPs exhibit stochastic variability (Section 3.1.4) that approximates variations in the accretion rate on the surface of the neutron star. By considering two magnetic poles, the accretion rate for each pole is expected to be partially independent, giving rise to two separate signals. Each of these individual signals makes a different contribution to the overall pulse profile. At each phase, the contribution is defined by the geometry, intrinsic beam pattern, emission structures, gravitational light bending, etc., and thus represents a mixing operator. Using BSS techniques, it becomes possible to separate these contributions without any prior knowledge of the original sources or how they are mixed.

The application of BSS to the analysis of X-ray pulsar profiles will be termed "phase correlated variability analysis" (PCVA). This specific term is justified by the additional steps that are specific to the problem of reconstructing the contributions of each pole, as well as by the focus of PCVA on the weight matrix rather than on the signals themselves, which is normally what BSS is interested in, since the weight matrix represents the individual pulse profiles associated with each magnetic pole. In the following sections, the specifics of the methodology will be explored and a detailed explanation of how it works will be provided.

This chapter is divided into two sections. The first section focuses on introducing the PCVA technique and its basic concepts, as well as some observations that support the idea.

In the second section, the properties and applicability of PCVA in the context of the pulse profile decomposition problem are discussed and illustrated by a series of simulations using realistic XRP light curves. Different BSS algorithms are compared to evaluate their performance, while also exploring the constraints and limitations of the method. Finally, verification and robustness tests are performed to ensure the reliability and accuracy of PCVA.

6.1 Introducing the PCVA

PCVA is the name of an observation-driven approach developed here that aims to improve our understanding of the emission mechanisms in the vicinity of accreting neutron stars by decomposing the observed emission into distinct components originating from different physical regions. This section introduces the motivation and the concept of PCVA. First, the concept and idea behind PCVA is discussed, supported by observations such as the typical power spectra of X-ray pulsars (XRPs) and the correlation information of the time variability characteristics. These observations suggest that certain signal components may be partially independent, indicating the potential separability of each component. Finally, we reformulate the problem using the framework of the Blind Source Separation (BSS) problem.

As discussed in Section 3.2, interpreting the pulsed emission from XRPs is a challenging task. Several approaches have been applied to this task. In Kraus et al. (1995), a methodology for decomposing pulse profiles was proposed (Section 3.2.3), but it relies on several assumptions. One of the primary assumptions is that the contributions from the two magnetic poles of the neutron star are inherently identical and symmetric in phase, with only a phase shift between them in the observed pulse profile. This phase shift could be attributed to an offset of the dipole magnetic field relative to the center of the neutron star. While this assumption is justified to some extent, it is important to note that there is no unique solution, and additional criteria must be employed to select the most appropriate solution. Although some individual sources have been analyzed using this approach, it is important to independently verify the underlying assumptions. Polarimetry measurements are emerging as a valuable new tool for determining the orientation of the magnetic field of XRPs relative to the observer (Section 3.1.3). This can help in finding solutions to the pulse profile decomposition proposed by Kraus et al. (1995, 1996). Even with the availability of polarimetric data, accurate reconstruction of the intrinsic beam patterns of XRPs still relies on the assumption of intrinsic symmetry of the beam patterns for the two magnetic poles. It is important to note, however, that the geometry determined by polarization results is not without its challenges. These results are highly dependent on the specific models used, and recent results from Doroshenko et al. (2023) raise concerns about their reliability. It is therefore important to independently verify the assumption of intrinsic symmetry and geometry and to explore alternative methods for reconstructing

the beam patterns.

A major challenge in interpreting XRP observations is that all observed properties of XRPs depend on the geometric configuration of the emission regions, which is not known a priori. Consequently, the intrinsic beam patterns of the emission regions remain highly uncertain. This inherent uncertainty complicates the verification of theoretical calculations and the interpretation of observational results, such as pulse phase-resolved spectroscopy or variations in pulse profiles. Reconstructing the geometry of the accretion region and its emission properties is therefore an essential first step in resolving these uncertainties. However, this requires new and innovative approaches to the analysis of observational data. To derive meaningful interpretations from XRP observations, such as light curves, pulse profiles, and spectra, it is essential to accurately determine the contributions of the two emission regions associated with the magnetic poles of the neutron star as a function of the pulse phase. This process is often referred to as pulse profile decomposition, where the individual contributions from each pole are extracted, resulting in "single-pole pulse profiles".

6.1.1 Conceptual Framework of PCVA and Supporting Observations

The light curves of XRPs show significant variability, as can be seen in Figure 6.1 for the example of a Cen X−3 observation.[1] This variability is present both on longer timescales and from pulse to pulse, showing stochastic fluctuations in the individual pulse profiles. The variability can be further studied in the power spectra, an example is shown in Figure 6.2.[2]

In addition to the strong peak around the spin frequency, these power spectra usually show a break around the spin frequency of the pulsar. They also exhibit a distinct type of noise, called red noise, which is characterized by its presence over a wide range of frequencies (this was discussed in more detail in Section 3.1.4). This observed variability is closely related to the flickering noise generated by instabilities within the accretion disk (Lyubarskii 1997). The flickering noise propagates to the inner accretion disk and the mass accretion rate of the neutron star, which in turn can be seen in the observed flux variability. Fluctuations at lower frequencies are associated with the Keplerian timescale at a certain distance within the disk where the fluctuations originate. Beyond the spin frequency, the presence of the pulsar's magnetosphere truncates the disk, resulting in the suppression of variability at these timescales (Revnivtsev et al. 2009). However, despite this suppression, the power spectrum shows that the variability is not completely eliminated at higher frequencies. Substantial noise is still detected around the pulsar's spin frequency, showing that the variability is still present in this range.

---

[1]Most of the figures in this thesis were created using the matplotlib Python module (Hunter 2007), and the data was processed with numpy (Harris et al. 2020).

[2]The power spectrum was generated using the Python Stingray module (Huppenkothen et al. 2019; Huppenkothen et al. 2019).
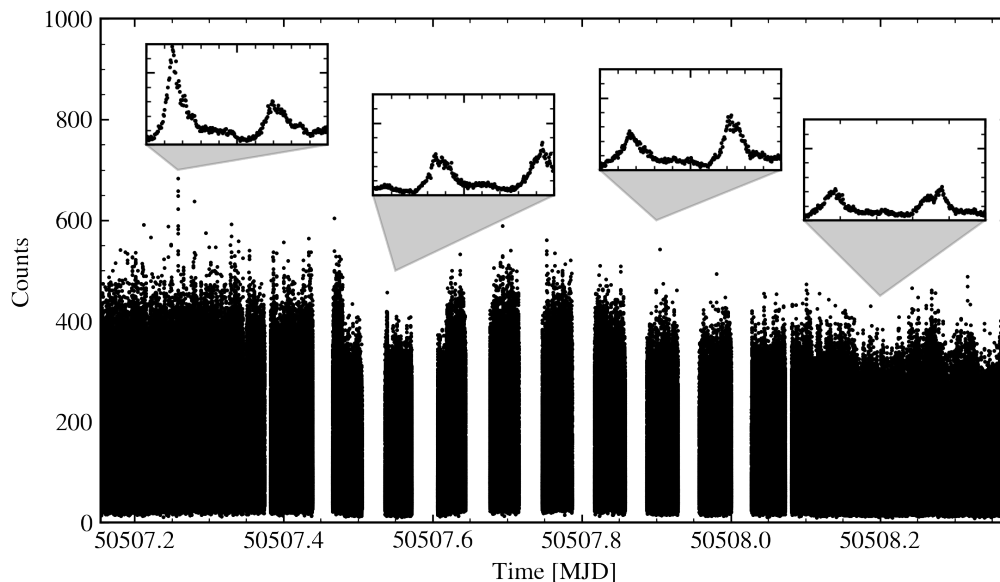
Figure 6.1: The light curves of XRPs, shown here as an example of Cen X−3, are typically highly variable, and stochastic variations can be seen even from pulse to pulse.

This highly variable accretion occurs at the two magnetic poles of the neutron star. The magnetic field of the pulsar can be very complex, but the radial dependence of a 2^l pole scales as $1/r^{l+2}$, which means that the magnetic dipole ($l = 1$) scales as the inverse distance cubed, while a quadrupole ($l = 2$) scales as r^{-4}, and so on. Therefore, as the distance increases, the contributions of the higher order moments become increasingly insignificant compared to the lower order moments, and the magnetic dipole field dominates at larger distances. In the case of disk accretion, this means that the dipole moment dominates at the inner accretion disk where matter couples to the magnetic field lines and is redirected by them toward the magnetic poles of the neutron star. The dipole is generally inclined so that opposite poles sample opposite sides of the accretion disk, as shown in Figure 6.3. The matter accreting to the two magnetic poles is therefore most likely coming from two opposite parts of the disk. This means that the fluctuations in the accretion rate should be at least partially independent for the two poles of the neutron star. The situation is even simpler in the absence of an accretion disk, as in the case of direct wind accretion, where it can be expected that individual clumps of matter will accrete mostly at one of the poles.

The phase-resolved variability of the accretion rate and the corresponding observed flux variations are illustrated in Figure 6.4. The top two rows of the figure show a sketch of how the mass accretion rates at the two magnetic poles of the neutron star could fluctuate
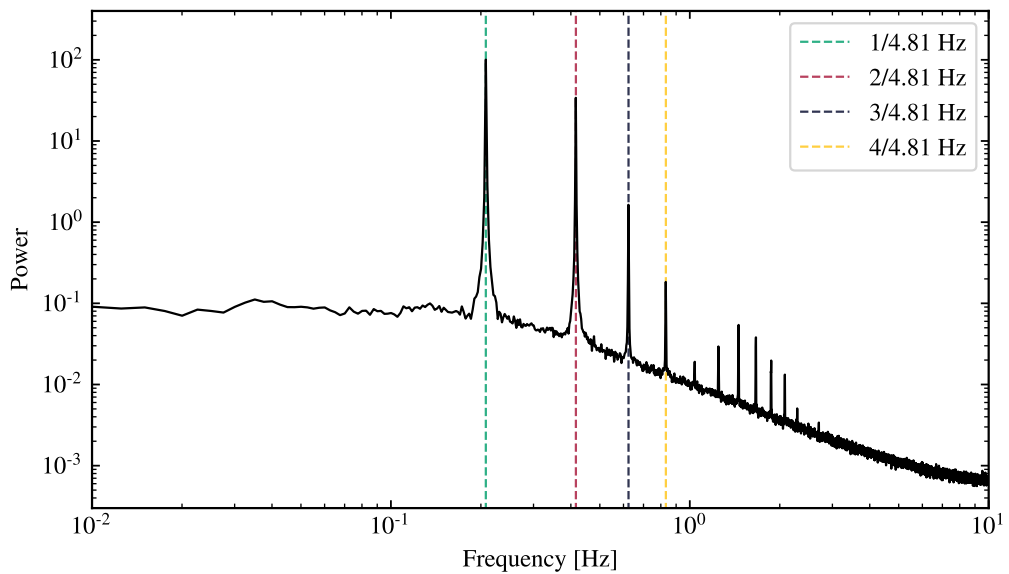
Figure 6.2: The power spectrum of Cen X−3 is shown here as an example. The peaks in the spectrum correspond to the spin frequency of the pulsar, which rotates approximately every 4.81 seconds (green dashed vertical line), and its harmonics at integer multiples of this fundamental frequency. Note that there is significant aperiodic variability in a wide range of frequencies, including around the spin frequency.
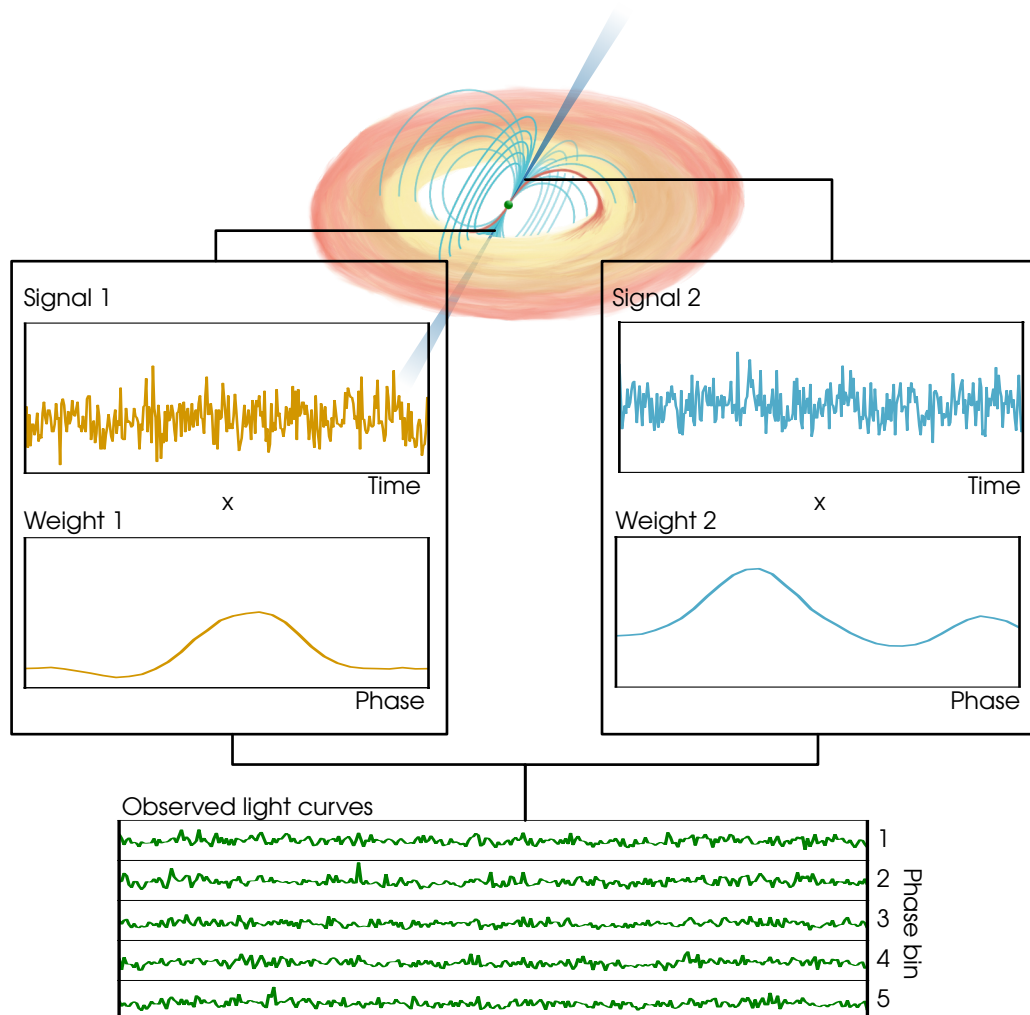
Figure 6.3: At the distance of the inner accretion disk, where the matter is stopped and couples to the magnetic field lines, the magnetic field is dominated by the dipole moment. It then follows the field lines to the magnetic poles of the neutron star, where it emits X-rays. The accretion rates at each of the poles give rise to the observed fluxes, the signals. The fluctuations in the accretion rate are roughly translated into fluctuations in the observed X-ray flux. The intensity of the beam at a given pulse phase is the single-pole pulse profile. In this context, this can also be referred to as the weights or weight matrix. These weights act as coefficients that systematically offset the observed flux. Thus, the flux in different phase bins will appear more correlated if it originates from the same pole, but less so if both poles contribute. The observed phase-resolved light curve is the result of mixing these signals with the weights. The sketch is not to scale.

aperiodically and independently with the pulse-to-pulse variability outlined above. During
each rotation of the pulsar there are pulse-phase intervals during which emission from
one or both poles is observable, depending on geometry, beam pattern, gravitational light
bending, and so on. These variations give rise to the single-pole pulse profiles seen on the
left of the sketch in Figure 6.4.
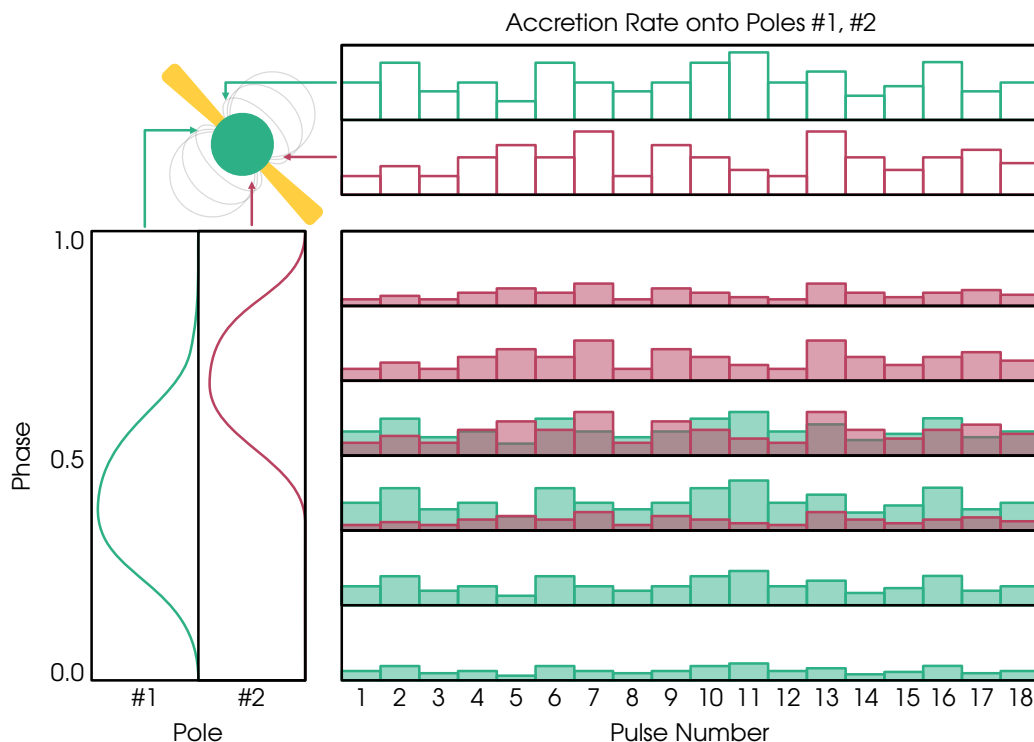
Figure 6.4: The mass accretion rate to the two magnetic poles of the neutron star is shown
in the top part of the image, closely related to the observed X-ray flux. The single-pole
pulse profiles that modify this flux are shown on the left. The resulting phase-resolved
"light curves" are shown in the "phase matrix" on the right. Fluxes in phase bins where
only one pole contributes are highly correlated, while in phase bins where the second pole
contributes, the correlation is greatly reduced. See the accompanying text for more details.

The flux resulting from the mass accretion is modulated by the shape of the pulse profile
as the pulsar spins. When only one pole is considered, this implies that the pulse-to-pulse
flux of that pole is offset, or scaled. This can be seen in the figure, as in some phase bins no
flux is observed when the pulse profile is zero, while in other phase bins the flux is scaled
according to the shape of the profile of that pulse. The same is true for the second pole. If
we consider two phase bins in which the observed emission is dominated by the emission

from one pole, as shown for example in the top two phase bins for pole 2, the emission from these generally arbitrary two phase bins will be highly correlated. The same holds true for the other pole, in other phase bins.

However, if the total emission in a phase bin is the sum of the contributions from both poles, the emission in two phase bins will appear less correlated. For example, correlating the emission from the first row with the third or fifth row in Figure 6.4 would result in a lower degree of correlation due to the combined contributions from both poles. In essence, the correlated emission from one pole is "diluted" by the additional noise from the other pole.

These ideas can be verified by observation. We can bin the observed light curve (Figure 6.1) into n pulse-phase bins and display each pulse in a column, as shown in Figure 6.5. This will be referred to as the phase pulse matrix. It shows the pulse-to-pulse variability of the individual pulses (columns in the matrix), and each phase bin (rows in the matrix) contains the light curve of that bin. To illustrate the discussed correlation properties associated with independent accretion at the two poles, the Pearson correlation coefficient can be calculated for each pair of pulse-to-pulse light curves in the phase bins. The results for each pair can be encoded in a phase correlation matrix, shown in Figure 6.6. This example of Cen X−3 data reveals a complex shape of the phase correlation matrix. The degree of correlation observed in the data is not consistently around one or zero. Instead, it fluctuates across different phase bins, which is consistent with the notions discussed earlier. This variability in the degree of correlation implies that the signals in Cen X−3, and potentially in other XRPs, are not fully correlated. Rather, the degree of correlation changes throughout the rotation period. Therefore, it can be concluded that the assumption of partial independence holds, as the signals have varying degrees of dependence on each other.

The variation in the degree of correlation across different phases can be attributed to the changing contributions of the two poles. A higher degree of correlation corresponds to emission from one of the two poles, while a lower degree indicates contributions from both poles. The idea is to use this information to distinguish and separate the contributions of the two poles. However, since the individual contributions from each pole and their mixing are unknown, this problem can be reformulated as a blind source separation task.

For PCVA, it should be noted that on timescales shorter than the spin period of the pulsar, multiple observers would be required around the neutron star, which is not possible. On the other hand, on timescales longer than the spin period, the variability of the accretion rate at the two poles is likely to be intrinsically correlated. Therefore, since PCVA relies on the independence of the light curves at the two poles, it is performed by exploiting the variability on the timescale of the pulsar's spin. PCVA exploits this aperiodic variability on the timescale of the spin frequency, or in other words, PCVA is performed by exploiting the pulse-to-pulse variability of the X-ray flux at a given pulse phase.
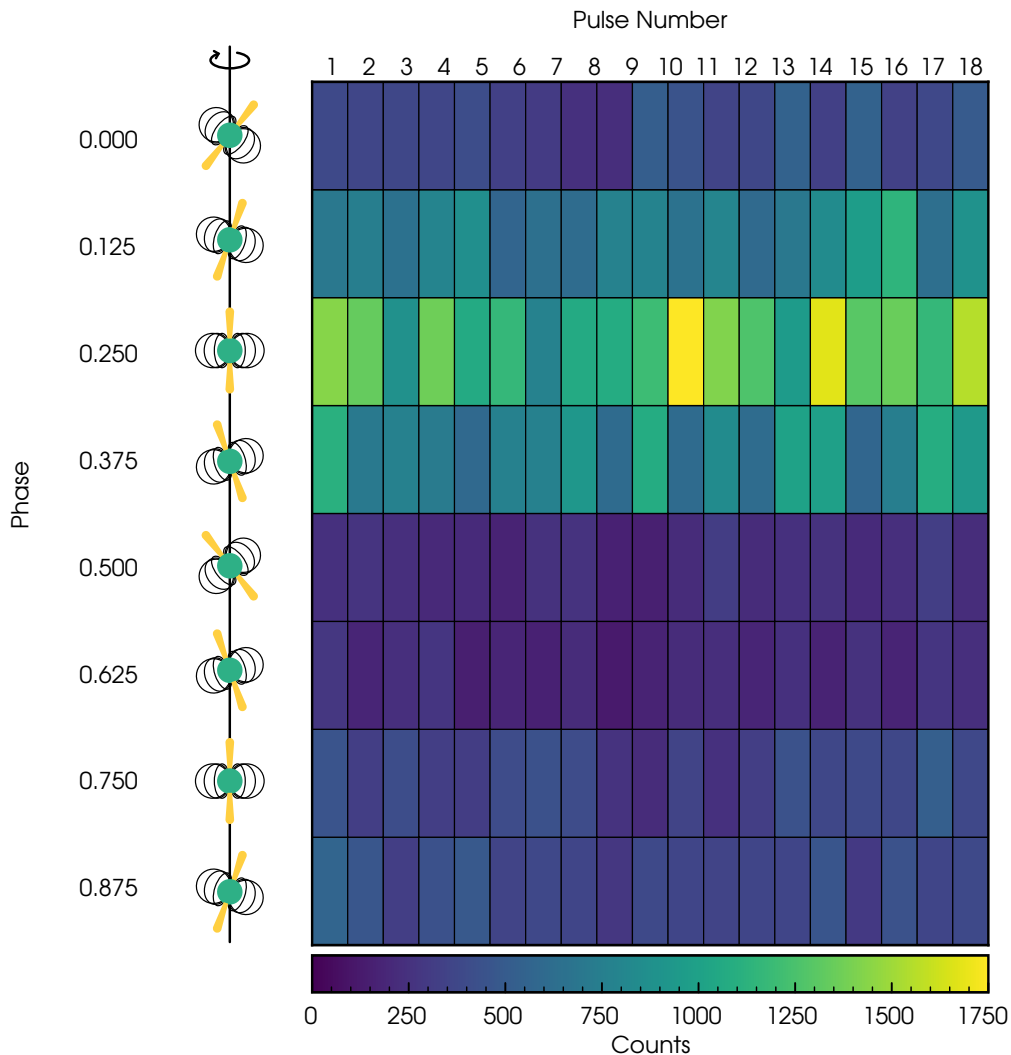
Figure 6.5: Illustration of a phase pulse matrix. On the left is the phase of the pulsar's spin in 8 phase bins, along with a sketch of the pulsar's position (with arbitrary zero phase, geometry, and observer's line of sight). Shown are 18 pulses of Cen X−3 as an example. The colors indicate the variability in the number of photons detected, revealing the pulse-to-pulse variability within each phase bin. If the matrix is read per column, the individual pulse profiles that exhibit some stochastic variability can be retrieved. Alternatively, reading the matrix by row provides light curves for each phase bin. The PCVA relies on the variability on the timescale of the pulsar's spin, i.e. its pulse-to-pulse variability.
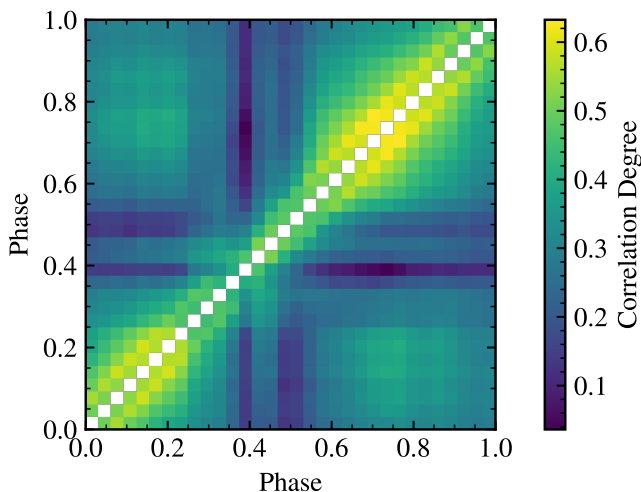
Figure 6.6: The phase-correlation matrix of Cen X−3 shows the Pearson correlation coefficient for each pair of light curves in two of 32 phase bins.

6.1.2 PCVA as a Blind Source Separation Problem

As introduced and described in Chapter 5, the blind source separation (BSS) problem refers to a scenario where there are unknown sources or signals that are mixed with an unknown mixing operator. In the case of PCVA, we are interested in two signals:

$$s(t) = [s_1(t), s_2(t)]^\mathsf{T},$$

where T is the transposition. These signals correspond to the observed emission produced by the accretion at each of the two magnetic poles. However, before these signals are observable, they are mixed with a mixing operator or matrix, denoted as

$$A = [a_{ij}] \in \mathbb{R}^{n \times 2}.$$

Here, A is a matrix representing the mixing process. Consequently, the resulting observations that result from mixing the signals $s(t)$ using the operator A can be represented as another vector:

$$x(t) = [x_1(t), x_2(t), \ldots, x_n(t)]^\mathsf{T}.$$

The vector $x(t)$ contains the observed data, with several components mixed with different mixing coefficients. In PCVA, the value n is the number of phase bins used in the analysis. The choice of n depends on factors such as data quality and the scientific

question at hand. For example, if there are specific features within the pulse profile that need to be resolved, the appropriate value of n should be determined accordingly.

This particular scenario of mixing source signals has been illustrated in Figure 6.4, where the signals s_1 and s_2 representing the observed flux emerging from the accretion process are shown in the top two rows, i.e. the top matrix. On the left side of the image is the mixing matrix A. This matrix, also called the weight matrix because it represents the modulation factors or mixing coefficients for the fluxes, corresponds to the single-pole pulse profiles. It contains the information on how the flux is modulated for each phase bin. The observed signal vector, denoted x, captures the source signals with different intensities defined by the coefficients. Mathematically, we can express this relationship as $x = As(t)$, where A is the mixing operator and $s(t)$ is the source signals. Neither the source signals nor the mixing operator are known. The primary goal is to recover the source signals and determine the mixing operator. This is done by finding a matrix

$$B = [b_{ij}] \in \mathbb{R}^{n \times 2}.$$

By applying the matrix B to the observations, $y = Bx(t)$, an estimate of the source signals can be obtained:

$$y(t) = [y_1(t), y_2(t)]^\mathsf{T}.$$

In other words, the vector $y(t)$ represents the estimated values of the source signals based on the observations. The process of determining B allows the original source signals to be separated and reconstructed from the observed mixed signals and in principle can be accomplished with any BSS algorithm, such as PCA, ICA, or NMF, described in Section 5.2. To better differentiate between the terms, it is important to understand their relationships. BSS refers to the general problem of separating mixed signals into their underlying components. Within the category of BSS, PCA, ICA, and NMF are algorithms that address this problem. On the other hand, PCVA is a specific application of BSS that uses the NMF algorithm to solve the problem.

In the PCVA application, the estimated values of the source signals y_1 and y_2 serve as approximations for the original signals s_1 and s_2. However, PCVA is primarily concerned with determining the weights, also known as the mixing matrix or single-pole pulse profiles. Recovering these weights is the primary goal of PCVA, and since any blind source separation recovers both signals and weights simultaneously, this is not a problem. As discussed in Chapter 5, the blind source separation problem is generally underdetermined, meaning that there are multiple possible solutions. To address this, several algorithms have been developed, each making different assumptions. In the context of PCVA, we will now use several of these algorithms for comparison.

6.2 Development of PCVA through Simulations

To develop the method, demonstrate and verify that blind source separation can be used to reliably decompose pulse profiles in XRPs, a series of simulations were performed. Light curves were simulated that contain information about the underlying accretion rate fluctuations and the mixing, which is defined by the mixing coefficients. As described earlier, this mixing operator characterizes the intensity contributions of the two poles throughout the rotation of the pulsar, and is also referred to as the single-pole pulse profile. The goal of PCVA is to recover these profiles from the mixed data, and in the simulations, the reconstructed results can be compared to the input to verify the method and to compare the performance of different algorithms to find out which works best given the quality of the available data. The simulation steps used are described below.

Two signals have been generated for each simulation, and it is assumed that the accretion rate fluctuations at the two poles have similar variability properties as the total observed flux. These are described by typical red-noise power spectral density (PSD) spectra with a break around the spin frequency, as expected for XRPs. The simulations were performed using the Python package pyLCSIM (Campana 2017) and produced two independent time series with stochastic fluctuations. The broken power law parameters, listed in Table 6.1 (Fürst et al. 2019; Mönkkönen et al. 2022), were chosen according to typical parameters for accreting XRPs, and one realization is shown in the top panel of Figure 6.7.

Table 6.1: Parameters of the light curves for the pyLCSIM simulations based on red-noise type power spectral density spectra. The values are typical for accreting XRPs (Fürst et al. 2019; Mönkkönen et al. 2022).

Parameter	Value
Exposure	10 ks
Average count rate (RXTE/PCA)	100 cts/s
Spin period	1 s
PSD normalisation	1
Power law index 1	1
Power law index 2	2
Break frequency	1 Hz

The coefficients corresponding to the single-pole pulse profiles for each pole define the mixing or weights matrix. To simulate the single-pole pulse profiles, we assumed that they have approximately the same complexity as the observed total pulse profiles of typical XRPs. Therefore, this matrix was parameterized by a smoothed sum of six random Gaussian functions. An example of single-pole pulse profiles and their sum, which would
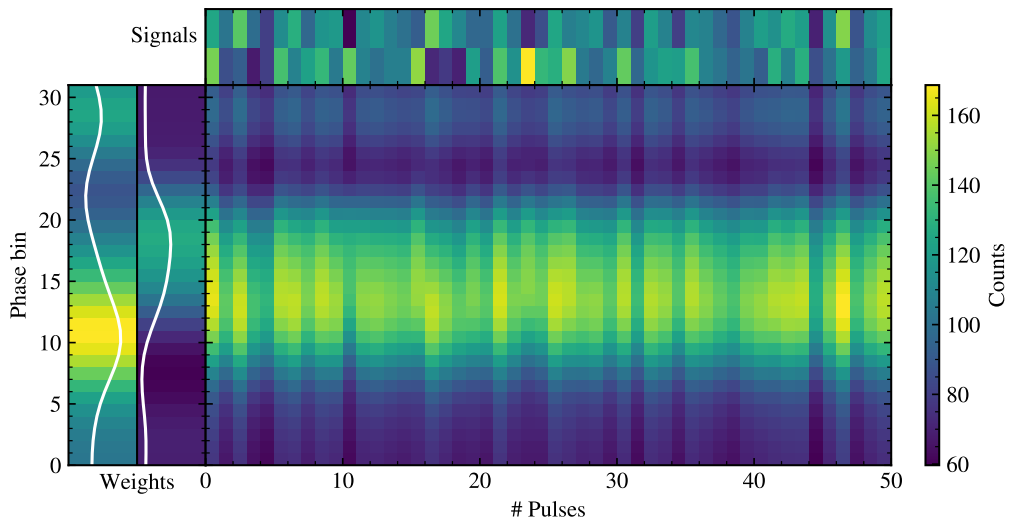
Figure 6.7: Simulation data to develop PCVA. The top panel of the figure shows two signals that roughly correspond to the mass accretion rate at the two poles of the neutron star. These are based on broken power law power spectral densities. On the left are the mixing coefficients, also known as single-pole pulse profiles. They were simulated from the smoothed sum of six random Gaussians, and only one of the possible realizations is shown here. Multiplying the signal and mixing matrices produces the phase pulse matrix shown in the middle. Only the first 50 pulses are shown as an example.

be the observed pulse profile, is shown in the left panel of Figure 6.7. However, since the parameters of the Gaussians that make up the profiles have been varied randomly, this is only one possible realization.

The phase pulse matrix is then constructed from the combination of the signal and the mixing matrix by matrix multiplication, and is shown in the center of Figure 6.7. By calculating the Pearson correlation coefficient of the light curves of each phase bin, the corresponding phase correlation matrix, shown in the middle panel of Figure 6.8, can be determined. This phase correlation matrix shows a much higher degree of correlation compared to the previously presented example of a Cen X−3 observation in Figure 6.6, also shown in the left panel of Figure 6.8 for comparison, if we simply use simulated rates to calculate it. This discrepancy is due to the fact that photons emitted by distant sources eventually reach detectors that are inherently Poisson-limited. This becomes very important for low count observations. In observations, the flux is observed rather than an accretion rate, which means that the simulated light curves and phase matrices must be scaled to account for the limited count statistics in real XRP observations. To achieve this, the simulated phase pulse matrix was used to draw data from a Poisson distribution. This makes the simulation more realistic by introducing random uncorrelated noise and reducing the overall degree of correlation. An example of the resulting phase correlation matrices before and after taking the Poisson limitations into account is shown in Figure 6.8.
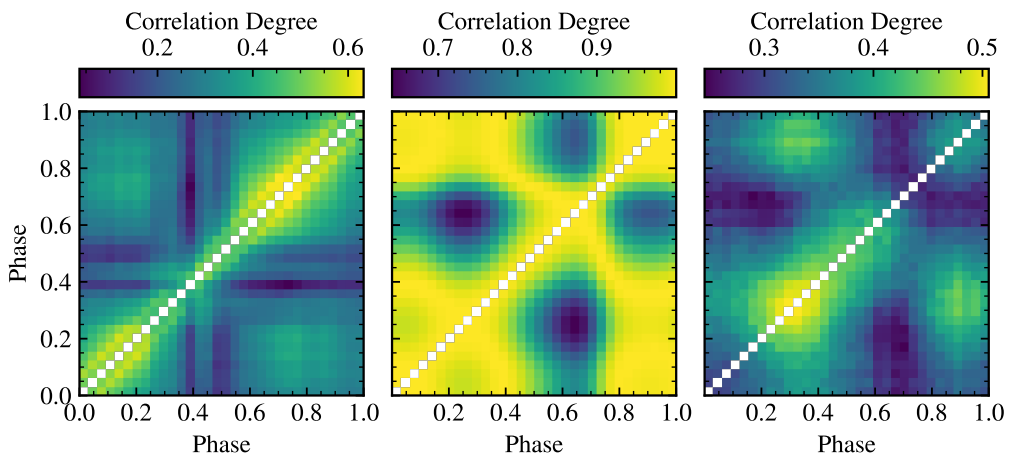
Figure 6.8: The left panel shows the phase correlation matrix of an observation. The middle panel is the phase correlation matrix of a simulation. The right panel shows the same data as the middle panel, but now corrected for Poisson statistics. Note that the features of the matrix are not to be replicated in this simulation, only the scaling of the correlation degree.

   To ensure meaningful and comparable results in the subsequent comparison of different algorithms, it is important to identify and outline the steps for PCVA that have emerged. Since our problem involves counts and count rates that cannot be negative due to the non-negativity constraint, the use of the Non-Negative Matrix Factorization (NMF) algorithm is appropriate. Therefore, NMF is used to analyze simulated data, which serves as an illustrative example to demonstrate the necessary steps in addition to the initial decomposition. In addition, NMF is expected to provide physically meaningful results that are easy to interpret. Therefore, the NMF algorithm was implemented in Python using the Scikit-learn package (Pedregosa et al. 2011)[3]. However, I also tried other methods and found that NMF indeed outperformed other methods when applied to simulated data, as described in Section 6.2.1. For the following description, I will limit myself to NMF, which was used to decompose the simulated phase pulse matrices and estimate the mixing matrix, which can then be compared to the input from the simulation.

   In Figure 6.9, the input weights of the simulation are shown as solid lines, and the recovered contributions are shown as dashed lines. The shape of the input contributions is well reconstructed. However, there is a clear discrepancy in the relative scaling of the two single-pole pulse profiles. This discrepancy is expected due to the nature of the BSS algorithms, including NMF, which aim to identify maximally independent source signals. These signals may not correspond to the true mixing if the signals are correlated to some degree. In the case of XRPs, the flux variability from both poles is expected to be correlated at lower frequencies, resulting in a bias during BSS reconstruction. The scaling discrepancy between the two contributions obtained from the initial NMF decomposition can be addressed by adjusting the scaling and matching the simulated and observed phase correlation matrices to reproduce the overall degree of correlation between the signals. In practice, this can be accomplished by comparing the phase correlation matrices of the initial simulated phase matrix with a new phase correlation matrix derived from a simulated light curve using the resulting and rescaled NMF decomposition. Figure 6.9 shows the initial phase correlation matrix and that of the simulated phase correlation based on the NMF decomposition in the "Input" and "Decomposition" panels, respectively. By scaling the NMF decomposition components, re-simulating, and comparing the correlation matrices, a minimization can be used to determine the optimally rescaled decomposition that takes into account the observed correlation properties. These rescaled components can be seen as dotted lines in Figure 6.9. The "Scaling optimized" panel in the figure shows the correlation matrix based on the optimally rescaled components.

   Note that in principle, one could bypass the NMF and search for the mixing matrix directly by comparing the correlation matrices directly. However, this would require minimizing a noisy cost function with a large number of parameters, which is difficult

---

[3]https://scikit-learn.org/stable/modules/generated/sklearn.decomposition.NMF.html
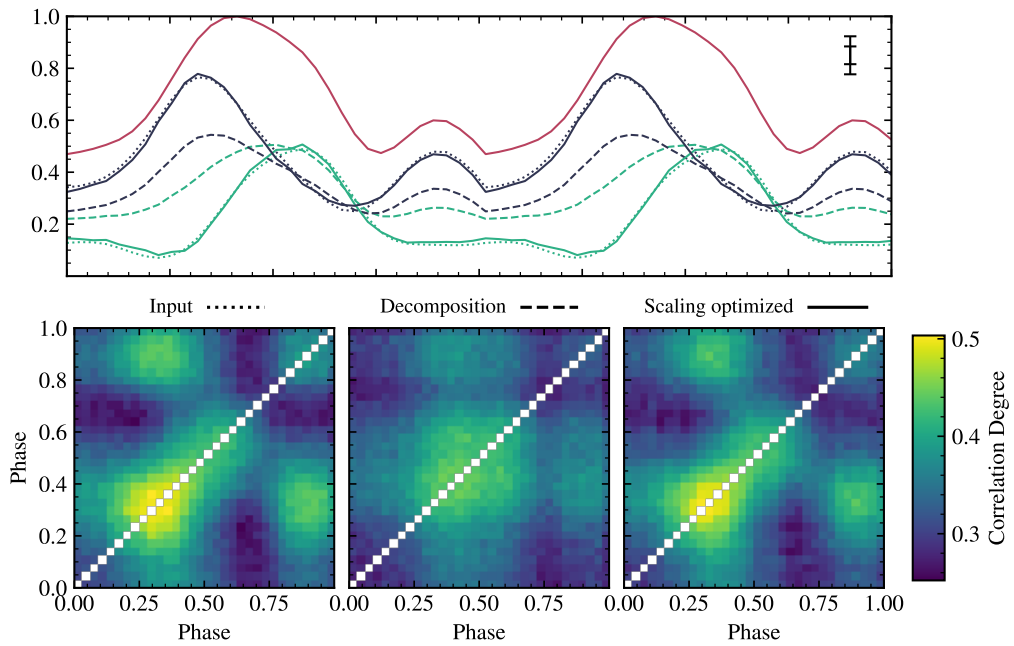
Figure 6.9: At the top is a realization of the simulated single-pole pulse profiles, shown as green and blue dashed lines. The red solid line is the sum of the two components. The initial NMF decomposition is shown as the respective dashed lines, and by comparing the phase correlation matrices (three lower panels) the scaling could be recovered, the result is shown as solid lines on top. See the accompanying text for further details.

to achieve by brute force minimization. NMF and other BSS methods are specifically designed to perform better in such scenarios. The optimization process used focuses on solving for two parameters, making it much easier to achieve.

Therefore, these are the steps for PCVA: First, the data must be prepared for analysis, meaning that pulse-to-pulse light curves must be generated in *n* phase bins, i.e., a phase pulse matrix is created. The decomposition algorithm separates the data into a signal matrix and a weight matrix. The scaling of the components must be adjusted by comparing the correlation matrices of the input and simulations based on the decompositions. Possible further steps to assess the robustness and uncertainties of the method will be explained later. In the following, PCVA is used with the outlined steps on simulated data to compare different BSS algorithms and evaluate their performance.

6.2.1 Comparison of BSS Algorithms for PCVA

The previously outlined steps necessary for PCVA are used with several blind source separation (BSS) algorithms to evaluate their performance, see Section 5.2 for an introduction. These algorithms are Principal Component Analysis (PCA, Pearson 1901), Non-Negative Matrix Factorization (NMF, Lee & Seung 1999), Fast Independent Component Analysis (fastICA, Cardoso 1998; Hyvärinen et al. 2004), and Preconditioned ICA for Real Data (Picard, Ablin et al. 2017, 2018).[4]

Using the same simulation parameters as previously defined, detailed in Table 6.1, a set of 100 weights and signals were simulated. Each simulation used a different random realization of both weights and signals to ensure that different types of weights and their combinations were covered. Consistent results were obtained across all algorithms used in the simulations, a result that is consistent with expectations given the durations and high count statistics simulated.

To provide a visual representation of the simulation results, a single realization is shown in Figure 6.10. In this figure, the smoothed sums of six randomly generated Gaussian distributions are shown as dotted lines, while the solid lines illustrate the recovered weights obtained by PCVA using each of the algorithms. It is important to note that while all algorithms successfully recover the fundamental components, the NMF algorithm outperforms the others in terms of input and recovery agreement.

In addition, the panels of the figure show the corresponding cosine similarities, which serve as a quantifiable measure of the similarity between two non-zero vectors. In our specific context, where the vectors cannot have negative values, the cosine similarity metric is bounded between 0 and 1. A value of 1 indicates that the vectors being compared

---

[4]NMF, PCA, and fastICA are implemented in Python in the Scikit-learn package (Pedregosa et al. 2011), `https://scikit-learn.org/stable/modules/decomposition.html`. For Picard see Ablin et al. (2017, 2018).
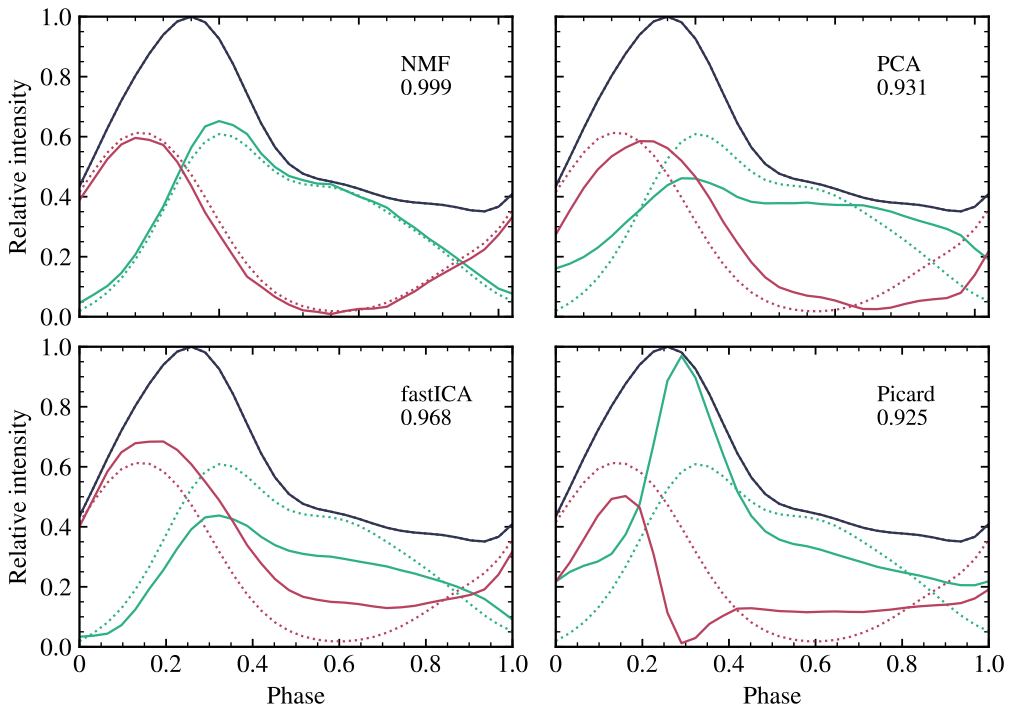
Figure 6.10: Input single-pole pulse profiles (dotted) and recovered profiles (solid) of one realization out of 100 simulations, using the NMF, PCA, fastICA, and Picard algorithms. Cosine similarity is shown for reference.

are identical. This metric allows to evaluate the recovery capabilities and the overall performance of the algorithms under investigation during the subsequent analysis.

The mean and standard deviation of the cosine similarities of all simulation results were calculated to evaluate the performance of the algorithms. The resulting analysis is shown in Figure 6.11. In general, all algorithms show the ability to recover the weights used in the simulation. However, when looking at the average similarity and the associated standard deviations, differences in their performance become apparent. With average similarity values ranging from 0.93 to 0.94 and relatively large standard deviations of about 0.04, all algorithms except NMF show a comparable level of performance. Conversely, NMF stands out as having better performance with a higher mean cosine similarity value of 0.99 and a significantly lower standard deviation of 0.02.
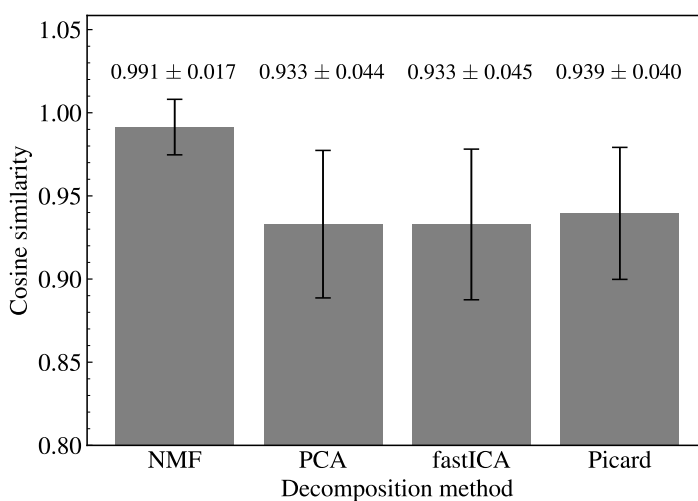
Figure 6.11: Comparison of the performance of four different algorithms for recovering simulated XRP single-pole pulse profiles. Shown are the mean cosine similarities and standard deviations for 100 simulations.

Therefore, based on the simulations, NMF is the best choice for PCVA. However, it is important to note that the results may in principle be different with different durations, count rates, pulse fraction, or other parameters. Therefore, it is important to keep in mind that NMF should not generally be used for all sources under all conditions. Instead, the choice of algorithm may need to be determined on a source-by-source basis, using simulations tailored to each source. Nevertheless, in addition to its better performance, NMF also offers better interpretability of the results, making it the best algorithm for the following analysis.

6.2.2 PCVA Requirements and Limitations

This section covers some general requirements for sources, data, and PCVA. As shown in Figure 6.8 and the corresponding text, the available data for XRPs, especially in phase-resolved form, can have low count rates and be dominated by Poisson noise. This poses a challenge for the separability of the individual components. In addition, the signals are not expected to be fully independent. In the case of the accretion disk scenario, although the accretion streams at the two poles sample opposite regions of the disk, they still originate from the same disk, implying some degree of correlation between the signals even if their phase may be shifted. Ultimately, the effectiveness of the method is limited by the counting statistics, which must be carefully considered and ensured. More specifically, I perform the PCVA using the pulse-to-pulse light curves divided into n phase bins. The determination of the appropriate number of phase bins, denoted n, depends on the resolution of the pulse profile to ensure that features of interest to the study are resolved, such as main pulses, secondary pulses, and other distinctive features. Consequently, this imposes the following requirements and constraints on the data. In cases where the light curve does not have sufficient time resolution, i.e. the time intervals are not small enough, aliasing problems can occur. Aliasing occurs when the sampling rate used to capture the signal is insufficient to accurately represent the frequency content of the signal. This results in the misrepresentation of high frequency components as lower frequencies, ultimately causing distortion and loss of important information. In our specific context, aliasing can lead to false correlation results, which can negatively affect the results of PCVA. To avoid this, it is generally recommended that the sampling frequency be at least twice the highest frequency present in the signal, known as the Nyquist frequency. However, this may not be sufficient in our case, and an empirical rule of thumb is that the light curve should have a temporal resolution equal to one third of the phase bin size. For example, consider the case of Cen X−3 with a spin period of 4.81 seconds. To sufficiently resolve the features within the pulse profile for a given study, 32 phase bins can be used. Consequently, each phase bin would be an interval of approximately 0.15 seconds. Thus, any light curve intended for PCVA must have a time resolution of 0.05 seconds or less, which is one-third of the phase bin size. It should be emphasized that the specific requirements outlined above depend on the source being studied and the corresponding number of phase bins required to resolve the features. Consequently, the selection of the instrument responsible for providing the data for PCVA must meet these requirements. See also the comments on choosing the right instrument in Chapter 4.

Once the appropriate time resolution of the light curves is confirmed, the next question is the required duration of the observation. The same simulation procedure as described above can be used to answer this question. By simulating data with varying numbers of pulse cycles, the minimum number of pulse cycles required to accurately recover the simulation input can be determined, see the top panel of Figure 6.12 for an example. The

recovery performance of the algorithms can be evaluated by comparing the reconstructed weights with the original simulation input.

The results of this analysis, performed on four different simulations, each with a different number of counts per phase bin, are shown in the middle panel of Figure 6.12. It shows the relationship between the number of pulse cycles and the quality of recovery achieved using PCVA. In particular, when considering simulations with 50-100 counts per phase bin, it becomes clear that a large number of pulses, more than 2000 in total, is required for robust PCVA recovery. This rough threshold is based on the cosine similarity metric, with values above 0.99 highlighted in the figure in gray as a reference point. For simulations with 1000 counts per phase bin, there is a relatively constant relationship in terms of the number of pulses required for accurate recovery. This suggests that once a sufficiently high count rate is achieved, achieving a reliable reconstruction becomes less sensitive to the specific number of pulse cycles.

It is important to note that the data used for PCVA does not necessarily have to come from a single observation. In scenarios where the shape of the pulse profile remains consistent and the mixing operator is unchanged, combining multiple observations becomes a possible approach to meet the required number of pulses for PCVA. This approach can be particularly interesting in situations where, for example, an average of 100 counts per phase bin is detected, but in a short observation. By combining multiple observations, the required number of pulses, over 2000, could be achieved to ensure reliable recovery of components using PCVA. However, it is important to be careful when combining observations. For this approach to be valid, the underlying assumption must be that the shape of the pulse profile and the mixing operator are constant. Any significant variation in these parameters among the combined observations could introduce biases or inconsistencies that could affect the reliability of the PCVA results. At minimum, it must be verified that the pulse profile does not change between the observations.

The performance of the PCVA as a function of the number of counts per phase bin is shown in the bottom panel of Figure 6.12. The results of simulations performed with different numbers of counts per phase bin are shown for four different observation durations. There is a strong dependence between the number of counts per phase bin and the performance of PCVA. Especially in the range below 100 counts per phase bin, there is a noticeable dependence. At these lower count rates, the data may be dominated by Poisson statistics. This can significantly affect the accuracy of PCVA in recovering the underlying components of the pulse profile. It is important to note that the average number of counts per phase bin is shown in the figure and the exact values can vary depending on factors such as the pulsed fraction and the shape of the pulse profile. Therefore, it is important to consider these factors along with the counts per phase bin when evaluating the performance of PCVA. However, the method seems to work well when the individual light curve phase bins are not dominated by Poissonian statistics.
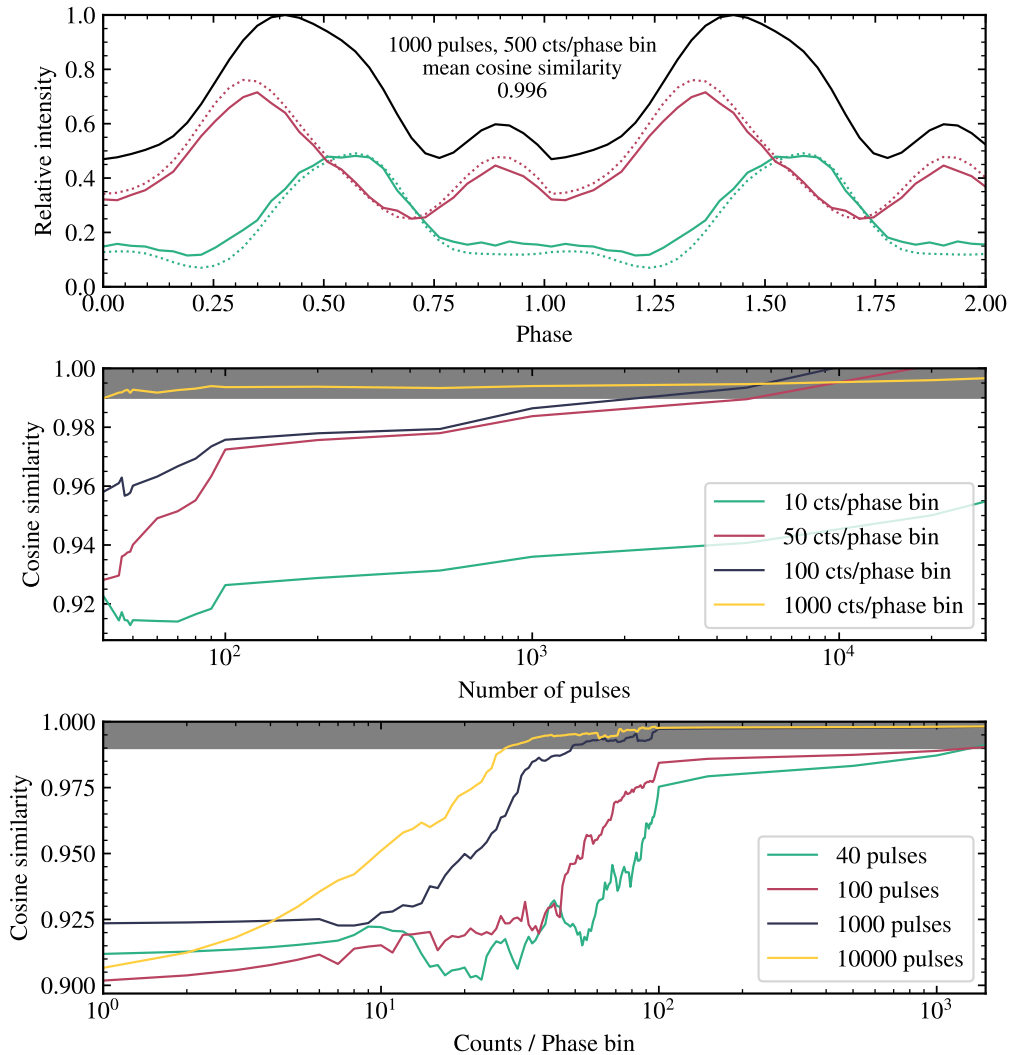
Figure 6.12: To determine the requirements for PCVA, the data was simulated in the same way as for the algorithm comparison, but with different average counts per phase bin and durations (i.e., number of pulses) for each simulation. The top figure shows an example, with the simulation input shown as dashed lines and the PCVA result shown as a solid line. The middle figure shows the performance of the PCVA as a function of the number of pulses, measured by the cosine similarity, for four different counts per phase bin. Since we are only interested in the general trends and not the final values, the data were smoothed with a Savitzy-Golay (Savgol) filter to reduce noise and improve the visibility of the general trends. The gray bar shows a cosine similarity of > 0.99. The same is true for the bottom figure, which shows performance as a function of counts per phase bin, for four different simulated numbers of pulses. More details in the text and in Figure 6.13.

We also examined the PCVA requirements, including both the number of pulses and the number of counts per phase bin. The results are shown in the matrix in Figure 6.13. This matrix provides an overview of the limitations and dependencies of PCVA performance based on different combinations of these two parameters. The matrix provides a visual representation of the relationship between the number of pulses and the number of counts per phase bin, highlighting regions of robust recovery and areas where limitations occur. In regions where both the number of pulses and the number of counts per phase bin are below certain thresholds, the performance of the PCVA is negatively affected. This is particularly evident in regions where the data is dominated by Poisson statistics, resulting in reduced accuracy in recovering the underlying components of the pulse profile. Conversely, in regions of the matrix where there are a significant number of pulses and a higher number of counts per phase bin, the performance of PCVA is robust for simulated data. In these regions, the method can accurately recover the components and provide reliable pulse profile decomposition.

By referring to the matrix shown in Figure 6.13, observations can be evaluated to see if PCVA is a potential analysis tool for certain sources. Two examples are shown in the figure; an observation of Her X$-$1 appears to provide many pulses, but with low counts per phase bin, potentially negatively affecting any PCVA, while the Cen X$-$3 observation shown provides more counts and likely a more robust PCVA. However, the matrix is only a general guide, and each observation must be examined in more detail before making a decision. It is important to note that the above estimates are, in principle, also influenced by the specific shapes of the two components. Therefore, to obtain more accurate and reliable estimates, it is necessary to perform simulations similar to those described above for each specific source. These simulations should use the initial decomposition as input to ensure consistency. Regardless, it is reasonable to expect that a robust reconstruction can only be achieved with sufficiently high photon and pulse counts. This means that the method is best suited for analyzing data from bright pulsars and instruments with large effective areas, such as NICER (Gendreau et al. 2016) and the upcoming eXTP observatory (Zhang et al. 2016).

6.2.3 PCVA Verification and Robustness Tests

To further verify the use of NMF in PCVA and to assess the overall robustness of the method, a series of tests were performed. In the first test, a data set consisting of 10000 pulses with an average count rate of 100 counts per second was simulated as described above. The PCVA was then applied to the entire data set and then it was divided into 10 segments. The purpose of this test was to determine if each of these individual parts could reliably and consistently recover the underlying components when compared to the full dataset. Based on the requirements discussed earlier (Figure 6.13), it is expected that the components will be recovered, although not necessarily fully accurately. This is consistent
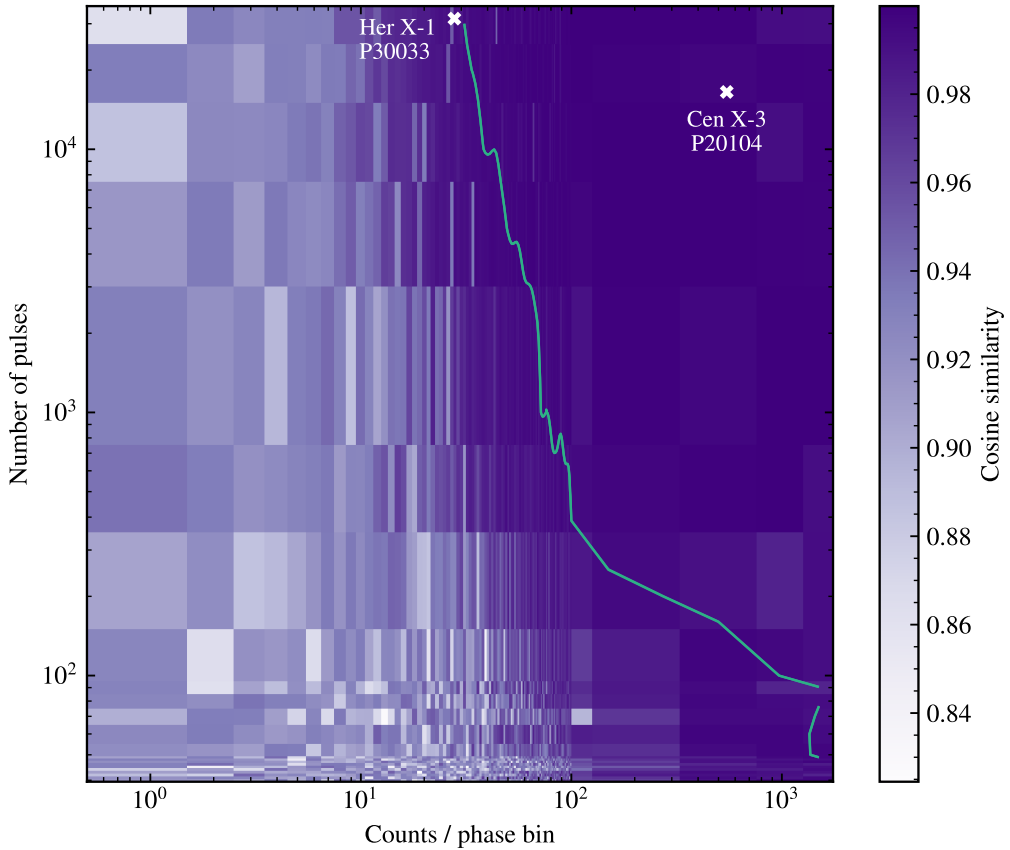
Figure 6.13: PCVA requirements as a function of number of pulses and average counts per phase bin. Cosine similarity was used as a measure of how well the input weights were recovered, see also Figure 6.12. The green line shows the contour at a cosine similarity of 0.99 and was generated after applying a Gaussian filter to the data to smooth the contour and improve the readability of the plot. The approximate data of the Her X$-$1 RXTE observation with ID P30033 is shown, with quite low counts per phase bin, as well as the Cen X$-$3 data used in this work with ID P20104, which is more suitable for PCVA. This matrix can be used to get a general idea of which sources can be analyzed with PCVA, but it should be noted that there are other factors, such as the pulsed fraction, that will influence the suitability and will need to be examined in more detail for each source.

with the results shown in the top row of Figure 6.14. The results show that the components are indeed recovered in each of the parts, confirming the robustness of PCVA. However, there is some variation, which is consistent with the expected limitations based on count rates and other factors affecting the recovery process.
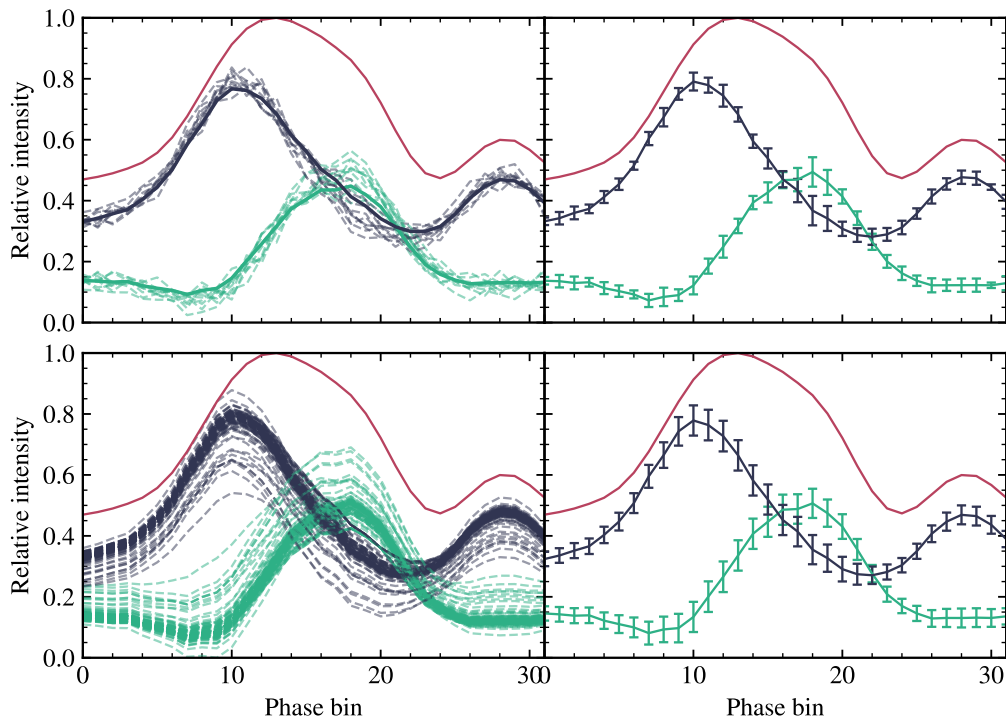
Figure 6.14: PCVA verification and consistency checks. The results in the top row show the PCVA result of a simulation with 10000 pulses and 100 counts per phase bin on average (solid line on the left) and the results after splitting the data into 10 segments (dashed lines). The right panel shows the mean and standard deviation of the results shown on the left. The bottom row shows simulation results of PCVA applied to the same data set, 100 times, and the right panel is the mean and standard deviation.

To further assess the reliability and unambiguous recovery of the input components, the simulations were repeated 100 times. This also allows an estimated quantification of the uncertainties associated with the recovered components. To quantify the reliability and estimate the uncertainty, the mean and standard deviation of the decompositions obtained from the individual simulations were calculated and compared with the input. The results are shown in the bottom panel of Figure 6.14, which shows the reconstruction of the contributions from both poles. The left panel shows the individual recovered components,

while the right panel shows the corresponding mean profiles and standard deviations as uncertainties. The results show that the contributions from both poles are indeed robustly reconstructed with relatively small uncertainties, provided that the required counts and number of pulses are satisfied.

Since NMF is an iterative method that is not guaranteed to converge, the effects of different convergence criteria and optimization starting points were analyzed and evaluated. The aim is to determine whether the conclusions drawn from PCVA could be invalidated by adjusting these factors. For this purpose, the NMF algorithm was initialized with different weights as starting points for the optimization. The results were then compared to the mean decomposition obtained from the previous set of 100 simulations. Specifically, three different scenarios were explored:

1. Initialization with a constant weight: The method was initialized with weights such that one weight remained constant, while the other weight was set to ensure that the initial pulse profile, i.e. the sum of the two initial weights, remained unchanged. This process was repeated for three different constant values, shown as dashed lines in each of the three columns of the top row of Figure 6.15. Each scenario was analyzed with 10 simulations, and the mean decomposition was calculated and shown as solid lines. In all three cases, the results converged to the expected solution corresponding to the original input (shown as dotted lines).

2. Initialization with shifted weights: Another set of initializations involved shifting one of the original weights by a certain number of phase bins. The second weight was adjusted to keep the overall pulse profile unchanged. The results of this analysis are shown in the middle row of Figure 6.15. Again, 10 simulations were performed and only the mean decomposition is shown. As in the previous case, shifting the weights did not significantly affect the results, and the PCVA consistently converged back to the expected solution.

3. Initialization with scaled weights: The third set of initializations involved scaling one of the components, while the other was chosen to leave the profile unchanged. Similar to the previous cases, 10 simulations were performed, and only the mean decomposition is shown in the bottom row of Figure 6.15. Once again, the scaling of the weights did not lead to significant deviations, and the PCVA method consistently converged to the expected results.

The consistency of these results strongly suggests that the PCVA method reliably and consistently recovers the underlying weights regardless of the specific initialization.
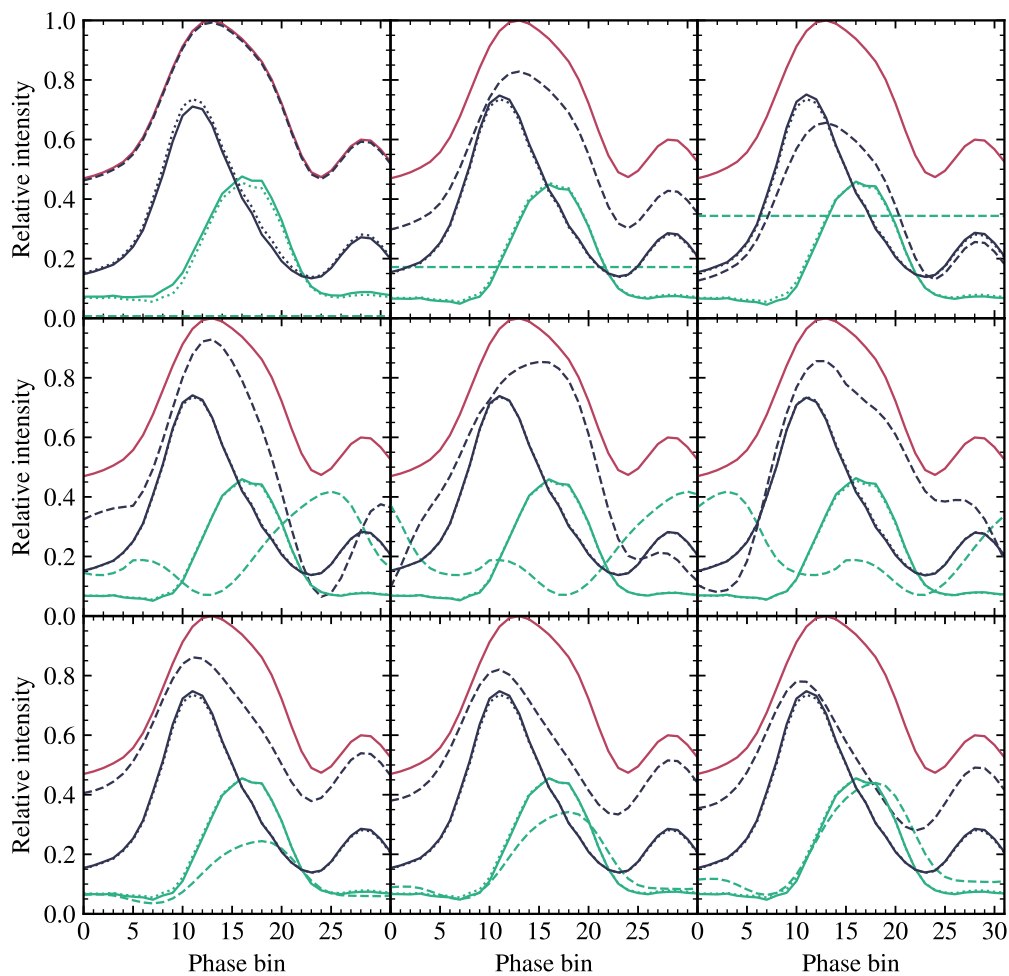
Figure 6.15: The results of different initializations for the NMF decomposition as part of the PCVA were analyzed for consistency. Dotted lines are the results with random initialization, dashed lines are the initialized weight matrix, and solid lines are the final decomposition result. The top row shows results for initializations where one weight is held constant, the middle row shows simulations where one weight is shifted in phase, and the bottom row shows differently scaled weights. In all cases, the results converge to the expected solution.

Application to Cen X–3
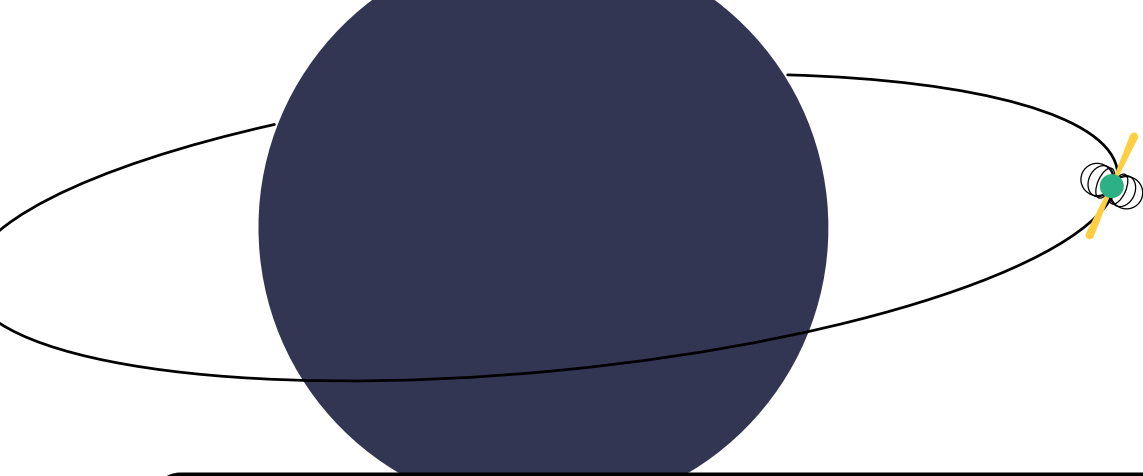
7. Pulse Profile Decomposition of Cen X−3

In this chapter I discuss the application of phase correlated variability analysis (PCVA) to Cen X−3 - the first X-ray pulsar ever discovered. Due to its high luminosity and extensive observational history by several satellites, Cen X−3 is a prime candidate for the application of PCVA. Another advantage is that there is already a decomposition of this source published by Kraus et al. (1996), which gives an independent reference for our results. First, I present a literature review of the system with an emphasis on the pulse profiles of Cen X−3 in Section 7.1. Then I present and discuss the PCVA results in Section 7.2.

7.1 The Cen X−3 System

The following Section 7.1.1 introduces the Cen X−3 system with some general characteristics and properties to put the system in context. This is followed by an overview of the main features of the Cen X−3 pulse profile in Section 7.1.2 with a brief review of previous attempts to model and decompose Cen X−3 pulse profiles. This provides a point of reference and helps to put the subsequent PCVA results into context.

7.1.1 Physical Properties of the Cen X−3 System

Cen X−3, sketched in Figure 7.1, is a high-mass X-ray binary system first observed in 1967 by Chodil et al. (1967) and is the very first X-ray pulsar ever detected, as reported by Giacconi et al. (1971a). The binary system consists of a neutron star rotating with a spin period of about 4.8 seconds orbiting an O-type supergiant companion star (Schreier et al. 1972; Krzeminski 1974). Cen X−3 is a persistently accreting X-ray binary (XRB). The observed X-ray flux is highly variable, which has been interpreted by Paul et al. (2005) as evidence for the presence of multiple accretion modes within the system. However, the
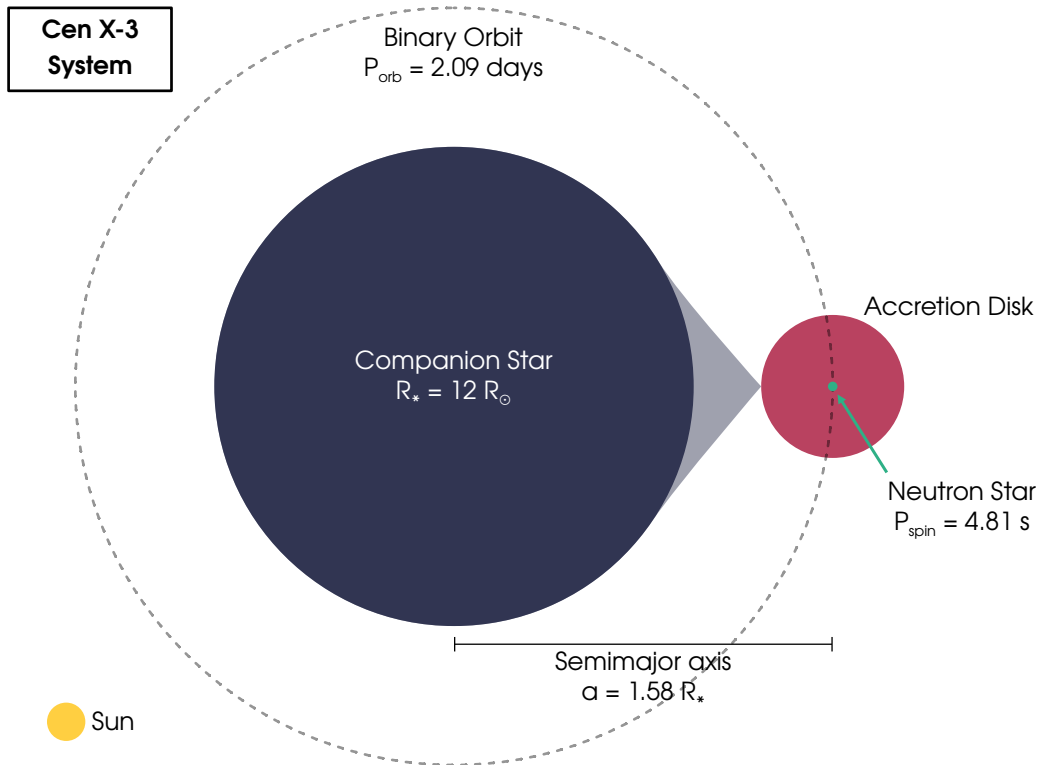
Figure 7.1: Pole-on sketch of the Cen X−3 system. The donor star radius, binary orbit, and accretion disk are roughly to scale. The image is modified from Sanjurjo-Ferrín et al. (2021). The real inclination of the system is about 70° (Ash et al. 1999), so it is actually observed almost edge-on.

exact nature and origin of the observed variability in Cen X−3 is not fully understood. Müller et al. (2011) were unable to confirm the reported spectral changes associated with the different accretion modes. However, it should be noted that for the purposes of this thesis we only use observations of Cen X−3 obtained during a bright state, as described in detail below. It is worth noting that even during this bright state, the pulsar in Cen X−3 is likely to be accreting below the critical luminosity (Tsygankov et al. 2022). Consequently, it is likely that there is no extended accretion column and that the emission comes from confined emission regions on the surface of the neutron star, which is relevant for the modeling presented in Section 7.2.2.

7.1.2 Pulse Profiles of Cen X−3

The pulse profile of Cen X−3 is constant in shape and time, as reported in Raichur & Paul (2010), and shows a structure composed of two distinct peaks during the bright state. The larger peak is commonly referred to as the primary peak, while the smaller one is referred to as the secondary peak. The primary peak rises sharply and declines more gradually, ending in a shoulder, the secondary peak. It is worth noting that the pulse profile of Cen X−3 shows variations in energy, see Figure 7.2. Specifically, the primary peak remains relatively constant over the energy range of 1−40 keV, while the secondary peak diminishes at higher energies, above about 20 keV. In addition to the energy variation, there are subtle variations in the pulse profile associated with the orbital phase (Raichur & Paul 2010). However, for the purposes of this work, these variations are considered to be of negligible relevance and are therefore not considered in further analysis.

To gain further insight into the pulse profile of Cen X−3, numerous studies and analyses have been conducted to understand its geometry and intrinsic beam pattern. Some of these studies are reviewed below, with particular emphasis on the decomposition analysis performed by Kraus et al. (1996). Wang & Welter (1981) approached the problem by phenomenologically parameterizing an asymmetric beam pattern. With this beam pattern, it was possible to reproduce the single peak pulse profile that was observed at low energies between 2 and 7 keV. A different approach was taken by Leahy (1991). They proposed a model that included polar emission regions in the form of rings or caps, see their geometry in Figure 7.3. These emission regions were allowed to be offset from the strictly antipodal positions on the surface of the neutron star. By allowing such offsets, the model reproduced the single peak pulse profile at intermediate energies, from 12.5 to 25 keV, reasonably well. The model assumes axisymmetric emission regions, and the asymmetry that is observed in the pulse profile is explained by an offset of the dipole. The polar cap model proposed by Leahy (1991) was further developed and refined by Riffert et al. (1993). They incorporated the effect of gravitational light bending into the model, which led to adjustments in the ring sizes and offsets to account for the observed pulse profiles of Cen X−3. By accounting for gravitational light bending, Riffert et al. (1993) found that smaller ring sizes and offsets
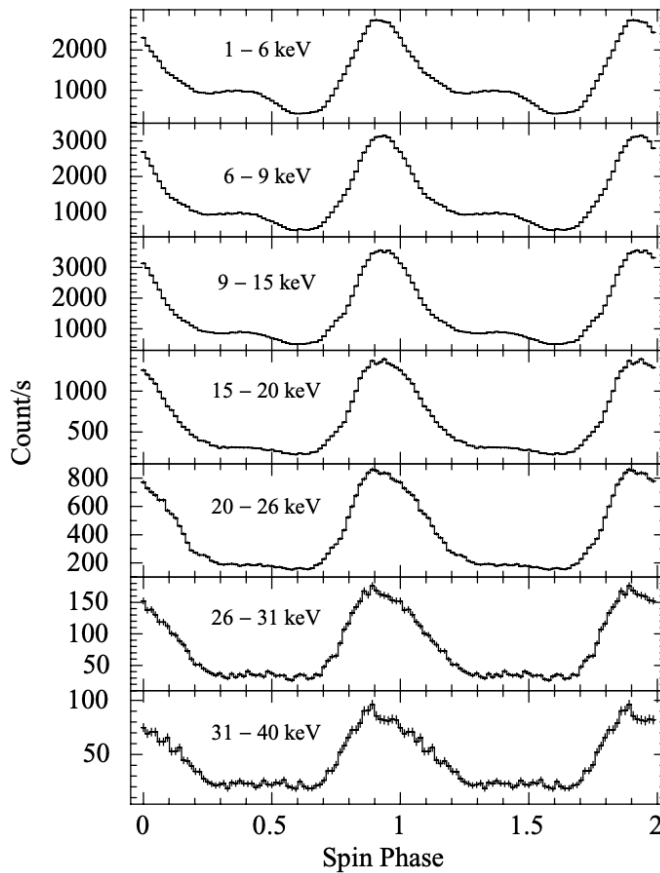
Figure 7.2: The energy dependence of the averaged Cen X−3 pulse profiles shows a constant primary peak. However, the secondary peak disappears at higher energies, above about 20 keV. The figure is taken from Raichur & Paul (2010).
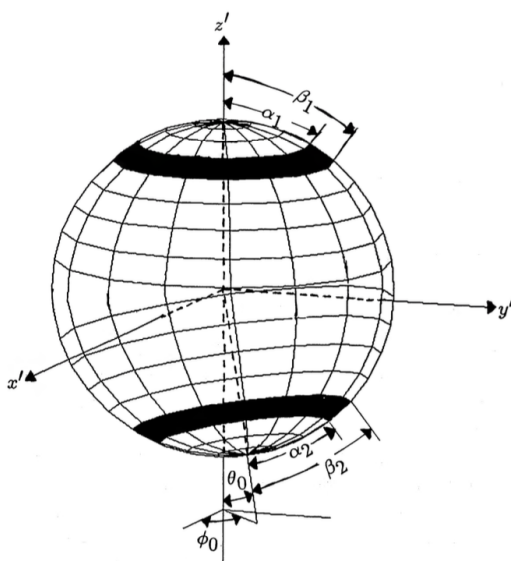
Figure 7.3: The polar cap emission model consists of two annular polar cap emission regions centered on the magnetic poles, offset from a strict dipole. The figure is taken from Leahy (1991).

were needed to reproduce the observed pulse profiles. The pulse profile of Cen X−3 and the resulting model based on the modified polar cap model of Riffert et al. (1993) are shown in Figure 7.4. The displaced dipole model, where the polar caps are not antipodal, has been applied in various studies to many sources, providing insights into the emission geometry and magnetic field configuration. In these models, the magnetic axis is either off-center or the magnetic field contains a significant non-dipole component. Evidence for the unequal and non-antipodal nature of the polar caps has been found for example in (Parmar et al. 1989; Bulik et al. 1992, 1995).

Kraus et al. (1995) developed a pulse profile decomposition analysis, introduced in Section 3.2.3, also based on the displaced dipole model, which was applied to Cen X−3 in their subsequent work (Kraus et al. 1996). Their method aimed to separate the contributions of different emission components and to provide a quantitative characterization of the pulse profile. The results of the pulse profile decomposition analysis of Kraus et al. (1996) for Cen X−3 can be seen in Figure 7.5 as an example. The example shows the decomposition of the pulse profile into different emission components coming from different regions of the neutron star.

Although the observations used by Kraus et al. (1996) differ from the data analyzed in this thesis, it is important to note that the stability of the observed pulse profile shapes suggests that any differences between the data sets are unlikely to significantly affect our
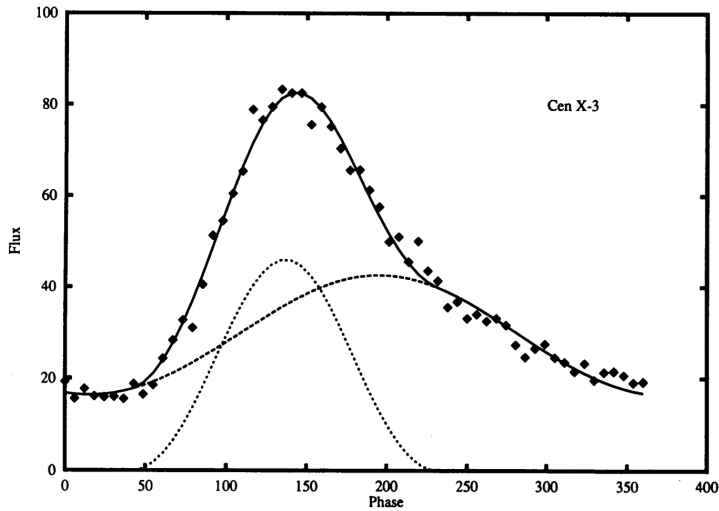
Figure 7.4: The polar cap emission model of Leahy (1991) has been modified by Riffert et al. (1993) to include relativistic light bending. This Cen X−3 pulse profile was fitted using two polar caps with opening angles of 10°. The two individual contributions of the polar caps are shown as dashed curves. The figure is taken from Riffert et al. (1993).

results. Consequently, the results reported by Kraus et al. (1996) serve as a baseline for our subsequent analysis.

In order to be able to directly compare the results of Kraus et al. (1996) with ours, I have applied their method (see Section 3.2.3 for a short overview and Kraus et al. (1995, 1996); Caballero et al. (2011); Sasaki et al. (2012) for detailed descriptions) to our RXTE observation of Cen X−3. The pulse profile of this observation appears similar to the O2 observation shown in Figure 7.5. Its symmetry point Φ_1 roughly coincides with the maximum of the pulse profile. I therefore determined Φ_1 to correspond to the maximum of the pulse profile of the RXTE observation, which is at about 213.75°. Together with their reported Δ angle for the O2 observation, 32.13°, the decomposition I obtained is shown in Figure 7.6. The result is consistent with that shown in Figure 7.5. In the following, I compare the PCVA results with this decomposition.

7.2 PCVA Decomposition Results of Cen X−3

Cen X−3, being the first X-ray pulsar known, has been extensively observed with various instruments. However, for the purpose of applying the phase correlated variability analysis (PCVA), a sufficiently high counting statistic is required, as seen in Section 6.2.2. Therefore, in this thesis we use an observation of Cen X−3 obtained with the Rossi X-ray Timing
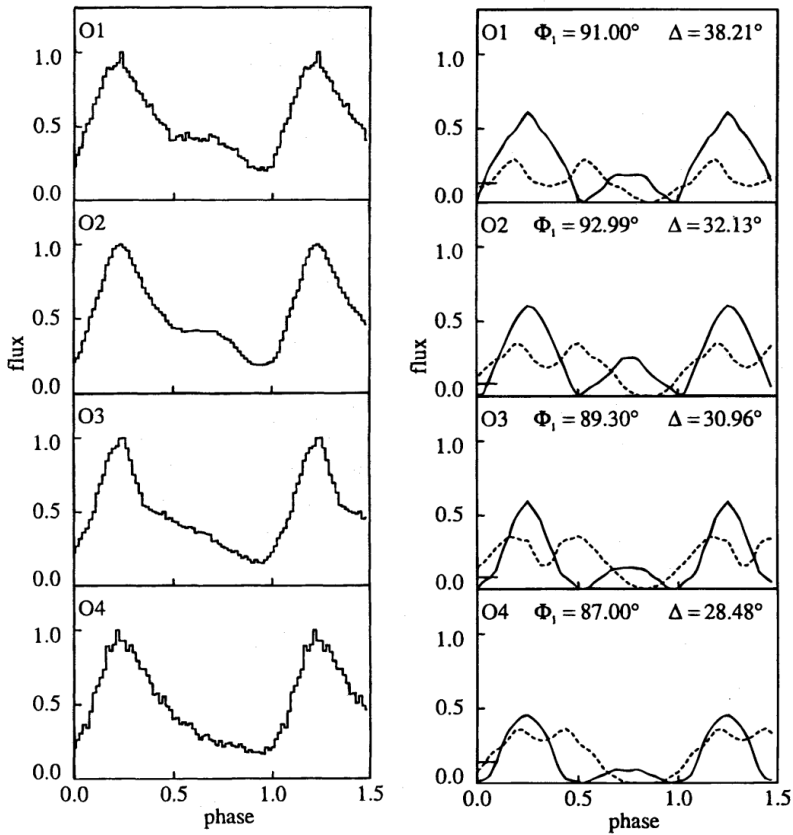
Figure 7.5: Pulse profiles of Cen X−3 observed with the OSO 8 satellite (left), from top to bottom in increasing energies. On the right are the corresponding symmetrically decomposed single-pole pulse profiles, obtained with the Kraus et al. (1995) method. The figure is combined from figures 1 and 3 in Kraus et al. (1996).
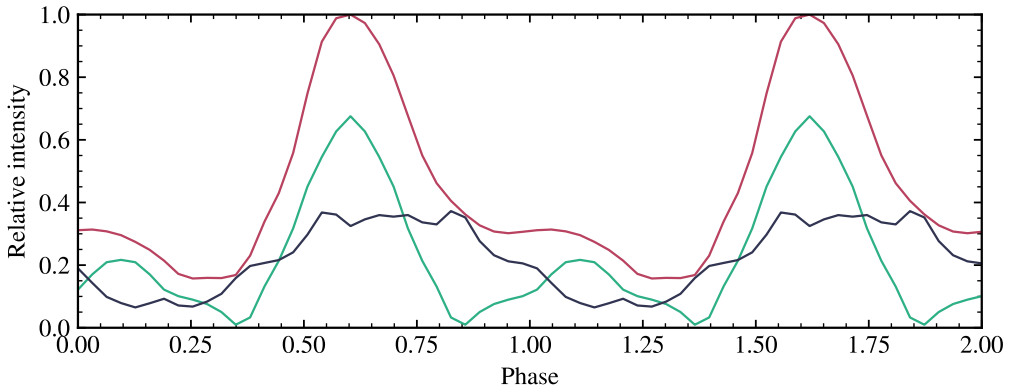
Figure 7.6: Pulse profile decomposition of the RXTE observation of Cen X−3 with ID 20104-01-01-00 using the Kraus et al. (1995) method and the angles $\Phi_1 = 213.75°$ and $\Delta = 32.13°$ as defined in Kraus et al. (1996). The decomposition is consistent with the results reported in Kraus et al. (1996) and presented in Figure 7.5. Note that the two components (green and blue) are symmetric in phase, as required by the method, and remarkably different from each other.

Explorer (RXTE, see Section 4.2 and Bradt et al. 1993) between February 28 and March 1, 1997, which corresponds to the Modified Julian Date (MJD) range of 50507-50508. These observations were made during the high accretion state of the source and cover a significant part of the pulsar's orbit. During this observation a total exposure time of 97 kiloseconds (ks) was achieved in the observation with observation ID 20104-01-01-00. All five proportional counters of the RXTE were operational during most of the observation. The data were extracted for channels 10−35, corresponding to an energy range of about 4−13 keV, which covers the energies where most of the source photons are detected. In addition, this energy range was chosen because there is no significant variation in the shape of the pulse profile (Klawin et al. 2023).

As discussed in Section 6.2.2, the time resolution needed for the PCVA depends on the source and the number of phase bins required. In the following analysis, 32 phase bins should sufficiently resolve the features, i.e. the two peaks of the pulse profile. The time resolution of the data is set to 2^{-5} seconds, which is small enough to perform PCVA. The spin period of the pulsar during this specific RXTE observation is about 4.81426042 seconds, as determined by Klawin et al. (2023). During the observation a visible dip was observed towards the end of the observation period. This is related to absorption in the companion's atmosphere. Therefore, only data recorded before MJD 50508.38 were included in our analysis, see Figure 7.7. This selection ensures that the data considered for the subsequent PCVA are free from the influence of variable absorption. The phase pulse
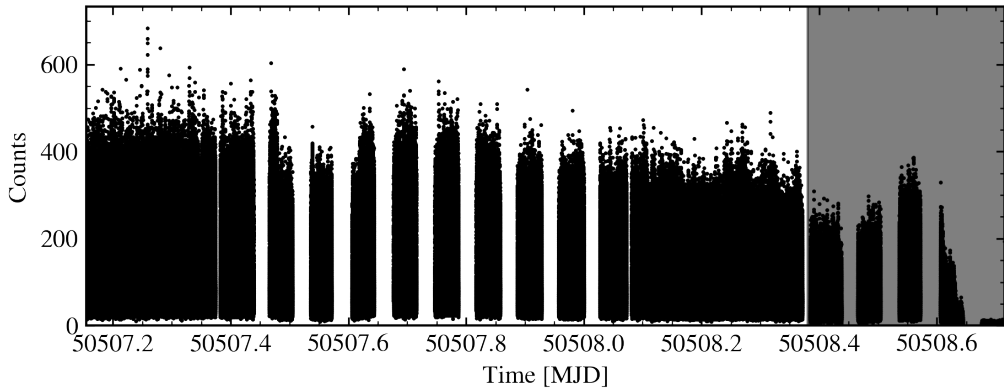
Figure 7.7: The complete light curve of the RXTE Cen X−3 observation with ID 20104-01-01-00. Since there is a dip at the end associated with absorption in the companion's atmosphere, only data before MJD 50508.38 were used for the analysis, the gray part after this date was discarded.

matrix of this observation is shown in Figure 7.8.

The PCVA method was applied to analyze the RXTE data from Cen X−3, using the same procedures used to analyze the simulated data in the previous chapter. The results of this analysis are shown in Figure 7.9, where the average of 100 decompositions of the two single-pole pulse profiles are plotted. In the upper right corner of the upper panel are the estimated uncertainties based on the minimum and maximum standard deviations of the simulation results. The primary peak of the overall pulse profile consists of a combination of two distinct single-pole components. When one component is reflected in phase and then aligned in phase, both components appear qualitatively similar, as shown in the middle panel of Figure 7.9. The secondary peak appears to result from contributions from both single-pole components. The separation between the two maxima is measured to be 0.125 in phase (corresponding to 45 degrees), while the separation between the two minima is 0.25 in phase (corresponding to 90 degrees). The minimum and maximum separation for each individual component is 0.1875 in phase, corresponding to an angle of 67.5 degrees, also shown in Figure 7.9, in the lower panel. In Figure 7.10 the results of the PCVA decomposition can be compared with the decomposition obtained by the method proposed by Kraus et al. (1996), which will be studied in detail below.

7.2.1 Comparison with the Kraus et al. 1996 Results

There are several notable differences when comparing the PCVA decomposition with the decomposition obtained by the method proposed by Kraus et al. (1995). First, the individual components obtained by PCVA are qualitatively similar, while the Kraus et al. (1996)
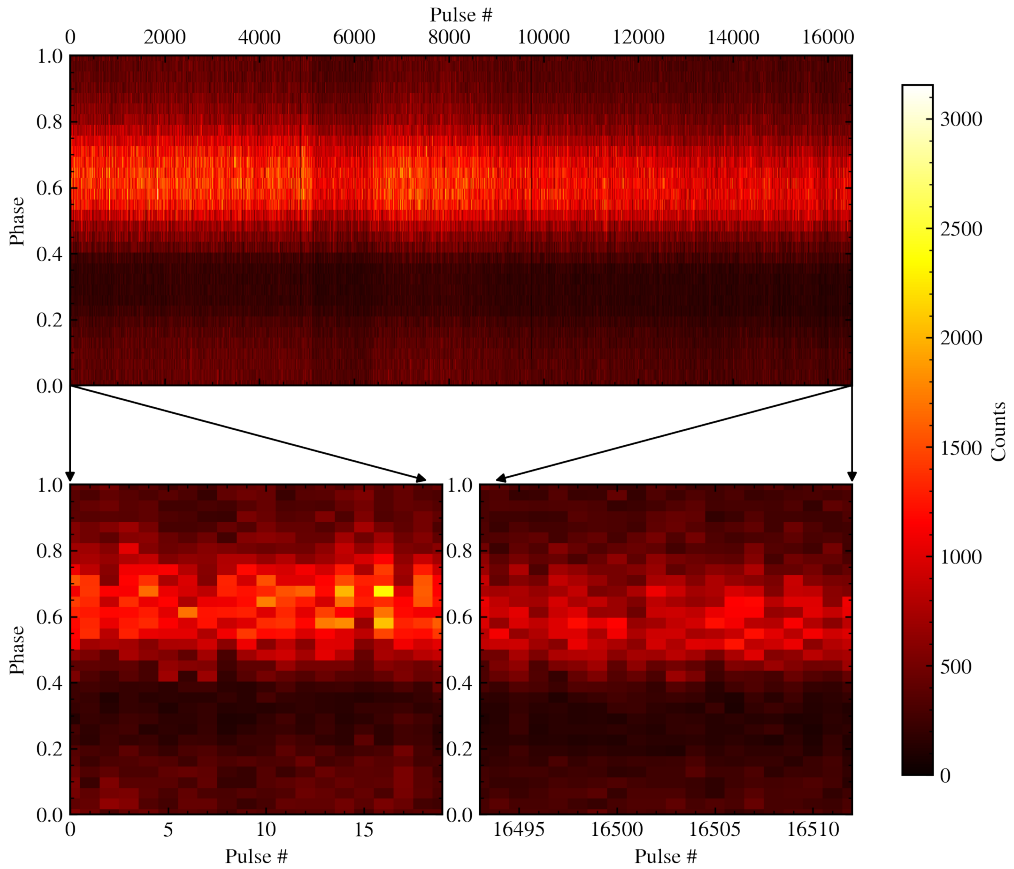
Figure 7.8: Cen X−3 phase pulse matrix of the RXTE observation with observation ID 20104-01-01-00. The top panel shows the entire data set analyzed, with over 16500 pulses. The lower panels show the first and last twenty pulses to better visualize the pulse-to-pulse variability.
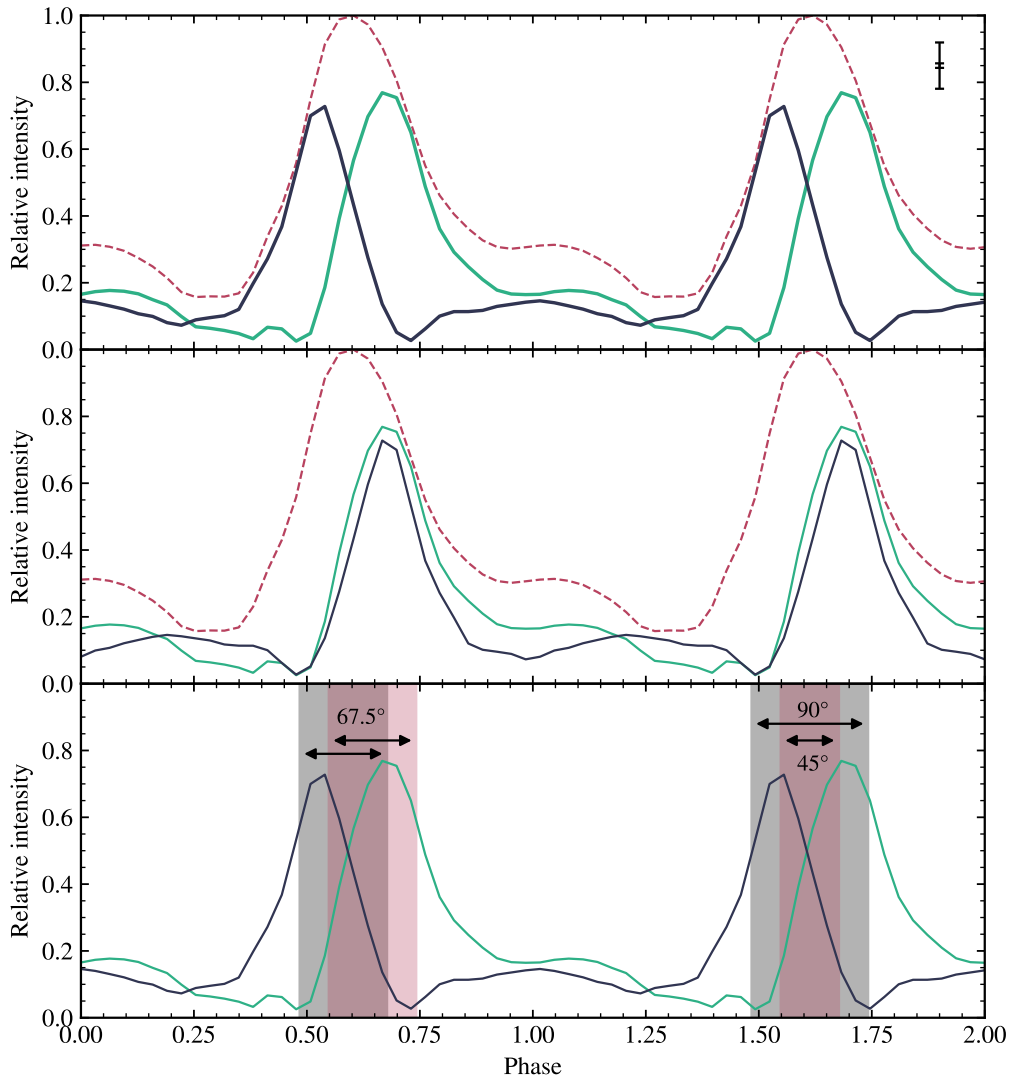
Figure 7.9: The PCVA decomposition of Cen X−3 is shown in the top panel in green and blue, with the total average pulse profile of the observation as the dashed red line. When one component is reflected in phase, the two components appear qualitatively very similar, as shown in the middle panel, where the blue component has been reflected in phase and shifted by seven phase bins. The lower panel shows the angles between the minima and maxima of each component, which are 67.5° for both, as well as between the two components, 90° from minimum to minimum and 45° from maximum to maximum.

method yields significantly different components. However, the most significant difference lies in the phase asymmetry of the components derived from the PCVA decomposition.

To verify that the Kraus et al. (1995, 1996) results could still be compatible with the observed aperiodic variability properties, I tried to use their results as input for the simulation of a phase-resolved light curve, as described in Section 6.2. The resulting correlation matrix, as shown in the middle panel of Figure 7.10, shows a distinct pattern that differs significantly from the observed correlation matrix. This simple test, that is independent of any assumptions associated with the PCVA methodology, highlights potential inconsistencies between the two approaches and raises questions about the validity of the assumptions underlying the Kraus et al. (1995, 1996) decomposition method. The discrepancy between the phase correlation matrix of simulated data using the Kraus et al. (1995, 1996) decomposition and the observed phase correlation matrix mentioned above implies an inherent inconsistency between the decomposition result and the observed correlation properties. This inconsistency is evident even when considering the limitations associated with the simulations. The differences in the phase correlation matrices indicate that the expected changes in different parts of the pulse profile do not match what is observed.

To ensure the reliability and robustness of the PCVA results, several tests are conducted to evaluate its stability and consistency. These tests are similar to the simulation verification and robustness tests performed in Section 6.2. First, by adjusting the initializations for the optimization process, it was evaluated if this could affect the results and conclusions of the PCVA. Specifically, we generated new phase-resolved light curves using the decomposition result obtained with PCVA as the basis, rather than random weights. We then re-decomposed these simulated data. In the first test, the decomposition of Kraus et al. (1995, 1996) was used as the starting point for the optimization, instead of random values. The weight matrix for the second initialization test was created by symmetrizing the PCVA results. In addition, the effect of initializing the method with the broad components determined by Riffert et al. (1993) was examined. The results for these three initializations can be found in Figure 7.11, and in all cases the decomposition converged to the expected results, reinforcing the confidence that these are the true components.

To ensure the stability of the decomposition, we also ran the analysis separately for multiple (10) segments of the observation, see the lower right panel of Figure 7.11. Again, the PCVA yielded the same expected solution, consistent with the results shown in Figure 7.9. These results, which are consistent regardless of the specific details of the analysis, further demonstrate the robustness of the PCVA results. All of the above validation checks and observations of the phase correlation lead to the conclusion that the PCVA decomposition is robust and therefore there is a real discrepancy with the Kraus et al. (1996) result. This challenges the main assumption of the decomposition method proposed by Kraus et al. (1995, 1996), which assumes a symmetrical emission characteristic at
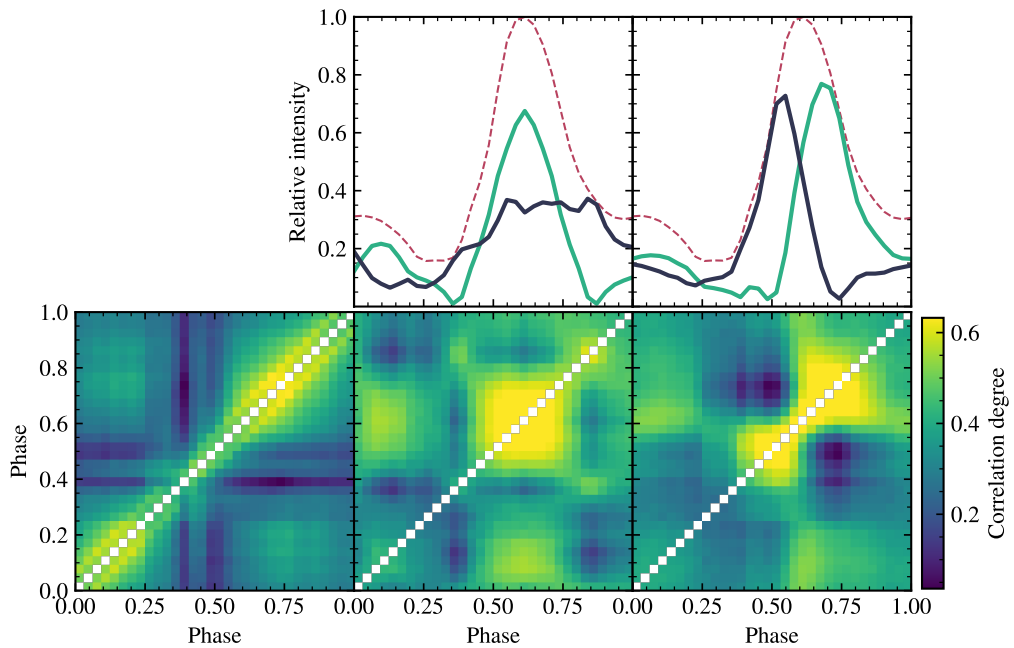
Figure 7.10: Comparison of the correlation properties of different data sets. The left panel shows the phase correlation matrix of the Cen X−3 observation. The middle panel shows the decomposition of Kraus et al. (1996) on top and the phase correlation matrix of a simulation with these components as input below. The right panel shows the same for the PCVA decomposition.
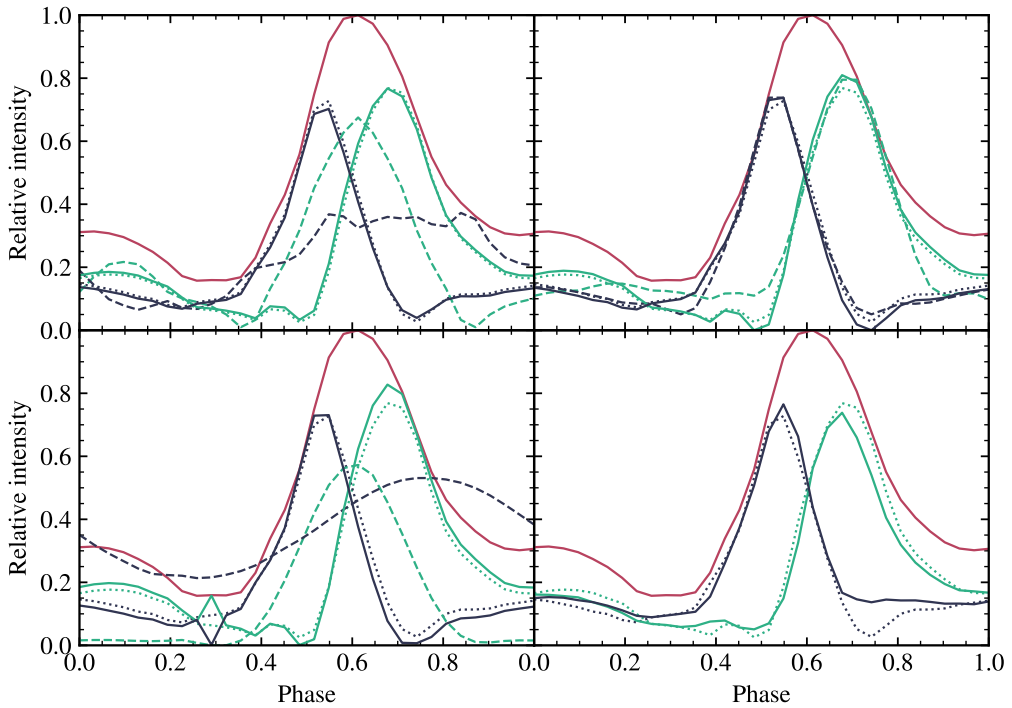
Figure 7.11: PCVA of Cen X−3 with different initializations. In all panels, the averaged PCVA decomposition is shown as dashed lines and the total pulse profile is shown as a red solid line. The dashed lines indicate the different initializations. In the upper left panel, the initialization of the NMF decomposition was set to the Kraus et al. (1996) (Figure 7.9) decomposition. The upper right panel shows a symmetrized version of the PCVA result as the starting point for the optimization, for the lower left panel it is approximately the decomposition of Riffert et al. (1993) (Figure 7.4). All panels show the average of 10 simulations. The bottom right panel shows the average result of the PCVA when the observation is split into 10 segments. All results are shown as solid lines, and in all cases the method converges to the expected result.

the two poles. The asymmetry in the PCVA results suggests the presence of inherent complexities within the emission mechanisms of Cen X−3 that cannot be adequately captured by the assumptions made in the Kraus et al. (1995, 1996) method.

7.2.2 Interpretation of the PCVA Results

The analysis and PCVA results described above lead to several conclusions regarding the emission from each neutron star pole. First, the observed emission pattern from each of the two poles is inherently asymmetric in phase. This suggests that the intrinsic beam pattern localized within the emission region is also asymmetric. Second, despite the phase reflection between the two poles, the contributions from the two poles are remarkably similar. To understand why this is the case and what it means in the context of pulse profile formation, a simplified model has been created and is described below. The goal of this modeling was to reconstruct the intrinsic beam patterns at each of the locations in the emission region. Considering the discussions presented by Kraus et al. (1995, 1996), it should be noted that the asymmetry observed in the pulse profile generated at a single pole implies the presence of an asymmetric intrinsic beam pattern. This asymmetry can arise, for example, if the magnetic field defining the opacities is not orthogonal to the photosphere of the emission region on the surface of the neutron star, but is at a small angle, see the discussion in Section 3.2.3. In fact, it can result from any asymmetry in the local emission from the photosphere in combination with a complex geometry. Consequently, the local beam pattern around the emission region may be symmetric about a particular direction, but asymmetric with respect to the normal vector. Ultimately, the beam pattern may not be symmetric at all, but we consider this included symmetry to be a next order approximation and simplification. With the rotation of the neutron star, this intrinsic asymmetry can give rise to asymmetric pulses.

To model this, the geometry of the pulsar is defined as follows. First, the orientation of the spin axis of the neutron star and the location of the emission region on its surface are defined. The upper left panel of Figure 7.12 shows the position of the spin axis, which is determined by the tilt and position angle of the pulsar's spin. The middle panel of Figure 7.12 shows the position of the emission region, which is characterized by the magnetic co-latitude and the rotational phase around the spin axis. In our toy model, the emission is generated by a single emission region at each pole. The emission pattern of each emission region is symmetric about an axis different from the normal. To define the direction of this axis, two additional angles, α and φ, must be defined. These angles are shown in the right panel of Figure 7.12. To express these angles in Cartesian coordinates, we use the x and y axes as shown in the figure. Note that in the unit sphere, the projection of the angle α on the $x - y$ plane is equal to the distance r from the origin. With these definitions, the beam pattern can be expressed in terms of α and φ as follows:
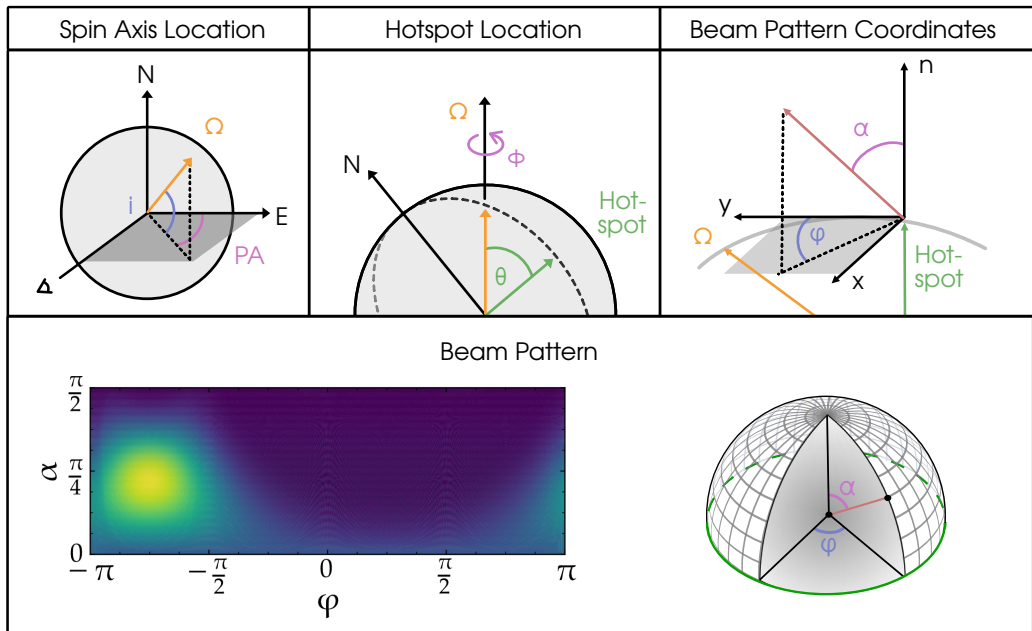
Figure 7.12: For the toy model, the pulsar geometry and the beam pattern are defined by the following angles. In the upper left panel is the spin axis (Ω) at the location of the inclination (i) and the position angle of the pulsar spin (PA). To its right, in the middle panel, the position of the emission region on the surface with respect to the spin axis is defined by the magnetic co-latitude (θ) and the rotation phase is denoted by Φ. The upper right panel shows the angles α and φ that define the emission pattern. α is measured from the normal to the surface and the reference for φ is the y axis, which in turn points to the spin axis. The lower panel shows an example of a simple asymmetric beam pattern and a sketch of the angles in the unit sphere.

$$\alpha = \arcsin(r), \text{ with } r = \sqrt{x^2 + y^2}$$
$$\varphi = \arctan\left(\frac{y}{x}\right).$$

To parameterize the local beam pattern, I use a two-dimensional cosine function with the $x - y$ coordinates:

$$f(x_1, y_1, \delta x_1, \delta y_1, \kappa_1, \kappa_2, x_2, y_2, \gamma) =$$
$$\left[\cos(x_1 + \delta x_1)\cos(y_1 + \delta y_1)\right]^{\gamma} + (\kappa_1 \cos(x_2)) + (\kappa_2 \cos(y_2)).$$

Here, x_1, x_2 and y_1, y_2 represent points in the $x - y$ plane, as shown in Figure 7.12, and can each take values between $-\pi/2$ and $\pi/2$. The cosine function can be shifted in the x and y directions by the values δx_1 and δy_1, respectively, with values between $-\pi$ and π. The parameters κ_1 and κ_2 determine the strength of the additive cosines, introducing additional asymmetries. Raising the function to the power of γ allows to adjust the width or "peakiness" of the beam pattern. An example of such a beam pattern, transformed back to the α, φ coordinate system, is shown in the bottom panel of Figure 7.12. This representation of the beam pattern, although arbitrary, provides a simple and flexible way to explore the characteristics of the local beam pattern, allowing us to study a wide variety of scenarios and investigate the effects of different parameters on the profiles.

In our model, we also account for the effects of gravitational light bending using the analytical approximation given by Beloborodov (2002) (see also Figure 3.8):

$$1 - \cos\alpha_{\text{em}} = (1 - \cos\psi)\left(1 - \frac{r_g}{R}\right).$$

Here, α_{em} is the angle at which a photon is emitted with respect to the radial direction, and ψ is the angle at which the emission of the photon is observed. The term r_g is the Schwarzschild radius, and R corresponds to the radius of a neutron star, which is about 3 times the Schwarzschild radius ($R \approx 3r_g$). This allows for a more accurate description of the emission properties, taking into account the effects of strong gravitational fields in the vicinity of the neutron star.

It is important to note that the parameterization outlined above serves as a simplified phenomenological function, intended to allow the study of symmetric and asymmetric local emission patterns, as well as the effect of various parameters on the visibility of the emission regions. The aim is to illustrate that asymmetric pulse profiles *can* be described by introducing even minimal deviations from symmetric local beam patterns. Furthermore, it is important to recognize that the actual beam pattern of the emission regions remains largely unknown and is unlikely to be strictly symmetrical. Therefore,

the presented parameterization is a tool for exploring and understanding the effects of asymmetry, but should not be considered as an accurate representation of the true beam pattern characteristics. Nevertheless, it remains valuable for studying the behavior of the observed emission and for exploring the implications of asymmetric contributions. This approach allows us to improve our understanding of the underlying physical processes involved in pulsar emission, even in the absence of detailed knowledge of the exact beam pattern.

By defining arbitrary geometries and beam patterns, the model can be used to test the effects of various parameters on the observed pulse profiles. Symmetric beam patterns, as shown in the upper part of Figure 7.13, produce symmetric pulse profiles. Each panel in the figure represents a separate and independent example, with the corresponding parameters outlined in Table 7.1 and Figures 7.13-7.15. The top left and top right panels of the figure show the geometry illustrating the rotational motion of the hotspot around the spin axis. Below each geometry is the corresponding beam pattern for that emission region. The visible regions of the beam pattern, observable to a distant observer positioned at infinity (at infinity perpendicular to the figure plane), are traced with lines. Note that here the emission region is assumed to be a point on the surface of the star. The resulting pulse profiles, shown in the larger central panel, are drawn in the same style as the lines used to represent the visible regions of the beam pattern. Symmetric intrinsic beam patterns produce symmetric pulse profiles. The lower part of the figure, analogous to the upper part, shows the effect of different asymmetric intrinsic beam patterns. This results in asymmetric single-pole pulse profiles, as expected.

In addition, I have studied the visibility of emission regions taking into account gravitational light bending. Specifically, I examined perfectly antipodal dipole emission regions under different geometries. An example of this is shown in the upper part of Figure 7.14. Unlike the previous figure, which explored completely independent geometries, this scenario is constrained to an antipodal geometry. As shown in this example, if one pole remains visible for most of the rotation period, the other pole will be mostly invisible during the same period. It is important to note that this visibility aspect is independent of the intrinsic beam pattern and depends primarily on the visibility of the emission region itself. In the example, the same beam pattern is used for both cases, and the overlap seen in the visibility of the pulse profiles can be attributed to the gravitational light bending effect.

In order for both poles to remain visible for a significant portion of the rotation period, two conditions must be met. First, the position angle or inclination must be close to 90 degrees. This ensures that both poles have approximately equal visibility throughout the rotation. Second, the magnetic colatitude must be small to prevent the emission regions from going too far "behind the edge" of the neutron star and becoming invisible to the observer. In the example shown in the lower part of Figure 7.14, a magnetic colatitude of
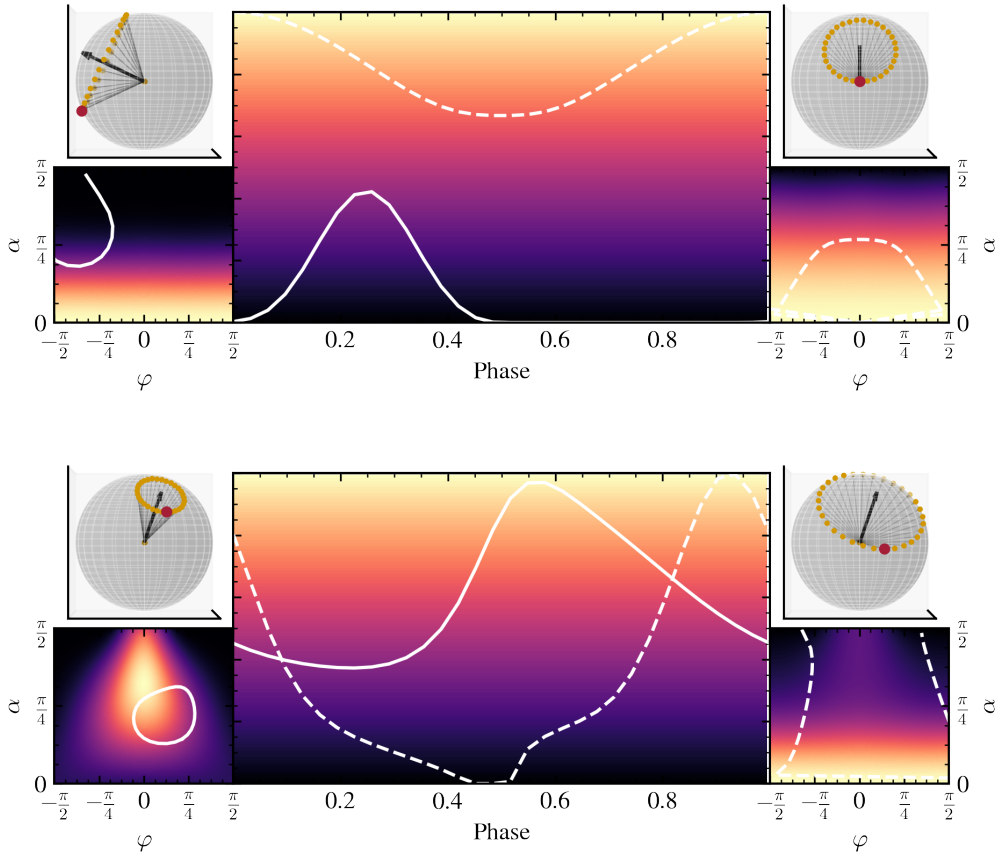
Figure 7.13: Pulse profiles generated with a toy model. The modeled geometries are shown in the panels showing the pulsar. The position of the spin axis is indicated by a black arrow. The emission region on the surface is shown as a red dot at phase zero and as yellow dots as the neutron star rotates. The beam patterns are shown in the panels below the geometry, as a function of α and φ. The solid line corresponds to the geometry and beam pattern on the left, while the dashed lines correspond to the right panels. The top figure shows the results for symmetric intrinsic beam patterns, which produce symmetric profiles. The bottom figure shows asymmetric beam patterns and the resulting asymmetric profiles. The geometries are arbitrarily chosen for illustrative purposes. See the accompanying text for more details.
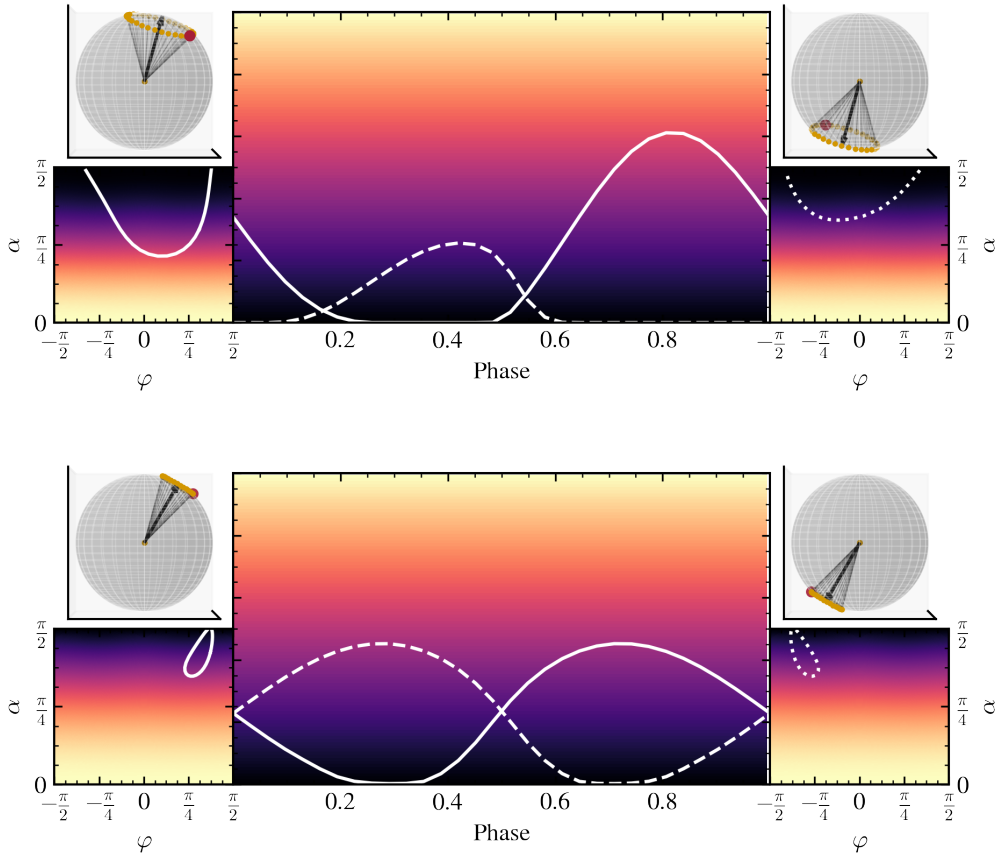
Figure 7.14: Pulse profiles generated with a toy model to illustrate the visibility problem. The figures and panels are similar to Figure 7.13, but here two poles are shown that are strictly antipodal with no offset of the dipole. The upper figure illustrates that in a strictly antipodal geometry, if one pole is visible for most of the rotation, the other pole will not be visible, even when gravitational light bending is taken into account. The lower figure illustrates that to explain an observation where both poles' emission is observable for most of the rotation, a position angle close to 90 degrees and a small magnetic colatitude of less than 15 degrees (shown in the lower figure) are required.

Table 7.1: Toy model parameters for the models shown in Figure 7.13, Figure 7.14, and Figure 7.15. The parameters include the geometry and beam pattern as described in the accompanying text.

Figure	$i[°]$	PA $[°]$	$\theta[°]$	δx_1	δy_1	κ_1	κ_2	γ	$\delta\Phi$
Upper 7.13 left	25	-90	50	0	0	0	0	5	0
Upper 7.13 right	30	0	30	0	0	0	0	1	0
Lower 7.13 left	45	20	20	-1	0	0	0	3	0
Lower 7.13 right	45	20	50	0	0	0	0.4	7	0
Upper 7.14 left	70	50	30	0	0	0	0	2	0.2
Upper 7.14 right	-70	-130	30	0	0	0	0	2	3.34
Lower 7.14 left	60	90	15	0	0	0	0	1	0.2
Lower 7.14 right	-60	-120	15	0	0	0	0	1	3.34
Upper 7.15 left	70	49	16	0.26	-0.97	0.25	0	15	-0.38
Upper 7.15 right	70	-131	16	0.97	1.5	0.25	0	15	2.76
Lower 7.15 left	70	49	16	0.26	-0.97	0.25	0	15	-0.38
Lower 7.15 right	70	-131	16	0.97	1.5	0.25	0	4	-2.35

15 degrees is shown, along with a perfect position angle of 90 degrees. As a result, the emission from both poles remains observable for almost the entire rotation of the pulsar. However, even small deviations from this specific geometry can lead to reduced visibility for at least one of the poles. Also note that any vertical extension of the emission region would greatly affect visibility.

   Using the toy model, I have thus shown that the PCVA results and the total pulse profile can be adequately described by considering small deviations from symmetric beam patterns. By relaxing the assumptions regarding the symmetric beam pattern, it becomes possible to provide a more accurate description of the asymmetric contributions from the poles of the neutron star.

   Despite uncertainties in the determination of the basic pulsar geometry, which should be kept in mind for the interpretation of the results, I used the results of Tsygankov et al. (2022) for the analysis of Cen X−3. This includes an orbital inclination of about 70 degrees, and an estimate of the position angle of the pulsar spin of about 49 degrees with a magnetic co-latitude of about 16 degrees. With these parameters, I used the toy model to explore what beam pattern might result in a single-pole pulse profile similar to that obtained by PCVA. An example of the results is shown in Figure 7.15, which follows the same structure as Figure 7.13 and Figure 7.14 with some modifications. The geometry of the pulsar, including its two poles, is shown in the upper left and right panels. Unlike the previous examples, the parameters used in this case are not arbitrary, but the values determined by Tsygankov et al. (2022) and listed in Table 7.1, along with the corresponding beam

pattern parameters. The corresponding beam patterns are shown below the geometries. The resulting pulse profiles obtained from the toy model are shown in the larger central panel. The two poles are represented by solid green and blue lines, while the total pulse profile is represented by a red line. For reference, the PCVA components are shown as dashed lines, and the observed total pulse profile of Cen X−3 is shown as a dotted red line.

When considering an asymmetric intrinsic beam pattern with respect to the normal, it is possible to reproduce the main features of the first PCVA contribution (left panels and green lines). The resulting single-pole pulse profile shows the same key features, including a minimum followed by a sharp rise to maximum and a gradual decline thereafter. However, reproducing the pulse profile for the second pole proved to be more challenging due to the specific geometry involved.

As shown previously in Figure 7.14, and considering the visibility of the poles during the star's rotation, assuming the geometry of Tsygankov et al. (2022), it is expected that one of the poles will remain observable for a significant portion of the rotation, while the other pole may not be visible for a significant portion of the time, even allowing for gravitational light bending within the assumed dipole geometry. This observation contrasts with the non-zero PCVA result, which indicates that both poles are visible for a substantial portion of the rotation and have similar overall visibility characteristics. To obtain comparable results within the toy model, it would be necessary to adjust the position angle closer to 90 degrees and to reduce the magnetic co-latitude.

To improve the agreement between the model and the observed pulse profiles, the constraints on the geometry parameters can be relaxed to allow an offset of one of the emission regions, which could be caused by an offset of the dipole. The resulting pulse profiles, shown in the lower part of Figure 7.15, are in better agreement with the observed profiles. The inclusion of an offset dipole helps to align the phase of the maximum with the visible portion of the PCVA result. However, despite this modification, the problem of visibility gaps for at least one pole persists, indicating that further refinements are needed to accurately reproduce the observed pulse profiles of Cen X−3.

There are two possible approaches to this problem. First, one could consider further relaxing the assumptions made about the basic geometry of the pulsar, such as the inclination angle. The inferred geometry based on polarimetric observations (Tsygankov et al. 2022) may not be entirely accurate because it relies on several assumptions, such as that the pulsar and orbital inclinations are the same. While this assumption is plausible, it is not necessarily true. In addition, the observed changes in position angle are described by the rotating vector model, and therefore also depend on assumptions. These assumptions could be violated by the presence of an extra polarized component related to scattering in the wind, as seen in Doroshenko et al. (2023), which could also be the case for Cen X−3. Therefore, the geometry of the pulsar can be considered to be rather uncertain. The second approach to solve the problem is to use a more complex model. For example, extended
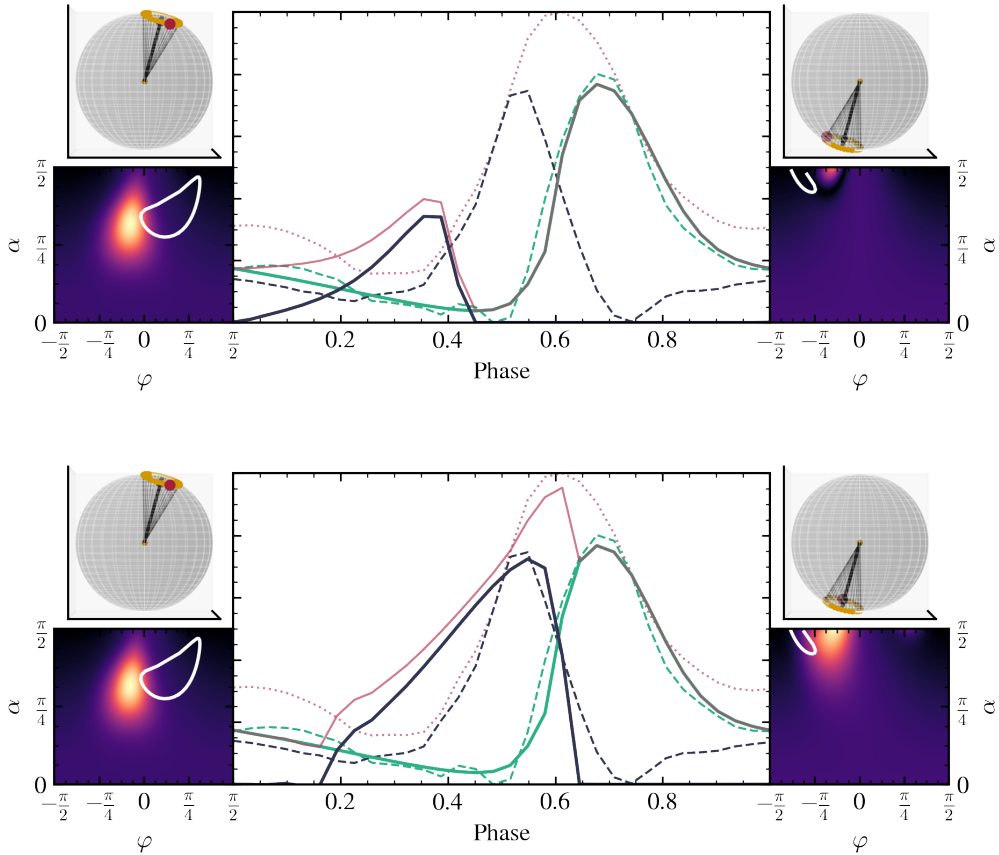
Figure 7.15: Pulse profiles generated with a toy model to try to understand PCVA decomposition, shown as dashed lines. The red dotted line is the total pulse profile. The figures and panels are similar to Figure 7.13, but the geometry is fixed to that determined by Tsygankov et al. (2022). The upper figure uses a strict antipodal geometry. With the asymmetric beam pattern in the lower left panel, one of the PCVA components is well explained. The problem lies in the second component, which is difficult to explain with the strict dipole model due to visibility problems. The lower figure relaxes these parameters and the second pole is much better explained.

emission regions, such as arcs on the surface of the neutron star, could be modeled and their flux integrated (see e.g. Figure 7.3). By considering such a model, a more realistic representation of the physical system can be achieved. Studies by Postnov et al. (2013) and results from the NICER mission, as reported by Riley et al. (2019), suggest that the emission regions in X-ray pulsars may have a higher level of complexity than previously thought. By including the possibility of extended emission regions in the model, the visibility problem encountered in the toy model can be more realistically addressed. Parts of the emission region could remain visible for extended periods during the rotation period, thus resolving some of the visibility gaps.

In summary, although the toy model lacks the complexity of the real system, it demonstrates that certain crucial aspects of the PCVA decomposition can be explained by a relatively simple geometry and intrinsic beam pattern, given the presence of certain asymmetries. However, to achieve a more accurate representation of the observed pulse profiles, either the geometry parameters must be relaxed or a more complex model that accounts for extended emission regions is likely required.

These results indicate that PCVA provides important information and can be used in future analyses to improve our understanding of Cen X−3. Providing these single-pole pulse profiles can help constrain modeling approaches and thus improve our understanding of its complex nature and emission mechanisms.
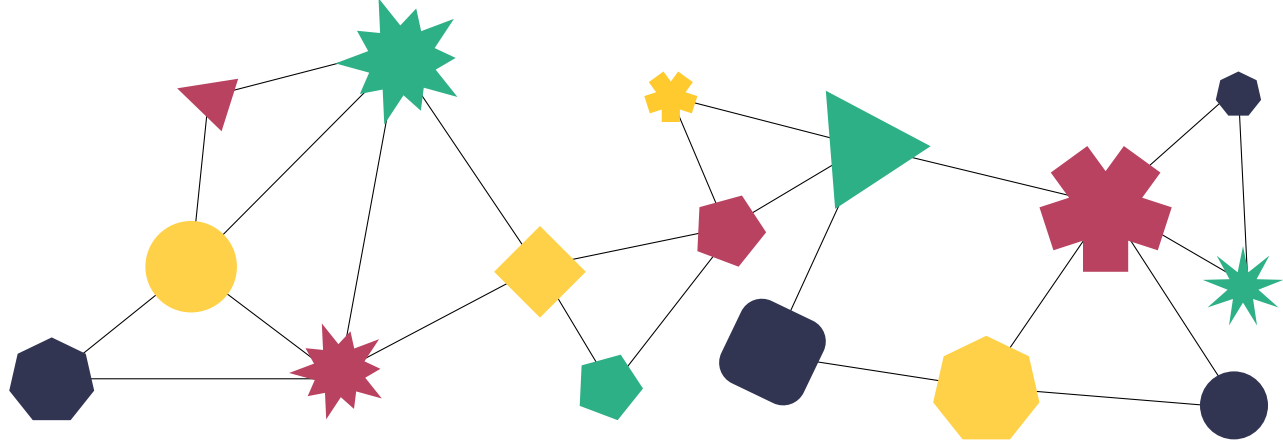
8. Conclusions

In X-ray binaries, the process of accretion of matter from a companion star to a neutron star results in the emission of primarily X-ray radiation. This is observed as pulsations due to a misalignment between the spin and magnetic axes of the neutron star. By performing timing analysis and folding the light curve with the pulse period, pulse profiles are obtained. However, the formation of the pulse profile shape is a highly complex process influenced by the combination of several factors. These factors include the geometric and magnetic configurations of the neutron star, the accretion rate, the spatial distribution of the emission regions and their footprints on the surface, vertical emission structures, phenomena such as gravitational light bending, and, most importantly, the unknown intrinsic local beam pattern defined by details of radiative transfer in strongly magnetized plasma.

Due to the complexity of the problem, there is no clear and coherent understanding of the underlying physical processes in the emission regions. This makes the verification of theoretical models challenging. The aim of this work was to fill this gap from a new perspective. Using a new approach to pulse profile decomposition, I disentangled the components contributing to the total pulse profile. Taking into account that most of the accretion occurs at the two magnetic poles of the neutron star, and that the flux variability traces fluctuations in the accretion rate, the decomposition of the pulse profile can be reformulated as a blind source separation problem. Blind source separation can be visualized as a classical concert scenario where several instruments are playing simultaneously, but a listener can selectively focus on each instrument and perceive them almost as if they were recorded independently. Similarly, our goal is to detect the accretion occurring at the poles of the X-ray pulsar, which produces unique observable X-ray signals similar to the instruments in the concert analogy. The independent flickering, which occurs on the timescale of the pulsar's spin period, is used to distinguish the signals coming from the two poles of the neutron star.

In this thesis, I have explored these issues by first providing an overview of the

context, which includes topics such as neutron stars, binary systems, pulse profiles, and their formation. I have also introduced the concept of blind source separation, including some example applications and existing algorithms for solving it. I then showed that the phase-resolved pulse-to-pulse light curves exhibit correlation properties that support the notion that separable signals exist, which can be exploited using blind source separation techniques to separate them. Next, I developed and tested the phase correlated variability analysis (PCVA) with a series of simulations. For an effective decomposition, I used a blind source separation algorithm to first disentangle the components and then recover their scaling using the phase correlation information of the light curve. I also performed simulations to identify the most appropriate blind source separation algorithm for this application. By comparing the input data of the simulations with the recovered components obtained by PCVA, the performance of the algorithms could be evaluated. I then selected a non-negative matrix factorization algorithm and used it for verification checks. Finally, I estimated the uncertainties associated with the recovered components. Based on numerous simulation tests and verification steps, I concluded that the PCVA successfully recovers the input pulse profiles.

PCVA can be applied to a wide range of luminous X-ray pulsars, making it a valuable tool for future studies in this field. This thesis provides a general guide detailing the basic steps, requirements, and limitations of PCVA, effectively serving as a recipe for future studies. Bright X-ray pulsars such as 4U 0115+63, Vela X−1, V 0332+53, 1A 0535+262, EXO 2030+375, and GX 301−2 can be interesting targets to study if the observational parameters allow. In addition, Her X−1 could possibly be studied by stacking several observations. The varying pulse profile during the super-orbital period makes Her X−1 particularly interesting to study. However, any source that exhibits variations in its pulse profile with respect to time, energy, or luminosity can be an interesting target. The profile variations may provide insights into changes in the accretion process and structures, and the individual contributions of each pole to these changes could be revealed. These future studies will benefit from instruments such as IXPE or the upcoming eXTP observatory.

Applying the new PCVA to the RXTE (Rossi X-ray Timing Explorer) data from Cen X−3, I found that the recovered components consist of two distinct single-pole pulse profiles of approximately equal amplitude and width. Contrary to the assumptions of previous investigations, these profiles exhibit asymmetry and appear to be reflected in phase. These results are not consistent with previous literature, mainly due to the lack of intrinsic symmetry. To explore these findings further, I created a toy model to describe the expected pulse profiles. This is based on several assumptions. First, the geometry of the system must be specified, including an inclination and position angle of the pulsar spin. Second, the emission regions are assumed to be single sources at each pole. Finally, the beam pattern is defined phenomenologically as symmetric about some direction, but asymmetric with respect to the normal of the surface. The resulting pulse profiles are

asymmetric due to this small deviation in the beam pattern. In addition, the toy model allows for an offset of the dipole. Finally, gravitational light bending is also taken into account in the model. This toy model can be used to conveniently explore the influence of various parameters, in particular the influence of an asymmetric intrinsic beam pattern, on the pulse profiles.

When studying the Cen X−3 PCVA results in the context of the toy model, a problem in the visibility of the emission regions emerges as the biggest challenge. The mostly non-zero contributions throughout the rotation suggest a larger visibility than is obtainable with literature geometries for Cen X−3. One is to relax the basic pulsar geometry, since literature geometries are also model-dependent, and the other is to extend the toy model to include more complex beam patterns or extended emission regions to solve visibility problems.

This analysis shows that PCVA provides important information for understanding observations of accreting X-ray pulsars. The single-pole pulse profiles it returns can be used in the future to constrain models and thus improve our understanding of the complex emission of these objects.

Bibliography

Ablin, P., Cardoso, J.-F., & Gramfort, A. 2017, Faster ICA under orthogonal constraint

Ablin, P., Cardoso, J.-F., & Gramfort, A. 2018, IEEE Transactions on Signal Processing, 66, 4040

Abney, W. D. W. 1877a, MNRAS, 37, 278

Abney, W. D. W. 1877b, The Observatory, 1, 134

Alonso-Hernández, J., Fürst, F., Kretschmar, P., Caballero, I., & Joyce, A. M. 2022, A&A, 662, A62

Annala, M. & Poutanen, J. 2010, A&A, 520, A76

Antoniadis, J., Freire, P. C. C., Wex, N., et al. 2013, Science, 340, 448

Arnaud, K., Smith, R., & Siemiginowska, A. 2011, Handbook of X-ray Astronomy

Arons, J. & Lea, S. M. 1976, ApJ, 207, 914

Arons, J. & Lea, S. M. 1980, ApJ, 235, 1016

Arzoumanian, Z., Brazier, A., Burke-Spolaor, S., et al. 2018, ApJS, 235, 37

Aschenbach, B. 1985, Reports on Progress in Physics, 48, 579

Ash, T. D. C., Reynolds, A. P., Roche, P., et al. 1999, MNRAS, 307, 357

Bachetti, M., Harrison, F. A., Walton, D. J., et al. 2014, Nature, 514, 202

Barthelmy, S. D., Barbier, L. M., Cummings, J. R., et al. 2005, Space Sci. Rev., 120, 143

Basko, M. M. & Sunyaev, R. A. 1976, MNRAS, 175, 395

Becker, P. A., Klochkov, D., Schönherr, G., et al. 2012, A&A, 544, A123

Becker, P. A. & Wolff, M. T. 2007, ApJ, 654, 435

Beloborodov, A. M. 2002, ApJ, 566, L85

Bhattacharya, D. & van den Heuvel, E. P. J. 1991, Phys. Rep., 203, 1

Bildsten, L., Chakrabarty, D., Chiu, J., et al. 1997, ApJS, 113, 367

Biryukov, A. & Abolmasov, P. 2021, MNRAS, 505, 1775

Blum, S. & Kraus, U. 2000, ApJ, 529, 968

Bobin, J., Rapin, J., Larue, A., & Starck, J.-L. 2015, IEEE Transactions on Signal Processing, 63, 1199

Bogdanov, S., Guillot, S., Ray, P. S., et al. 2019a, ApJ, 887, L25

Bogdanov, S., Lamb, F. K., Mahmoodifar, S., et al. 2019b, ApJ, 887, L26

Bombaci, I. 1996, A&A, 305, 871

Bondi, H. & Hoyle, F. 1944, MNRAS, 104, 273

Bradt, H. 1997, in Ital. Phys. Soc. Conf. Ser. 57: Frontier Objects in Astrophysics and Particle Physics, ed. F. Giovannelli & G. Mannocchi, 169

Bradt, H. V., Rothschild, R. E., & Swank, J. H. 1993, A&AS, 97, 355

Bradt, H. V. & Swank, J. H. 1989, in NATO Advanced Study Institute (ASI) Series C, Vol. 262, Timing Neutron Stars, ed. H. Ögelman & E. P. J. van den Heuvel, 393

Brumback, M. C., Hickox, R. C., Fürst, F. S., et al. 2021, ApJ, 909, 186

Bulik, T., Gondek-Rosińska, D., Santangelo, A., et al. 2003, A&A, 404, 1023

Bulik, T., Meszaros, P., Woo, J. W., Hagase, F., & Makishima, K. 1992, ApJ, 395, 564

Bulik, T., Riffert, H., Meszaros, P., et al. 1995, ApJ, 444, 405

Burgio, G. F., Schulze, H. J., Vidaña, I., & Wei, J. B. 2021, Progress in Particle and Nuclear Physics, 120, 103879

Burnard, D. J., Klein, R. I., & Arons, J. 1988, ApJ, 324, 1001

Caballero, I., Kraus, U., Santangelo, A., Sasaki, M., & Kretschmar, P. 2011, A&A, 526, A131

Caballero, I. & Wilms, J. 2012, Mem. Soc. Astron. Italiana, 83, 230

Caiazzo, I. & Heyl, J. 2021, MNRAS, 501, 129

Camenzind, M. 2007, Compact objects in astrophysics : white dwarfs, neutron stars, and black holes

Campana, R. 2017, pyLCSIM: X-ray lightcurves simulator, Astrophysics Source Code Library, record ascl:1708.016

Cappallo, R., Laycock, S. G. T., & Christodoulou, D. M. 2017, PASP, 129, 124201

Cardoso, J.-F. 1998, in Proceedings of the 1998 IEEE International Conference on Acoustics, Speech and Signal Processing, ICASSP '98 (Cat. No.98CH36181), Vol. 4, 1941–1944 vol.4

Carloni Gertosio, R., Bobin, J., & Acero, F. 2022, arXiv e-prints, arXiv:2209.13585

Castor, J. I., Abbott, D. C., & Klein, R. I. 1975, ApJ, 195, 157

Cerda-Duran, P. & Elias-Rosa, N. 2018, in Astrophysics and Space Science Library, Vol. 457, Astrophysics and Space Science Library, ed. L. Rezzolla, P. Pizzochero, D. I. Jones, N. Rea, & I. Vidaña, 1

Chan, W. C. 2013, Performance analysis of telecommunications and local area networks, The Springer International Series in Engineering and Computer Science (New York, NY: Springer)

Chen, X., Wang, W., Tang, Y. M., et al. 2021, ApJ, 919, 33

Chien, J.-T. & Chen, B.-C. 2006, Audio, Speech, and Language Processing, IEEE Transactions on, 14, 1245

Chodil, G., Mark, H., Rodrigues, R., et al. 1967, Phys. Rev. Lett., 19, 681

Crilly, P. & Carlson, A. 2009, Communication Systems (McGraw-Hill Education)

Cromartie, H. T., Fonseca, E., Ransom, S. M., et al. 2020, Nature Astronomy, 4, 72

Davidson, K. & Ostriker, J. P. 1973, ApJ, 179, 585

Demorest, P. B., Pennucci, T., Ransom, S. M., Roberts, M. S. E., & Hessels, J. W. T. 2010, Nature, 467, 1081

Dietrich, T., Coughlin, M. W., Pang, P. T. H., et al. 2020, Science, 370, 1450

Diez, C. M., Grinberg, V., Fürst, F., et al. 2023, arXiv e-prints, arXiv:2303.09631

Doroshenko, V., Poutanen, J., Heyl, J., et al. 2023, arXiv e-prints, arXiv:2306.02116

Doroshenko, V., Poutanen, J., Tsygankov, S. S., et al. 2022a, Nature Astronomy, 6, 1433

Doroshenko, V., Santangelo, A., Kreykenbohm, I., & Doroshenko, R. 2012, A&A, 540, L1

Doroshenko, V., Suleimanov, V., Pühlhofer, G., & Santangelo, A. 2022b, Nature Astronomy, 6, 1444

Doroshenko, V., Tsygankov, S. S., Mushtukov, A. A., et al. 2017, MNRAS, 466, 2143

Doroshenko, V., Zhang, S. N., Santangelo, A., et al. 2020, MNRAS, 491, 1857

Drischler, C., Han, S., Lattimer, J. M., et al. 2021, Phys. Rev. C, 103, 045808

Ducci, L., Sidoli, L., Mereghetti, S., Paizis, A., & Romano, P. 2009, MNRAS, 398, 2152

El Mellah, I., Grinberg, V., Sundqvist, J. O., Driessen, F. A., & Leutenegger, M. A. 2020, A&A, 643, A9

Elsner, R. F. & Lamb, F. K. 1976, Nature, 262, 356

Elsner, R. F. & Lamb, F. K. 1977, ApJ, 215, 897

Fahes, M., Kervazo, C., Bobin, J., & Tupin, F. 2022, Unrolling PALM for sparse semi-blind source separation

Ferrigno, C., Becker, P. A., Segreto, A., Mineo, T., & Santangelo, A. 2009, A&A, 498, 825

Ferrigno, C., Falanga, M., Bozzo, E., et al. 2011, A&A, 532, A76

Forsblom, S. V., Poutanen, J., Tsygankov, S. S., et al. 2023, arXiv e-prints, arXiv:2303.01800

Fürst, F., Kretschmar, P., Grinberg, V., et al. 2019, Astronomische Nachrichten, 340, 323

Fürst, F., Kreykenbohm, I., Pottschmidt, K., et al. 2010, A&A, 519, A37

Garg, A., Rawat, D., Bhargava, Y., Méndez, M., & Bhattacharyya, S. 2023, arXiv e-prints, arXiv:2304.00889

Gehrels, N., Chincarini, G., Giommi, P., et al. 2004, ApJ, 611, 1005

Gendreau, K. C., Arzoumanian, Z., Adkins, P. W., et al. 2016, in Society of Photo-Optical Instrumentation Engineers (SPIE) Conference Series, Vol. 9905, Space Telescopes and Instrumentation 2016: Ultraviolet to Gamma Ray, ed. J.-W. A. den Herder, T. Takahashi, & M. Bautz, 99051H

Ghosh, P. & Lamb, F. K. 1979a, ApJ, 232, 259

Ghosh, P. & Lamb, F. K. 1979b, ApJ, 234, 296

Giacconi, R., Gursky, H., Kellogg, E., Schreier, E., & Tananbaum, H. 1971a, ApJ, 167, L67

Giacconi, R., Kellogg, E., Gorenstein, P., Gursky, H., & Tananbaum, H. 1971b, ApJ, 165, L27

Glasser, C. A., Odell, C. E., & Seufert, S. E. 1994, IEEE Transactions on Nuclear Science, 41, 1343

Grinberg, V., Hell, N., El Mellah, I., et al. 2017, A&A, 608, A143

Guillot, S. & Rutledge, R. E. 2014, ApJ, 796, L3

Guillot, S., Servillat, M., Webb, N. A., & Rutledge, R. E. 2013, ApJ, 772, 7

Haberl, F., Angelini, L., Motch, C., & White, N. E. 1998, A&A, 330, 189

Haensel, P., Potekhin, A. Y., & Yakovlev, D. G. 2007, Neutron Stars 1 : Equation of State and Structure, Vol. 326

Harding, A. K. & Lai, D. 2006, Reports on Progress in Physics, 69, 2631

Harris, C. R., Millman, K. J., van der Walt, S. J., et al. 2020, Nature, 585, 357

Hasinger, G. & van der Klis, M. 1989, A&A, 225, 79

Hassan, N. & Ramli, D. A. 2018, Procedia Computer Science, 126, 363, knowledge-Based and Intelligent Information and Engineering Systems: Proceedings of the 22nd International Conference, KES-2018, Belgrade, Serbia

Heger, A., Fryer, C. L., Woosley, S. E., Langer, N., & Hartmann, D. H. 2003, ApJ, 591, 288

Herault, J. & Jutten, C. 1986, in American Institute of Physics Conference Series, Vol. 151, Neural Networks for Computing, 206–211

Hewish, A., Bell, S. J., Pilkington, J. D. H., Scott, P. F., & Collins, R. A. 1968, Nature, 217, 709

Hockey, T., Trimble, V., Williams, T. R., et al. 2007, The Biographical Encyclopedia of Astronomers

Hou, X., You, Y., Ji, L., et al. 2022, ApJ, 941, 126

Hu, Y. F., Ji, L., Yu, C., et al. 2023, ApJ, 945, 138

Hulse, R. A. & Taylor, J. H. 1975, ApJ, 195, L51

Hunter, J. D. 2007, Computing in Science & Engineering, 9, 90

Huppenkothen, D., Bachetti, M., Stevens, A., et al. 2019, Journal of Open Source Software, 4, 1393

Huppenkothen, D., Bachetti, M., Stevens, A. L., et al. 2019, ApJ, 881, 39

Hyvärinen, A., Karhunen, J., & Oja, E. 2004, Independent Component Analysis, Adaptive and Cognitive Dynamic Systems: Signal Processing, Learning, Communications and Control (Wiley)

Iben, Icko, J. 1991, ApJS, 76, 55

Iping, R. C. & Petterson, J. A. 1990, A&A, 239, 221

Israel, G. L., Belfiore, A., Stella, L., et al. 2017, Science, 355, 817

Iwakiri, W. B., Pottschmidt, K., Falkner, S., et al. 2019, ApJ, 878, 121

Jahoda, K., Markwardt, C. B., Radeva, Y., et al. 2006, ApJS, 163, 401

Jahoda, K., Swank, J. H., Giles, A. B., et al. 1996, in Society of Photo-Optical Instrumentation Engineers (SPIE) Conference Series, Vol. 2808, EUV, X-Ray, and Gamma-Ray Instrumentation for Astronomy VII, ed. O. H. Siegmund & M. A. Gummin, 59–70

Kaminker, A. D., Pavlov, G. G., & Shibanov, Y. A. 1983, Soviet Astronomy Letters, 9, 58

Karino, S. 2007, PASJ, 59, 961

Kim, D.-H. & Trippe, S. 2021, arXiv e-prints, arXiv:2109.13387

Klawin, M., Doroshenko, V., Santangelo, A., et al. 2023, A&A

Klochkov, D., Doroshenko, V., Santangelo, A., et al. 2012, A&A, 542, L28

Konar, S. 2013, in Astronomical Society of India Conference Series, Vol. 8, Astronomical Society of India Conference Series, 89–95

Konar, S. 2017, Journal of Astrophysics and Astronomy, 38, 47

Konar, S., Bagchi, M., Bandyopadhyay, D., et al. 2016, Journal of Astrophysics and Astronomy, 37, 36

Kong, L.-D., Zhang, S., Zhang, S.-N., et al. 2022, ApJ, 933, L3

Kraus, U. 2001, ApJ, 563, 289

Kraus, U., Blum, S., Schulte, J., Ruder, H., & Meszaros, P. 1996, ApJ, 467, 794

Kraus, U., Nollert, H. P., Ruder, H., & Riffert, H. 1995, ApJ, 450, 763

Kretschmar, P., El Mellah, I., Martínez-Núñez, S., et al. 2021, A&A, 652, A95

Kreykenbohm, I., Wilms, J., Kretschmar, P., et al. 2008, in The 7th INTEGRAL Workshop, 107

Krzeminski, W. 1974, ApJ, 192, L135

Kuruoğlu, E. E., Bedini, L., Paratore, M. T., Salerno, E., & Tonazzini, A. 2003, Neural Networks, 16, 479, neural Network Analysis of Complex Scientific Data: Astronomy and Geosciences

Kutschera, M. 1998, Acta Physica Polonica B, 29, 25

Lamb, F. K., Boutloukos, S., Van Wassenhove, S., et al. 2009, ApJ, 706, 417

Lamb, F. K., Pethick, C. J., & Pines, D. 1973, ApJ, 184, 271

Langer, N. 2012, ARA&A, 50, 107

Lattimer, J. M. 2012, Annual Review of Nuclear and Particle Science, 62, 485

Lattimer, J. M. 2019, in American Institute of Physics Conference Series, Vol. 2127, Xiamen-CUSTIPEN Workshop on the Equation of State of Dense Neutron-Rich Matter in the Era of Gravitational Wave Astronomy, 020001

Lattimer, J. M. & Prakash, M. 2004, Science, 304, 536

Lattimer, J. M. & Steiner, A. W. 2014, ApJ, 784, 123

Lazar, C. & Doncescu, A. 2009, in 2009 International Conference on Complex, Intelligent and Software Intensive Systems, 924–929

Leahy, D. A. 1991, MNRAS, 251, 203

Leahy, D. A. 2004, ApJ, 613, 517

Leahy, D. A., Morsink, S. M., Chung, Y.-Y., & Chou, Y. 2009, ApJ, 691, 1235

Lee, D. D. & Seung, H. S. 1999, Nature, 401, 788

Lever, J., Krzywinski, M., & Altman, N. 2017, Nature Methods, 14, 641

Li, T.-P. 2007, Nuclear Physics B Proceedings Supplements, 166, 131

Li, X., Li, X., Tan, Y., et al. 2020, Journal of High Energy Astrophysics, 27, 64

Li, X., Liu, C., Chang, Z., et al. 2019, Journal of High Energy Astrophysics, 24, 6

Lim, Y. & Holt, J. W. 2022, Galaxies, 10, 99

Liu, C., Zhang, Y., Li, X., et al. 2020, Science China Physics, Mechanics, and Astronomy, 63, 249503

Long, M., Romanova, M. M., & Lovelace, R. V. E. 2007, MNRAS, 374, 436

Longair, M. S. 2011, High Energy Astrophysics

Lorimer, D. R. 2008, Living Reviews in Relativity, 11, 8

Luo, Z., Li, C., & Zhu, L. 2018, IEEE Access, 6, 66685

Lyubarskii, Y. E. 1997, MNRAS, 292, 679

Malacaria, C., Heyl, J., Doroshenko, V., et al. 2023, arXiv e-prints, arXiv:2304.00925

Malacaria, C., Mihara, T., Santangelo, A., et al. 2016, A&A, 588, A100

Mason, A. B., Clark, J. S., Norton, A. J., Negueruela, I., & Roche, P. 2009, A&A, 505, 281

Matsuoka, M., Kawasaki, K., Ueno, S., et al. 2009, PASJ, 61, 999

Meszáros, P. 1984, Space Sci. Rev., 38, 325

Mészáros, P. 1984, in American Institute of Physics Conference Series, Vol. 115, High Energy Transients in AstroPhysics, ed. S. E. Woosley, 165–178

Meszaros, P. & Nagel, W. 1985, ApJ, 299, 138

Meszaros, P., Novick, R., Szentgyorgyi, A., Chanan, G. A., & Weisskopf, M. C. 1988, ApJ, 324, 1056

Mihara, T., Makishima, K., & Nagase, F. 2004, ApJ, 610, 390

Mihara, T., Nakajima, M., Sugizaki, M., et al. 2011, PASJ, 63, S623

Miller, M. C., Lamb, F. K., Dittmann, A. J., et al. 2019, ApJ, 887, L24

Miller, M. C., Lamb, F. K., Dittmann, A. J., et al. 2021, ApJ, 918, L28

Mönkkönen, J., Tsygankov, S. S., Mushtukov, A. A., et al. 2022, MNRAS, 515, 571

Mukherjee, D. & Bhattacharya, D. 2012, MNRAS, 420, 720

Mukherjee, D., Bhattacharya, D., & Mignone, A. 2014, in European Physical Journal Web of Conferences, Vol. 64, European Physical Journal Web of Conferences, 02004

Müller, D., Klochkov, D., Santangelo, A., Mihara, T., & Sugizaki, M. 2011, A&A, 535, A102

Mushtukov, A. & Tsygankov, S. 2022, arXiv e-prints, arXiv:2204.14185

Mushtukov, A. A., Suleimanov, V. F., Tsygankov, S. S., & Portegies Zwart, S. 2021, MNRAS, 503, 5193

Mushtukov, A. A., Suleimanov, V. F., Tsygankov, S. S., & Poutanen, J. 2015a, MNRAS, 454, 2539

Mushtukov, A. A., Suleimanov, V. F., Tsygankov, S. S., & Poutanen, J. 2015b, MNRAS, 447, 1847

Mushtukov, A. A., Tsygankov, S. S., Poutanen, J., et al. 2023, arXiv e-prints, arXiv:2303.17325

Mushtukov, A. A., Tsygankov, S. S., Serber, A. V., Suleimanov, V. F., & Poutanen, J.

2015c, MNRAS, 454, 2714

Nagase, F. 1989, PASJ, 41, 1

Najarian, K. & Splinter, R. 2012, Biomedical Signal and Image Processing, 2nd edn. (Boca Raton, FL: CRC Press)

Nang, Y., Liao, J.-Y., Sai, N., et al. 2020, Journal of High Energy Astrophysics, 25, 39

Naso, L., Miller, J., & Kluźniak, W. 2013, in International Journal of Modern Physics Conference Series, Vol. 23, International Journal of Modern Physics Conference Series, 106–110

Nättilä, J. & Kajava, J. J. E. 2022, arXiv e-prints, arXiv:2211.15721

Nelke, C. M., Jax, P., & Vary, P. 2016

Oppenheimer, J. R. & Volkoff, G. M. 1939, Physical Review, 55, 374

Orlandini, M. 2006, Advances in Space Research, 38, 2742

Ott, C. D., Burrows, A., Thompson, T. A., Livne, E., & Walder, R. 2006, ApJS, 164, 130

Özel, F. & Freire, P. 2016, ARA&A, 54, 401

Özel, F., Psaltis, D., Arzoumanian, Z., Morsink, S., & Bauböck, M. 2016, ApJ, 832, 92

Ozgen, M. T., Kuruoglu, E. E., & Herranz, D. 2008, Digital Signal Processing, 18, 360

Parmar, A. N., White, N. E., & Stella, L. 1989, ApJ, 338, 373

Paul, B., Raichur, H., & Mukherjee, U. 2005, A&A, 442, L15

Pearson, K. 1901, The London, Edinburgh, and Dublin philosophical magazine and journal of science, 2, 559

Pedregosa, F., Varoquaux, G., Gramfort, A., et al. 2011, Journal of Machine Learning Research, 12, 2825

Picquenot, A., Acero, F., Bobin, J., et al. 2019, A&A, 627, A139

Piraino, S., Santangelo, A., di Salvo, T., et al. 2007, A&A, 471, L17

Postnov, K., Shakura, N., Staubert, R., et al. 2013, MNRAS, 435, 1147

Poutanen, J. & Beloborodov, A. M. 2006, MNRAS, 373, 836

Poutanen, J., Mushtukov, A. A., Suleimanov, V. F., et al. 2013, ApJ, 777, 115

Pringle, J. E. & Rees, M. J. 1972, A&A, 21, 1

Raichur, H. & Paul, B. 2010, MNRAS, 401, 1532

Rajeswari, J. & Jagannath, M. 2017, Informatics in Medicine Unlocked, 8, 13

Ramli, D. A., Shiong, Y. H., & Hassan, N. 2020, Procedia Computer Science, 176, 582, knowledge-Based and Intelligent Information and Engineering Systems: Proceedings of the 24th International Conference KES2020

Rees, M. J. 1975, MNRAS, 171, 457

Reig, P. 2011, Ap&SS, 332, 1

Reig, P. & Roche, P. 1999, MNRAS, 306, 100

Revnivtsev, M., Churazov, E., Postnov, K., & Tsygankov, S. 2009, A&A, 507, 1211

Riffert, H. & Meszaros, P. 1988, ApJ, 325, 207

Riffert, H., Nollert, H. P., Kraus, U., & Ruder, H. 1993, ApJ, 406, 185

Riley, T. E., Watts, A. L., Bogdanov, S., et al. 2019, ApJ, 887, L21

Riley, T. E., Watts, A. L., Ray, P. S., et al. 2021, ApJ, 918, L27

Romani, R. W., Kandel, D., Filippenko, A. V., Brink, T. G., & Zheng, W. 2022, ApJ, 934, L17

Romano, P., Cusumano, G., Campana, S., et al. 2005, in Society of Photo-Optical Instrumentation Engineers (SPIE) Conference Series, Vol. 5898, UV, X-Ray, and Gamma-Ray Space Instrumentation for Astronomy XIV, ed. O. H. W. Siegmund, 369–376

Romanova, M. M., Ustyugova, G. V., Koldoba, A. V., & Lovelace, R. V. E. 2004, ApJ, 610, 920

Romanova, M. M., Ustyugova, G. V., Koldoba, A. V., Wick, J. V., & Lovelace, R. V. E. 2003, ApJ, 595, 1009

Rothschild, R. E., Kühnel, M., Pottschmidt, K., et al. 2017, MNRAS, 466, 2752

Ryan, S. G. & Norton, A. J. 2010, Stellar Evolution and Nucleosynthesis

Sanjurjo-Ferrín, G., Torrejón, J. M., Postnov, K., et al. 2021, MNRAS, 501, 5892

Sasaki, M., Klochkov, D., Kraus, U., Caballero, I., & Santangelo, A. 2010, A&A, 517, A8

Sasaki, M., Müller, D., Kraus, U., Ferrigno, C., & Santangelo, A. 2012, A&A, 540, A35

Schneider, P. 2015, Extragalactic Astronomy and Cosmology: An Introduction

Schreier, E., Levinson, R., Gursky, H., et al. 1972, ApJ, 172, L79

Seidman, S., Guag, J., Beard, B., & Arp, Z. 2021, Heart Rhythm, 18

Serylak, M., Venkatraman Krishnan, V., Freire, P. C. C., et al. 2022, A&A, 665, A53

Shapiro, S. L. & Teukolsky, S. A. 1986, Black Holes, White Dwarfs and Neutron Stars: The Physics of Compact Objects

Sidoli, L. 2017, in XII Multifrequency Behaviour of High Energy Cosmic Sources Workshop (MULTIF2017), 52

Silva Aguirre, V. 2018, in Astrophysics and Space Science Proceedings, Vol. 49, Asteroseismology and Exoplanets: Listening to the Stars and Searching for New Worlds, ed. T. L. Campante, N. C. Santos, & M. J. P. F. G. Monteiro, 3

Sompairac, N., Nazarov, P. V., Czerwinska, U., et al. 2019, International Journal of Molecular Sciences, 20

Spruit, H. C. 2008, in American Institute of Physics Conference Series, Vol. 983, 40 Years of Pulsars: Millisecond Pulsars, Magnetars and More, ed. C. Bassa, Z. Wang, A. Cumming, & V. M. Kaspi, 391–398

Stairs, I. H. 2004, Science, 304, 547

Staubert, R., Schandl, S., Klochkov, D., et al. 2006, in American Institute of Physics Conference Series, Vol. 840, The Transient Milky Way: A Perspective for MIRAX, ed. F. D'Amico, J. Braga, & R. E. Rothschild, 65–70

Staubert, R., Shakura, N. I., Postnov, K., et al. 2007, A&A, 465, L25

Staubert, R., Trümper, J., Kendziorra, E., et al. 2019, A&A, 622, A61

Steiner, A. W., Lattimer, J. M., & Brown, E. F. 2013, ApJ, 765, L5

Sugizaki, M., Mihara, T., Serino, M., et al. 2011, PASJ, 63, S635

Suleimanov, V. F., Poutanen, J., & Werner, K. 2020, A&A, 639, A33

Sun, S., Yu, W., Yu, Y., Mao, D., & Lin, J. 2019, ApJ, 885, 55

Taha, L. & Abdel-Raheem, E. 2020, Sensors, 20, 3536

Takahashi, H. R. & Ohsuga, K. 2017, ApJ, 845, L9

Thorsett, S. E. & Chakrabarty, D. 1999, ApJ, 512, 288

Tolman, R. C. 1939, Physical Review, 55, 364

Torregrosa, Á., Rodes-Roca, J. J., Torrejón, J. M., Sanjurjo-Ferrín, G., & Bernabéu, G. 2022, Rev. Mexicana Astron. Astrofis., 58, 355

Truemper, J., Pietsch, W., Reppin, C., et al. 1978, ApJ, 219, L105

Tsygankov, S. S., Doroshenko, V., Lutovinov, A. A., Mushtukov, A. A., & Poutanen, J. 2017, A&A, 605, A39

Tsygankov, S. S., Doroshenko, V., Mushtukov, A. A., et al. 2023, arXiv e-prints, arXiv:2302.06680

Tsygankov, S. S., Doroshenko, V., Poutanen, J., et al. 2022, ApJ, 941, L14

Tsygankov, S. S., Lutovinov, A. A., Churazov, E. M., & Sunyaev, R. A. 2006, MNRAS, 371, 19

Tuo, Y. L., Ji, L., Tsygankov, S. S., et al. 2020, Journal of High Energy Astrophysics, 27, 38

Vybornov, V., Doroshenko, V., Staubert, R., & Santangelo, A. 2018, A&A, 610, A88

Walter, R. & Ferrigno, C. 2017, in Handbook of Supernovae, ed. A. W. Alsabti & P. Murdin, 1385

Walter, R. & Zurita Heras, J. 2007, A&A, 476, 335

Wang, P. J., Kong, L. D., Zhang, S., et al. 2022, ApJ, 935, 125

Wang, Y. M. & Welter, G. L. 1981, A&A, 102, 97

Watts, A. L. 2019, in American Institute of Physics Conference Series, Vol. 2127, Xiamen-CUSTIPEN Workshop on the Equation of State of Dense Neutron-Rich Matter in the Era of Gravitational Wave Astronomy, 020008

Watts, A. L., Andersson, N., Chakrabarty, D., et al. 2016, Reviews of Modern Physics, 88, 021001

Watts, A. L., Yu, W., Poutanen, J., et al. 2019, Science China Physics, Mechanics, and Astronomy, 62, 29503

Weigert, A. & Wendker, H. J. 2010, Astronomie und Astrophysik - ein Grundkurs.

Weisskopf, M. C., Soffitta, P., Baldini, L., et al. 2022, Journal of Astronomical Telescopes, Instruments, and Systems, 8, 026002

White, N. E., Swank, J. H., & Holt, S. S. 1983, ApJ, 270, 711

White, N. E. & Zhang, W. 1997, ApJ, 490, L87

Wilms, J., Allen, A., & McCray, R. 2000, ApJ, 542, 914

Wolff, M. T., Guillot, S., Bogdanov, S., et al. 2021, ApJ, 918, L26

Wolter, H. 1952a, Annalen der Physik, 445, 94

Wolter, H. 1952b, Annalen der Physik, 445, 286

Wright, E. & Reynders, D. 2004, Practical telecommunications and wireless communications, Practical professional books from Elsevier (London, England: Newnes)

Zhang, S., Santangelo, A., Feroci, M., et al. 2019, Science China Physics, Mechanics, and Astronomy, 62, 29502

Zhang, S. N., Feroci, M., Santangelo, A., et al. 2016, in Society of Photo-Optical Instrumentation Engineers (SPIE) Conference Series, Vol. 9905, Space Telescopes and Instrumentation 2016: Ultraviolet to Gamma Ray, ed. J.-W. A. den Herder, T. Takahashi, & M. Bautz, 99051Q

Zhang, S.-N., Li, T., Lu, F., et al. 2020, Science China Physics, Mechanics, and Astronomy, 63, 249502

Zhang, W., Giles, A. B., Jahoda, K., et al. 1993, in Society of Photo-Optical Instrumentation Engineers (SPIE) Conference Series, Vol. 2006, EUV, X-Ray, and Gamma-Ray Instrumentation for Astronomy IV, ed. O. H. Siegmund, 324–333

Zhang, W., Tait, A., Huang, C., et al. 2023, Nature Communications, 14, 1107

Zhang, X., Wang, Q., & Jin, Y. 2019, in Artificial Intelligence and Security, ed. X. Sun, Z. Pan, & E. Bertino (Cham: Springer International Publishing), 253–265

Zhou, Q., Jiepeng, Y., Li, J., Wang, Z.-Y., & Huang, L. 2022, Multidimensional Systems and Signal Processing, 33

Zieliński, T. P. 2021, Starting digital signal processing in telecommunication engineering: A laboratory-based course (Cham, Switzerland: Springer Nature)

Index

Symbols

A

B

C

N

O

P

R

S

T

U

V

W

X

Z

Acknowledgements

Research is a collaborative effort, and this thesis would not have been possible without the contributions of numerous individuals who supported me in various ways. I am sincerely grateful to all of them for the roles they have played.

First and foremost, I would like to express my gratitude to Prof. Dott. Andrea Santangelo for his support throughout my journey. From the early days when I joined his group as a HiWi to the present, he has provided guidance, supervision, and a place within the high energy astrophysics group. I am grateful to Dr. Victor Doroshenko, my supervisor, whose intriguing idea for this project immediately caught my interest. His guidance and willingness to discuss and answer questions were invaluable. I am also grateful to him for reviewing my thesis and offering advice along the way. I would also like to thank Prof. Dr. Klaus Werner, who acted as an additional reviewer of my thesis. He was very kind and helpful in his comments and encouragement. I would especially like to thank Dr. Chris Tenzer for his warm welcome and extensive support. Conversations with him have always been enriching thanks to his vast knowledge and thought-provoking discussions. In addition, his approachability has always made me feel at ease when seeking his advice. I am truly grateful for his countless acts of support.

I would like to express my deep appreciation to my wonderful colleagues. A big thank you to Aafia and Camille for proofreading excerpts of my thesis and providing valuable input. I am also grateful to Heiko and Fabian for their help with the abstracts. Furthermore, I would like to thank them as well as Christian for the memorable "Vintage A112" moments. Our time together was filled with good discussions, shared experiences of university life, and most of all, a lot of fun. The success of my thesis is also due to the contributions of all the other members of IAAT. I would like to thank them for creating a friendly and supportive working environment that was both productive and enjoyable. Finally, I would like to thank my parents, my family, and Sam for their continuous support and belief in me. I am especially grateful to Sam for his patience, encouragement, and for always making me laugh. Thank you.